

Development of Phonon-Polariton THz Spectroscopy, and The Investigation of Relaxor Ferroelectrics

by

Benjamin John Paxton
B.A. Mathematics, B.A. Chemistry, University of Oregon, 2000

Submitted to the Department of Chemistry
in partial fulfillment of the requirements for the degree of

DOCTOR OF PHILOSOPHY

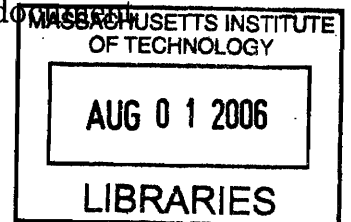
at the

MASSACHUSETTS INSTITUTE OF TECHNOLOGY

June 2006

© Massachusetts Institute of Technology, 2006. All rights reserved.

The author hereby grants to MIT permission to reproduce and distribute publicly paper and electronic copies of this thesis document in whole or in part.



Author /

Department of Chemistry
April 30, 2006

ARCHIVES

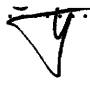
Certified by /

Keith A. Nelson
Professor
Thesis Supervisor

Accepted by /

Robert W. Field
Chairman, Department Committee on Graduate Students

This doctoral thesis has been examined by a committee of the Department of Chemistry as follows:

Professor Andrei Tokmakoff 

Chairman

Professor Keith A. Nelson

Thesis Supervisor

Professor Robert W. Field 

Development of Phonon-Polariton THz Spectroscopy, and The Investigation of Relaxor Ferroelectrics

by

Benjamin John Paxton

B.A. Mathematics, B.A. Chemistry, University of Oregon, 2000

Submitted to the Department of Chemistry
on May 24, 2006, in partial fulfillment of the
requirements for the degree of
DOCTOR OF PHILOSOPHY

Abstract

This thesis develops phonon-polariton based THz spectroscopy and uses this technique to make the first THz frequency dielectric measurements of a relaxor ferroelectric crystal, in particular $\text{KTa}_{0.982}\text{Nb}_{0.018}\text{O}_3$ (KTN 1.8). THz spectroscopy has emerged as an important probe for a wide variety of systems with the development of pulsed THz radiation sources and time-domain detection methods. Four factors motivate the use of phonon-polaritons generated in an ionic crystal (typically LiNbO_3 or LiTaO_3) via impulsive stimulated Raman scattering as a THz source for spectroscopy: (1) the versatility of phonon-polariton waveform shaping and detection, (2) the ability to use the ionic crystal as a compact, integrated spectroscopic platform, (3) the high THz refractive index of the host material facilitates coupling of THz radiation into high-dielectric samples, and (4) the potential to generate large amplitude polariton fields for nonlinear THz spectroscopy. Here we demonstrate both reflection and transmission implementations of THz spectrometers based on grating interferometric measurement of the phase and amplitude of a phonon-polariton waveform before and after interaction with a sample. A simple implementation of free space THz spectroscopy with conventional detection is also performed as a comparison to the polariton spectroscopy measurements. For the investigation of high-dielectric materials, both reflection and transmission polariton spectroscopy offer clear advantages over free space methods.

Polariton spectroscopy is used to measure the refractive index of KTN 1.8 in the ~ 50 -250 GHz range from 4-300 K as the index varies between ~ 10 and 35. At low temperatures, the Nb ions in our sample induce dynamically fluctuating polar nano-regions (PNRs) that dominate the dielectric response at low frequencies ($< 10^{-7}$ Hz). Our results differed from low frequency measurements in two ways: a significantly smaller, but still ionic, dielectric response and Curie-Weiss soft mode behavior. Together with ISRS transient grating measurements of the KTN soft mode in the low temperature disordered state, we attribute this behavior to soft mode

mediated fast Nb intersite hopping separated from slower PNR dynamics.

Thesis Supervisor: Keith A. Nelson

Title: Professor

Acknowledgments

MIT has been an extraordinary experience for me, and it has been my pleasure to learn, both scientifically and personally, from some exceptional individuals. First and foremost, I would like to thank my research advisor, Keith Nelson, for his enthusiasm and encouragement over the course of my thesis work. Several scientists contributed directly to the measurements presented in this thesis. Many of the polariton spectroscopy measurements presented in this thesis were performed jointly with Dr. Masashi Yamaguchi, his drive and ideas greatly advanced this project. The free space THz spectroscopy measurements were performed with Dr. Thomas Hornung and Ka-Lo Yeh. Finally, I would like to thank Prof. Jean Toulouse for providing the KTN sample and for taking an interest in our results, our discussions contributed greatly to my understanding of KTN.

On a personal level, I was fortunate to work and share a laser with Jaime Choi (nee Beers) and together we survived many a laser mishap, which she usually fixed with a steely optimism. Jaime also always knew exactly what to say to make me feel better when I was feeling down. Thomas Feurer was a friend and an exceptional scientist, it was great to have him guide me through my first few femtosecond laser experiments. I greatly enjoyed our Friday happy hours. Peter Poulin was the sage of the Nelson lab, both a fine experimentalist and softball player. His cleanliness shames us all. Some of my favorite memories are defending the chemistry department's honor with him in the annual NERC Softball tournament. I always enjoyed a discussion of how the world works with Nikolay Stoyanov, and I will never forget that "there is a limit". Josh Vaughan was my academic year. His curiosity always kept me on my toes, and I value his perspective on things. Thomas Hornung may seem quiet but he plays a mean game of tennis. Eric Statz was a bulwark of the group, exuding superhuman patience and avoiding email. I will remember Kenji Katayama for his style, and I am grateful for the hospitality he and his wife showed us when we visited Japan for an Ultrafast conference. Darius Torchinsky has the unique ability to combine pessimism with a positive spirit, and always make me smile. Christoph Klieber brought renewed

spirit and organizational motivation into the lab, I bequeath to him the RegA laser. May they treat each other well.

I overlapped with many other group members, and I am grateful to all of them for their help and support; Gloria Pless, Rebecca Slayton, Osamu Kamishima, Efren Gutierrez, Cindy Bolme, Kevin Webb, Kathy Stone, Ka-Lo Yeh, Tina Hecksher, Taeho Shin, Gagan Saini, Duffy Turner, Emmanuel Peronne, and Thomas Pezeril.

Boston also afforded many a great experience outside of MIT. Many of these were with my friends and longtime roommates Bryan and Matt. With the always punctual and motivated Verdi (no not the laser), I spent many mornings in the gym and many night on the town. Ashley was another great roommate and friend, her calming presence and thesis advice always proved invaluable. I was also fortunate to know Shelly and Cathy.

I would like also like to thank my undergraduate advisors, Professors Cathy Page and Geri Richmond, at the University of Oregon for the providing me some great educational opportunities in their labs and some general guidance. I felt well prepared coming to MIT.

Finally, I would like to thank my family for their love and support. Some of my earliest memories are my mother giving me vinegar and baking soda to make “volcanos” in my sand box. I also remember the chemistry set that my grandparents gave me as young teenager. I take it as an omen of my future as a physical chemist that I could not figure out how to open the chemicals until I was in college.

Contents

1	Introduction	23
2	Experimental	27
2.1	RegA Laser System	27
2.2	Janis STVP-100 Cryostat	28
2.3	Aerotech Air Bearing Stage	29
2.4	ISRS Transient Grating Experiment	31
2.5	Free Space THz Spectroscopy	38
2.6	“Deathstar” Optical Pulse Shaper	40
3	Phonon-polaritons as a THz Source	43
3.1	Introduction to Phonon-Polaritons	45
3.2	Impulsive Stimulated Raman Scattering	49
3.3	Generation and Detection of Phonon-Polaritons	51
3.3.1	Phonon-Polariton Generation	51
3.3.2	Phonon-Polariton Waveforms	53
3.3.3	Phonon-Polariton Detection	55
4	Development of Phonon-Polariton Based THz Spectroscopy	57
4.1	Motivation of Phonon-Polaritons as a THz Source	57
4.2	Phonon-Polariton Based THz Spectroscopy	60
4.2.1	Principles	60
4.2.2	Crystals	64

4.2.3	Phonon-Polariton Detection	66
4.3	Dielectric Function from THz Spectroscopy	70
4.3.1	Method of Data Extraction	71
4.3.2	Single Crystal Spectrometer	75
4.3.3	Reflection Spectrometer	76
4.3.4	Transmission Spectrometer with Cut Crystals	78
4.3.5	Spectroscopy with Free Space THz Radiation	80
4.4	Demonstration on LiTaO ₃ and LiNbO ₃	80
4.4.1	Temperature Dependence	81
4.4.2	Anisotropy	83
4.4.3	Horizontal Polarization of the Excitation and Probe	85
4.4.4	Polariton Coupling to Free Space	86
4.5	Free Space THz Spectroscopy	87
4.6	Comparison of Polariton based THz Spectroscopy to Free Space THz Spectroscopy	91
4.7	Multicycle Phonon-Polariton Waveform Generation	95
4.7.1	Deathstar Temporal Pulse Shaping	95
4.7.2	Transient Grating Phonon-Polariton Excitation	96
4.8	Conclusions and Future Directions	98
5	Introduction to Ferroelectrics	101
5.1	Ferroelectrics: Background and Terminology	101
5.2	Applications of Ferroelectrics	106
5.3	Basic Concepts	108
5.3.1	Classification of Ferroelectric Crystals	108
5.3.2	Curie-Weiss Law	109
5.4	Relaxor Ferroelectrics	110
6	Spectroscopic Studies of Nb Dynamics in KTN	115
6.1	Introduction to KTN	116
6.2	Phonon-Polariton Spectroscopy of KTN	121

6.3	Discussion of KTN Polariton Spectroscopy	125
6.4	ISRS Measurement of the KTN Soft Mode	128
6.5	Free Space THz Spectroscopy of KTN	131
6.6	Conclusions and Future Directions	134
7	Summary and Future Directions	137
A	Extraction Programs	141
A.1	Transmission Single Crystal	141
A.2	Reflection Spectroscopy	145
A.3	Transmission Spectroscopy Cut Crystal	149

List of Figures

2-1	Dimensions of the STVP-100 cryostat sample chamber.	29
2-2	Transient grating experimental apparatus. f_1 and f_2 are typically 15 cm. The spatial filtering of the higher diffraction orders and the attenuation of the reference field is not shown.	33
2-3	Phase mask patterns used in the transient grating and polariton spectroscopy measurements. Adapted from Crimmins [3].	36
2-4	Transient grating ISRS experiment in 5%MgO:LiNbO ₃ at 295 K excites a phonon-polariton response with a wavevector magnitude of 1090 cm ⁻¹ and a frequency of 2.11 THz. This is typical data for high temperature (>70K) in 5%MgO:LiNbO ₃	37
2-5	Transient grating ISRS experiment in 5%MgO:LiNbO ₃ at 8 K excites a phonon-polariton response with a wavevector magnitude of 1090 cm ⁻¹ and a frequency of 2.23 THz. Reversible photorefractive damage degrades the signal quality relative to figure 2-4 by scattering the optical pump light, but less damping in the LiNbO ₃ at low temperature generates a longer polariton pulse train.	38
2-6	Free space THz spectrometer experimental apparatus. Phonon-polaritons are generated in LiNbO ₃ and coupled to free space. The THz radiation induces birefringence in an optical probe in the ZnTe crystal. Figure prepared by Ka-Lo Yeh.	39
2-7	The Deathstar optical pulse shaper. Figure prepared by Jaime Choi. .	40

3-1	Simulated phonon-polariton dispersion curve for LiTaO ₃ . The solid lines indicate the upper and lower polariton branches. The dashed lines describe the dispersion of uncoupled optical radiation. The band gap describes the region where phonon-polariton propagation is forbidden. The lower branch at low wavevector is the region of interest for our experiments.	49
3-2	Phonon-polariton generation and detection with a short femtosecond excitation pulse.	53
3-3	Schematic illustration of a propagating polariton waveform generated with a femtosecond excitation pulse. The right propagating polariton waveform is emphasized to show that although the primary direction of propagation is lateral, the polariton waveform undergo total internal reflection as it propagates between the front and back surfaces.	53
3-4	The excitation pulse is focused to a line. This launches a phonon-polariton plane wave generated throughout the volume of the crystal. The right propagating polariton waveform is not shown.	54
4-1	Top view - Schematic illustration of polariton-based transmission THz spectroscopy cell. The pump beam is focused to a line, and the polaritons are generated throughout the depth of the cell. The LiTaO ₃ crystals are cut to compensate for the forward polariton wavevector component. The pump excitation also generates a right propagating polariton waveform that is not involved in the experiment and is not shown.	61

- 4-2 Side view THz transmission cell. The LiTaO_3 crystals are not cut to compensate for the forward propagation angle of the polariton waveform, and as such, polariton reflections are observed. The raw data shows the propagation of the left propagating polariton waveform. The labels R and L on the peaks in the raw data refer to interferometric measurements at the right and left probe arms and the arrows show the direction of polariton propagation. In chronological order, the first peak is the polariton waveform arriving at the right probe arm, the second peak is the reflection from the pump side of the sample measured at the right probe arm, the third peak is propagation through the sample arriving at the left probe arm, the fourth peak is reflection from the far side of the sample at the right probe arm, and the fifth peak is the polariton after two reflections arriving at the probe arm. Peak identification can be aided by translating the cell with respect pump and probe beams to see how the peak positions change. 62
- 4-3 In LiTaO_3 , a line excitation is focused along the horizontal dimension with a cylindrical lens with a focal length of 30cm (red) and 20cm (blue). The polariton pulse shape is related to the spatial derivative of excitation profile. A tighter focus results in a shorter pulse in the time domain and a correspondingly larger bandwidth. 64
- 4-4 Comparison of detected polariton intensity in LiTaO_3 and 3% $\text{MgO}:\text{LiNbO}_3$. Both the generation and detection efficiencies are stronger in LiNbO_3 . 65
- 4-5 Comparison of uncut LiTaO_3 was to a cut LiTaO_3 crystal that has been physically pressed together. A 5% transmission loss was calculated from comparing the excitation peak to the transmitted peak. 66
- 4-6 The dual arm interferometer measures the THz pulse before and after interaction with the sample. 67

4-7	Top view of single crystal spectroscopy cell illustrating the portions of the generated polariton wavefront that probe 1 and probe 2 coherently integrate. Scale E1 and Scale E2 are used to normalize the measured polariton pulses. “pupr” is the distance between the pump and probe beams. “prpr” is the distance between the probe beams. “txtal” is the thickness of the crystal.	76
4-8	Top view of reflection spectroscopy cell illustrating the portions of the right and left generated polariton wavefronts that probe 1 coherently integrates. Scale E1 and Scale E2 are used to normalize measured polariton wavepackets.	77
4-9	LiTaO ₃ is cut at an angle of 20° and a clamp is used to hold the crystals together. Scale E1 and Scale E2 are used to normalize the measured polariton wavepacket signals.	79
4-10	Polariton spectroscopy of LiTaO ₃ as a function of temperature. See figure 4-2 for spectrometer geometry. The transmitted peaks (right) show a strong temperature dependent absorption. And while not as apparent in the raw data, the variation in time delay of the transmitted peak is also significant.	82
4-11	Temperature dependent refractive index for LiTaO ₃ performed in two separate experimental trials. The value of the refractive index is independent of frequency in the measured range of 50-250 GHz.	83
4-12	THz spectroscopy of different orientations of the optic axis of LiTaO ₃ . Plot (a) shows the polariton polarization parallel to the optic axis of the LiTaO ₃ sample. Plot (b) shows the polariton polarization perpendicular to the optic axis of the LiTaO ₃ sample. A slight increase in the time of flight is observed.	84
4-13	Measurement of a polariton pulse in LiTaO ₃ with excitation and probe polarized parallel to the optic axis, (HH) in the lab frame. This generation and detection is much weaker than our normal (VV) excitation.	85

4-14 Demonstration of polariton coupling to free space. The cut crystal couples $\sim 53\%$ of its energy to free space THz radiation. The polariton waveform in the uncut crystal undergoes total internal reflection. The reflection is not seen in the cut crystal because the probe does not intersect the polariton waveform at the proper angle to see a constant phase slice.	86
4-15 Top view: A polariton waveform generated in LiTaO_3 is used as a THz radiation emitter and recoupled into a second LiTaO_3 crystal where it is measured. The spacing, A , is 1 mm in the lower scan and 2 mm in the upper scan.	87
4-16 The refractive index of $5\%\text{MgO}:\text{LiNbO}_3$ measured with free space THz spectroscopy.	88
4-17 The extinction coefficient, κ , of $5\%\text{MgO}:\text{LiNbO}_3$ measured with free space THz spectroscopy.	89
4-18 THz water resonances in measured with free space THz spectroscopy. The reference was taken in the cryostat with atmospheric water vapor present, while the low temperature measurement on $5\%\text{MgO}:\text{LiNbO}_3$ was dry. Assignments from Grischkowsky [83].	90
4-19 Comparison of PP polariton spectroscopy with free space methods in KTN. Polariton transmission spectroscopy is able to transmit more THz radiation through the KTN sample at lower temperatures where the dielectric constant begins to diverge. Free space measurement could not be continued below 150 K while polariton transmission measurements were performed at all temperatures down to 80 K. Polariton reflection measurements were performed down to 4 K. The results of measurements at lower temperatures are reported subsequently. . . .	92

4-20	The reflection amplitude coefficients determined from our experimentally measured values of the refractive index for KTN utilizing polariton spectroscopy. The values were converted to equivalent values of what a free space reflection THz spectroscopy method would yield for air KTN interface at 45° and normal incidence.	93
4-21	An optical temporal only pulse shaper was used to generate a 7 cycle pulse train to excite a 400 GHz polariton excitation that was detected with the standard dual arm interferometer. The rapid decay of the waveform from one probe arm to the second is an artifact of the excitation and detection used.	95
4-22	A grating is imaged into a LiNbO ₃ crystal exciting a narrow band polariton waveform with a 1 THz frequency. The black plot shows the probe overlapped with the excitation pulse and the polariton propagating away from the probing region. The red plot shows polariton propagating into and out of the second probe region. The modulation amplitude of the black plot is much larger because it is measuring both the right and left propagating polariton field and measuring the polariton throughout the entire depth of the crystal.	97
5-1	Structure of an ABO ₃ perovskite in the cubic paraelectric phase. The A cations site is on the corners of the cube, the B cation is situated at the center, and Oxygen on the face centers.	103
5-2	Schematic representation of a pair of unit cells undergoing several fundamental types of structural phase transitions from a centrosymmetric prototype. Adapted from Lines and Glass [88].	106
5-3	Schematic illustration of B cation occupation sites within the framework of the eight site model for an ABO ₃ perovskite. Adapted from Dougherty [17].	109
5-4	Overview of differences between normal ferroelectrics and relaxors. Adapted from Samara [7].	113

6-1	Schematic drawing of PNR formation. At high temperature the correlation length r_c is on the order of one lattice constant. At lower temperatures the dipole induces a polarization in several unit cells around it forming a PNR. Adapted from Samara [7].	118
6-2	The temperature dependence of KTN's index of refraction at ~ 50 to 250 GHz measured with free space THz spectroscopy, two trials of phonon-polariton reflection spectroscopy, and phonon-polariton transmission spectroscopy with cut crystals.	122
6-3	Unprocessed data from polariton transmission measurements of KTN 1.8. At 150 K the time of flight of the transmitted peak E2 significantly increased due to the refractive index change of KTN.	122
6-4	Power spectra of a polariton waveform generated with cylindrical lens ($f = 20$ cm) before and after reflection from KTN 1.8 at 300 K. . . .	123
6-5	Unprocessed data from polariton reflection spectroscopy measurements of KTN 1.8. A schematic of the relative positions of the pump and probe beams is shown at the bottom of the figure. The blue region designates the the reflected polariton signal. The pink region designates the left propagating polariton passing through the left probe arm and can be used to determine the temperature dependent dielectric properties of the LiTaO_3 crystal.	124
6-6	Refractive index measured with polariton transmission and reflection spectroscopies (~ 50 -250 GHz) on KTN 1.8, presented alongside dielectric spectroscopy at lower frequencies by Samara on KTN 2.0 [110]. . .	125
6-7	Curie-Weiss plot of $1/\epsilon'$ for all polariton spectroscopy data. A linear regression was fit to the high temperature data (150-300 K) and appears to describe all of the dielectric data above T_f at ~ 30 K. . . .	126
6-8	Wavevector dependence of the KTN 1.8 soft mode at 10 K, where the magnitude of the wavevector ranged from 840 to 3500 cm^{-1}	128

6-9	Transient grating ISRS measurement of the KTN 1.8 soft mode as a function temperature. The magnitude of the excitation wavevector is 3500 cm^{-1} .	129
6-10	Temperature dependence of soft mode in KTN 1.8 measured interferometrically. As the temperature goes from 10 to 40 K the soft mode oscillation (blue arrows) change from underdamped to overdamped, until it disappears completely by 40 K.	131
6-11	Unprocessed times series of THz transmission spectroscopy of KTN 1.8 at 300 K and a reference. The blue boxes represent the windowed portion of the time series used for data extraction. The y-axes are to the same scale.	132
6-12	Bandwidth of the reference THz field and a THz field transmitted through KTN 1.8 at 300 K.	132
6-13	THz free space measurement of the index of refraction of KTN 1.8. Below 150 K no transmitted signal could be detected.	133
6-14	THz free space measurement of the extinction coefficient κ of KTN 1.8. Below 150 K, no transmitted signal could be detected.	134

List of Tables

2.1	Typical Parameters of the Coherent RegA laser system	27
3.1	A_1 symmetry transverse optical phonon modes in LiNbO_3 and LiTaO_3 obtained from ref. [44, 45]. S is the coupling strength between the lattice vibration and the electromagnetic radiation.	48
3.2	Constants for modulation of the index of refraction due to phonon-polaritons from reference [22]. Units for r_{13} and r_{33} are pm/V.	55
5.1	Values of the ferroelectric transition temperature T_c [88] for four chemical analog ABO_3 ferroelectrics that are of particular interest in this thesis. KTaO_3 and KNbO_3 are simple cubic perovskites in the paraelectric state while LiTaO_3 and LiNbO_3 have a more complicated structures. Note that changes in chemical compositions can cause substantial changes in ferroelectric behavior. KTaO_3 is an incipient ferroelectric which low temperature ferroelectric transition is frustrated by quantum fluctuations.	104

Chapter 1

Introduction

The development of pulsed free space THz radiation sources and time-domain detection methods have driven an active and growing interest in THz spectroscopy and imaging [1]. These techniques use THz fields that go through free space before and after interaction with a sample and cover the $\sim 0.1 - 10$ THz frequency range. THz spectroscopy has been applied to a wide array of systems as a probe of intramolecular modes of vibration, torsions and rotations in molecules, and phonons in solids. This thesis demonstrates an alternate approach to that of conventional free space THz methods, enabling compact spectrometer systems and the study of high-dielectric materials. Our approach uses phonon-polariton waveforms in ionic crystals as a source of THz frequency electric fields.

Phonon-polaritons are lattice vibrational waves that couple to electromagnetic radiation. Through this coupling, coherent collections of polaritons form propagating waveforms that travel at light like speeds. In LiTaO_3 and LiNbO_3 crystals, these polaritons have THz frequencies and we use them as a source of THz radiation for dielectric spectroscopy. Because the polariton waveforms are coupled to a crystal, we can observe their propagation in ways not possible with free space radiation. Much effort in the Nelson Lab [2–6] has been directed towards generating, manipulating, controlling and detecting these lattice vibrational waves. This thesis extends this work by performing the first quantitative spectroscopic measurements with phonon-polariton waves and developing phonon-polariton spectroscopy into practical tool

for performing dielectric spectroscopy at THz frequencies. Several implementations of compact polariton spectrometers are presented and spectroscopic measurements are made from both reflected and transmitted polariton waveforms. This thesis also connects to free space THz spectroscopy methods by including some simple free space THz measurements for comparison to the polariton spectroscopy results.

The unique advantages of polariton spectroscopy are leveraged to investigate the relaxor ferroelectric $\text{KTa}_{0.982}\text{Nb}_{0.018}\text{O}_3$ (KTN 1.8) which, unlike normal ferroelectric crystals does not form a true ferroelectric phase with long-range ordering of dipole moments in each unit cell. At low temperature, it is well known [7] that KTN forms polar nanoregions (PNRs) around the Nb ion impurities. These fluctuating dipoles provide an enormous dipole response to low frequency ($< 10^{-7}$ Hz) electric fields, resulting in a huge dielectric constant ($\epsilon' > 100,000$). The experiments presented here constitute the first “THz” frequency (50-250 GHz) dielectric measurements on a relaxor ferroelectric. The measurements perform a direct test of the suggestion by Toulouse [8] that the complex dynamics of some relaxor ferroelectrics could be separable into fast, phonon assisted hopping of central ions (Nb in this case) and slower PNR relaxation. Impulsive stimulated Raman scattering measurements of the KTN soft optic phonon mode were also conducted to examine the coupling of this mode to the fast central ion hopping dynamics.

Chapter 2 introduces several topics: the femtosecond laser system used for the majority of experiments presented in this thesis, the sample-in-vapor cryostat used for the low temperature spectroscopic studies on the relaxor ferroelectric KTN, a description of the free space THz spectroscopy experiment that is used for comparison to the polariton spectroscopy data, the transient grating measurements that are used to investigate the soft mode of KTN, and the “Deathstar” optical pulse shaper that used to excite multicycle THz waveforms.

Next, chapter 3 provides a brief overview of THz spectroscopy and an introduction to phonon-polaritons. It discusses the generation of phonon-polaritons through impulsive stimulated Raman scattering and phonon-polariton propagation and detection. This introduction provides the necessary background to understand phonon-polariton

based THz spectroscopy. Chapter 4 explains the basic principles of polariton spectroscopy, introduces three configurations of compact THz spectrometers, and explains the methods necessary to extract spectroscopic data from polariton waveform measurements.

The other main topic of this thesis is the investigation of the model relaxor ferroelectric, dilute $\text{KTa}_{1-x}\text{Nb}_x\text{O}_3$ (KTN). Chapter 5 provides a general introduction to ferroelectrics and highlights the features most relevant to relaxor ferroelectrics. Finally, chapter 6 presents the first quantitative measurements made using the polariton spectroscopy developed in this thesis and the first THz measurement of a high-dielectric material, KTN. The KTN refractive index is determined in the ~ 50 - 250 GHz range from 4-300 K are made. These results are supplemented with ISRS transient grating measurements of the KTN soft mode to provide new insights into the dynamics of Nb ion impurities and relaxor ferroelectrics generally. Chapter 7 provides a summary of the work presented in this thesis and discusses future directions of research.

Chapter 2

Experimental

2.1 RegA Laser System

The experiments performed in this thesis, with the exception of the free space THz measurements discussed in section 2.5, were performed with a Coherent RegA laser system. The system consists of an 18W Coherent Verdi diode laser that pumps both a Coherent Mira-900 femtosecond oscillator and Coherent RegA-9000 amplifier. Typical parameters for the laser system are given in table 2.1.

	ML Power	CW Power	Rep Rate	Bandwidth	Duration
Verdi	–	16.5 W	–	–	–
Mira	500 mW	900 mW	76MHz	12 nm	140 fs
RegA	1W	1.8W	250KHz	9 nm	250 fs

Table 2.1: Typical Parameters of the Coherent RegA laser system

The Verdi pump laser replaced an unstable and unreliable Coherent Innova 400 20W Argon ion pump laser that had power and pointing stability problems. Most of the polariton spectroscopy measurements presented in this thesis were made when the system was pumped with the argon ion pump laser, and the total power of the amplified system was typically only 700-800mW and noticeably less stable than with the solid state pump. All of the transient grating measurements were performed with the Verdi pumped system. There has been one other significant alteration to the laser

system. The grating in the RegA pulse compressor was damaged and was replaced with a Spectrogon US Inc. blazed diffraction grating, part PC 2200 30 x 30 x 10 mm, optimized for 800 nm with >90% efficiency.

2.2 Janis STVP-100 Cryostat

The Janis cryostat STVP-100 (Serial No. 8570) was critical to the temperature dependent experiments in this thesis. The cryostat works equally well with either liquid nitrogen or liquid helium cryogenics, although most of the experiments presented here used liquid helium. The cryostat is a “sample in vapor” model, which was useful in guaranteeing that all of the crystals in the polariton spectroscopy measurements were at the desired temperature. Because the sample is not in vacuum, as it would be in a cold finger cryostat, there is an additional convenience in that the sample can be easily manipulated at all times, i.e. replaced while the cryostat is chilled, due to the positive pressure in the sample chamber. In this cryostat the sample has a vertical translation range of 2 inches and can be rotated a full 360°. This type of cryostat has a vacuum jacket to insulate the cryogenic chamber. Our cryostat was custom-designed to enlarge the cryogenic chamber, depicted in figure 2-1, beyond that of the standard STVP-100 models. This was done to allow a greater angle (23°) for crossed laser pulses as well as to accommodate larger samples. The distances between the windows, and the window thicknesses, are shown in figure 2-1. These distances are useful for estimating the time delay between THz echo pulses that sometimes arrive after reflection at the cryostat windows.

The inner windows, between the vacuum jacket and the cryogenic material, have special indium seals so that stress induced by the temperature change is minimized. This is important for depolarization experiments where strain in the quartz windows can induce birefringence. Consequently, however, these windows do not seal well and can leak slightly upon going from low to high temperature so that the vacuum jacket must be reevacuated. Although it is not necessary, in practice it is often convenient to evacuate continuously the vacuum jacket with a diffusion pump. Never do this

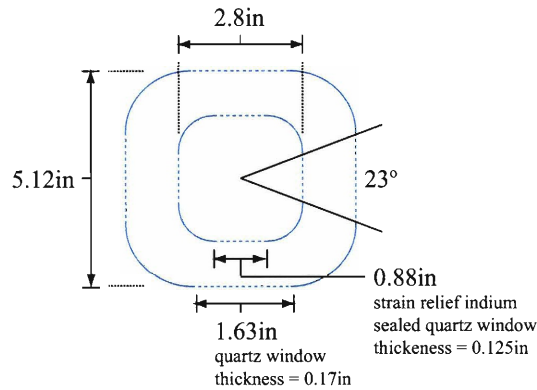


Figure 2-1: Dimensions of the STVP-100 cryostat sample chamber.

with mechanical rotatory pump however, cryo-pumping in the sample chamber will pull oil of the rotatory pump and into the vacuum system.

The temperature of the cryostat is controlled through a Lakeshore model 332 temperature controller which controls a 50 Ohm vaporizing heater at the bottom of the cryostat where the cryogen enters the chamber. There are two diodes, one by the heater and one at the end of the rod that mounts the sample. It is important to use the diode by the vaporizer for temperature control and the diode by the sample as the estimation of the sample temperature. The electronic temperature control is only a fine adjustment; the most important control of the temperature occurs on the manual flow control valve of the cryogen transfer line. This valve ranges from completely open to completely closed in about 5 full turns. The cryostat operates optimally with this valve less than half a turn away from fully closed.

2.3 Aerotech Air Bearing Stage

As part of my thesis work, I interfaced the Aerotech air-bearing stage, model ABL 2000, used as delay line in the Deathstar acoustic measurements [9,10] to a computer. The Aerotech stage is controlled by an Aerotech Soloist controller, and power is supplied through a Aerotech step-down transformer module. The stage offers 1.2 m of travel, 1 μm resolution, and velocities of 400 mm/s. The stage is a continuous ve-

locity type, which means that it moves from one position to another with continuous velocity motion (or a trapezoidal velocity profile). The acceleration to and from this velocity is quick and can be ignored for data collection purposes. This type of motion is unusual for femtosecond time domain spectroscopy, where the position of the stage must be synchronized with the data collection, and stepper motor translation stages are more often used. However the air-bearing stage is well suited for motion over relatively large distances. The Aerotech stage is used with a Stanford Research Systems lockin amplifier (LIA), model SRS810, for data acquisition. A LIA necessarily averages a signal over a time interval, and as such the signal the LIA measures is an average over the delay position of the continuous velocity Aerotech stage. The labview software that controls the stage allows the user to set the time constant of the LIA and resolution of the stage. Then the velocity of the stage is determined such that the stage moves the distance of one resolution increment in “ i ” time constants, where $i = 1$ was found to be the best tradeoff between resolution and data collection rate. A minimum velocity of $100 \mu\text{m/s}$ and minimum travel distance of $100 \mu\text{m}$ are enforced as the stage does not perform consistently below these values.

Our Soloist controller was purchased with the “plus” option package that included the PSO (position synchronized output) feature. This feature is linked to the stage position encoder and sends a programmable TTL signal when the encoder travels a programmable number of $1 \mu\text{m}$ steps. The TTL signal is sent to a National Instruments data acquisition (DAQ) card. This card synchronizes the acquisition of the analogue output signal of the digital LIA and stage position. Although the LIA can be triggered directly and has an internal buffer to store triggered data, it can only store triggered data at an acquisition rate of less than 1024 Hz . This is too slow to store the digital LIA data directly, and for this reason the analog output of the LIA, which provides the LIA signal at rate of 102 KHz , is used.

2.4 ISRS Transient Grating Experiment

Laser induced dynamic grating or four-wave mixing spectroscopy is a powerful time-resolved optical technique that is widely used to study a broad range of phenomena, including molecular and lattice vibration, bulk and surface acoustic waves, and relaxation and transport processes [11, 12]. In this technique, two interfering laser beams are crossed in a sample to produce a spatially periodic material excitation that is monitored through the diffraction of a third (probe) beam. All transient grating measurements were conducted using diffractive optics [4, 13, 14] as described below.

The use of diffractive optics simplifies the use of a fourth beam as a local oscillator (or reference beam) to optical heterodyne the probe beam for improved detection, yielding a signal intensity I_S on the diode of:

$$I_S = I_R + I_D + 2\sqrt{I_R I_D} \cos \theta \quad (2.1)$$

where I_R and I_D are the reference and diffracted signal intensities, respectively, and θ is the phase difference between these optical fields. If the excitation field is modulated with a chopping wheel, then the first two terms in equation 2.1 are constant, and their contribution to the signal can be filtered with lockin amplifier detection. By its nature the diffracted signal is weak, so it is easy to experimentally set conditions such that $I_R \gg I_D$, so that $I_S \propto \sqrt{I_D}$.

Crossed femtosecond pulses were used to excite Raman active modes in LiTaO_3 , LiNbO_3 and the relaxor ferroelectric $\text{KTa}_{1-x}\text{Nb}_x\text{O}_3$ (KTN) via impulsive stimulated Raman scattering (ISRS). The theory of ISRS will be introduced in section 3.2. This section introduces the experimental apparatus for the generation and detection of laser induced transient gratings. The experiments presented here follow a major advance in this technique by Rogers et. al. [13], in which the ± 1 diffraction orders from transmissive diffraction gratings were used as the two beams for crossed excitation pulses and ± 1 diffraction orders of second laser beam were used for the probe and local oscillator beams. This approach has three significant advantages. First, the two pairs of crossing beams traverse common path optics, and are interferometrically

stable. Secondly, when a beamsplitter is used to make two fs pulses for crossed excitation the area of overlap is smaller than the spatial size of pulse due to the short pulse duration, in what is known as the “pancake effect”. This limits the number of interference fringes, N , to roughly, $N \sim 2\tau c/\lambda$, where τ is the pulse duration, λ is the central wavelength. In contrast, the diffraction gratings tilt the wavefront of the interfering pulses such that they interfere over roughly their entire spatial region [15]. The third benefit, for the case where the pump and probe interact with gratings of the same period, the condition for Bragg reflection is automatically satisfied, and the diffracted beam is automatically collinear with the reference beam.

The transient grating experimental methods used in this thesis are outlined below. For a more comprehensive discussion of the experimental details and theory of transient grating ISRS measurements consult [4, 14, 16–18]. The basic transient grating experiment apparatus is presented in figure 2-2. The pump and probe beams are diffracted off of separate gratings (of the same grating period) and a cylindrical (typically 15 cm) lens (CL1) collimates the diffracted orders. The distance f_1 between CL1 and the phase mask is the most critical parameter of the alignment. This distance is optimized by placing a retroreflector at the focal plane of CL1, and the distance between the phase mask and CL1 is adjusted by translating the phase mask until the light reflected from the retroreflector is recombined by the phase mask. In the transient grating experiment all diffraction orders (including the zeroth) except for the ± 1 orders are spatially blocked near the Fourier plane of CL1 between f_1 and f_2 . The ± 1 diffraction orders (four beams) for both the pump and probe beam are crossed in the sample by a spherical lens of focal length f_2 , typically 15cm. The relative sizes of the excitation and probe (and local oscillator) regions are set by controlling the spatial sizes of the pump and probe beams on the corresponding diffraction gratings. The heterodyne configuration is illustrated, but the homodyne signal can be easily obtained by blocking the local oscillator field, and this is often done during alignment.

The relative phase of the laser induced grating signal and the reference field can be set by relative translation of the pump and probe diffraction gratings. The local oscillator can be attenuated by a special ND filter that has some exposed substrate

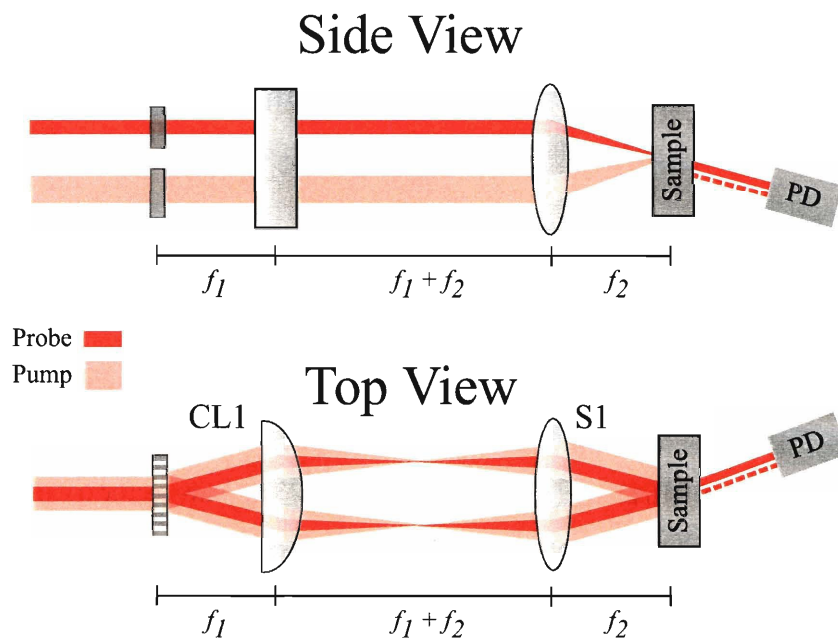


Figure 2-2: Transient grating experimental apparatus. f_1 and f_2 are typically 15 cm. The spatial filtering of the higher diffraction orders and the attenuation of the reference field is not shown.

glass. The local oscillator passes through ND filter and the probe beam passes through the glass substrate. This is necessary to keep the probe and local oscillator temporally overlapped. In general, the strongest local oscillator that does not induce a non-linear interaction in the sample or saturation of the detector should be used. The power of the probe beam is set before the phase mask splits it into a probe and local oscillator through diffraction. For probe beam and local oscillator power level of ~ 35 mW or less, attenuation of the local oscillator was not needed.

The size of the pump and probe beams before the phase masks are set to ensure that the pump grating is larger in height than the probe. This ensures that the transient grating has a defined wavevector given by:

$$\mathbf{q} = \pm(\mathbf{k}_1 - \mathbf{k}_2) \quad (2.2)$$

where \mathbf{q} is the wavevector of the material response and \mathbf{k}_1 and \mathbf{k}_2 are the wavevector of the two excitation pulses. For dispersive vibrational excitations, such as phonon-polariton modes, the vibrational wavevector depends on orientation of the sample [12], and \mathbf{q} is only approximately given by $\pm(\mathbf{k}_1 - \mathbf{k}_2)$. The wavevector \mathbf{q} can be calculated from the optical parameters of the experiment. The wavelength of the grating formed by imaging the binary phase mask into the transparent sample is given by,

$$\Lambda = \frac{\Lambda_0 f_2}{2f_1} \quad (2.3)$$

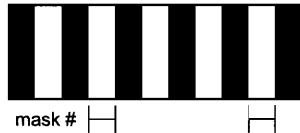
where f_1 is the focal length of the collimating CL1 lens and f_2 is the focal length of S1 which focuses the beams into the sample, λ is the center wavelength of the pump light, and Λ_0 is the phase mask period (twice the phase mask number), and the wavevector $\mathbf{q} = 2\pi/\Lambda$. As will be elaborated further in chapter 3, phonon-polaritons that are excited with a grating patten of wavevector \mathbf{q} have a small forward wavevector component, so \mathbf{q} defines the lateral component q_x of the phonon polariton wavevector, separate from the small forward component. The phonon polariton wavelength is given by,

$$\Lambda = \frac{\Lambda_0 f_2}{2f_1} \cos(\theta_f). \quad (2.4)$$

Where θ_f is the angle of forward propagation of the polariton.

The binary phase masks used in these experiments are custom made by Digital Optics Corporation, Charlotte NC. The diffraction efficiency is optimized for a particular wavelength by controlling the etch depth of the phase mask pattern. These experiments use gratings optimized for 800 nm light. The masks are also numbered such that the mask number equals half of the grating period. Figure 2-3 shows the available mask patterns.

Digital Optics Corporation



Etch Depth = $\lambda/(2n-2)$

diffraction angle, $\theta = \lambda/(2 \text{ mask\#})$

~70% Energy into +/- 1 orders

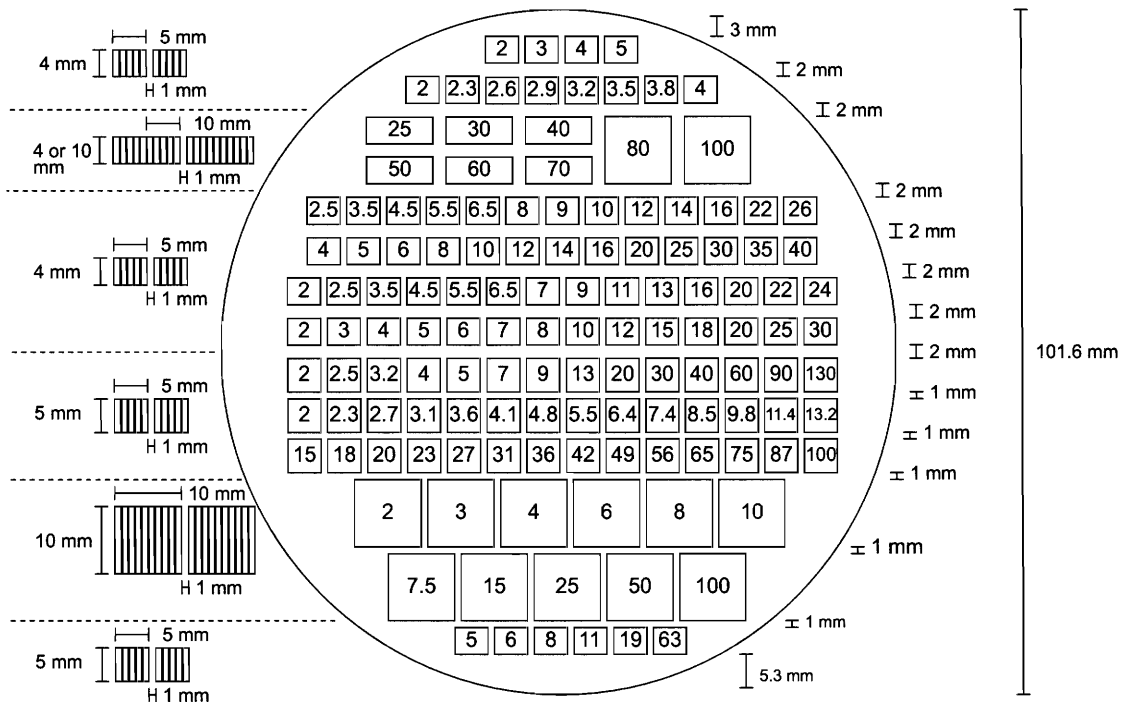


Figure 2-3: Phase mask patterns used in the transient grating and polariton spectroscopy measurements. Adapted from Crimmins [3].

Typical data for the transient grating ISRS experiments are presented in figure 2-4. The experiment shown is for 5%MgO:LiNbO₃ at room temperature (295 K), but in a cryostat. The grating excites a phonon-polariton response that has a well defined wavevector magnitude of 1090 cm⁻¹. The data were collected using a lockin amplifier with a time constant of 30 ms, and the total data acquisition time was ~3 minutes.

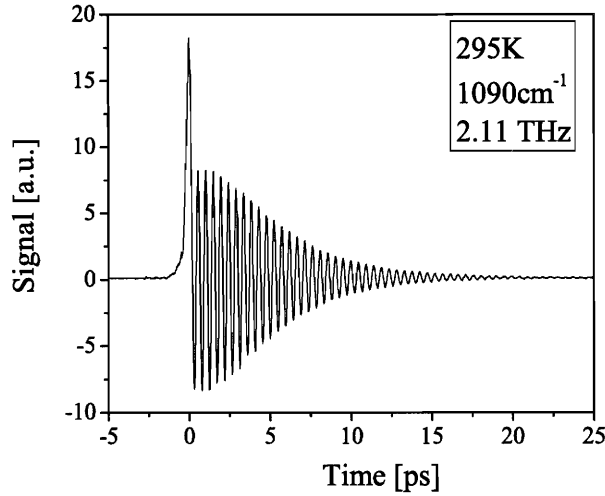


Figure 2-4: Transient grating ISRS experiment in 5%MgO:LiNbO₃ at 295 K excites a phonon-polariton response with a wavevector magnitude of 1090 cm⁻¹ and a frequency of 2.11 THz. This is typical data for high temperature (>70K) in 5%MgO:LiNbO₃.

At low temperatures, optical experiments on LiNbO₃ and LiTaO₃ are more difficult because reversible photorefractive damage occurs, which strongly scatters light [19]. This has important implications for our polariton spectroscopy measurements, and is discussed more fully in section 4.2.2. MgO doped LiNbO₃ is substantially more resistant to photorefractive damage than LiNbO₃ or LiTaO₃, and an experiment identical to figure 2-4 is presented in figure 2-5 at a temperature of 8K. As expected, the damping of the polariton mode is significantly reduced, and the frequency of the polariton mode changes slightly. The signal to noise ratio of the data is diminished relative to that of the high temperature measurement; this is due to the photorefractive ef-

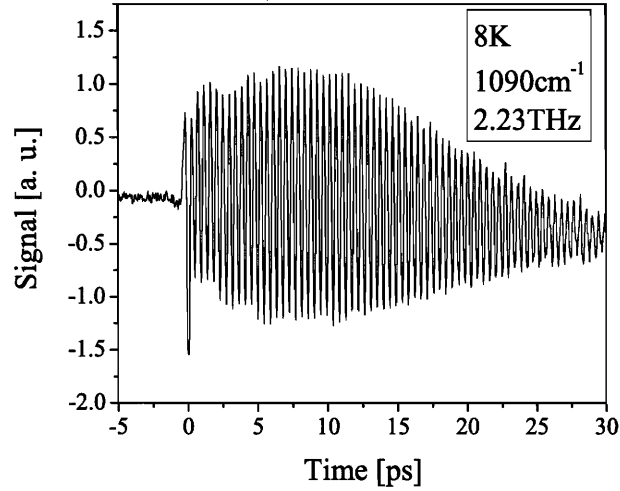


Figure 2-5: Transient grating ISRS experiment in 5%MgO:LiNbO₃ at 8 K excites a phonon-polariton response with a wavevector magnitude of 1090 cm⁻¹ and a frequency of 2.23 THz. Reversible photorefractive damage degrades the signal quality relative to figure 2-4 by scattering the optical pump light, but less damping in the LiNbO₃ at low temperature generates a longer polariton pulse train.

fects and becomes progressively worse with exposure to the optical excitation pulses. For example it was only possible to take this scan over several minutes before pump scatter overwhelmed the reference field. Sum frequency chopping of both the pump and probe was also used to minimize the effects of the scattered pump light. This data scan would not have been possible in undoped LiNbO₃ or LiTaO₃ due to the photorefractive effects.

2.5 Free Space THz Spectroscopy

A simple implementation of conventional THz spectroscopy was performed to provide a comparison to the phonon-polariton spectroscopy measurements pioneered in chapter 4. In this context, we use “conventional” THz spectroscopy to mean the use of any of a variety of THz sources, including photoconductive antennas or electro-optic crystals such as zinc telluride or LiNbO₃, where THz radiation propagates through

free space, and gold parabolic mirrors are used to collimate and focus the THz radiation into a sample and then into a detector (usually a electrooptic detection crystal or a photoconductive antenna). These techniques are well established [1] and such THz spectroscopy set-ups are published [20].

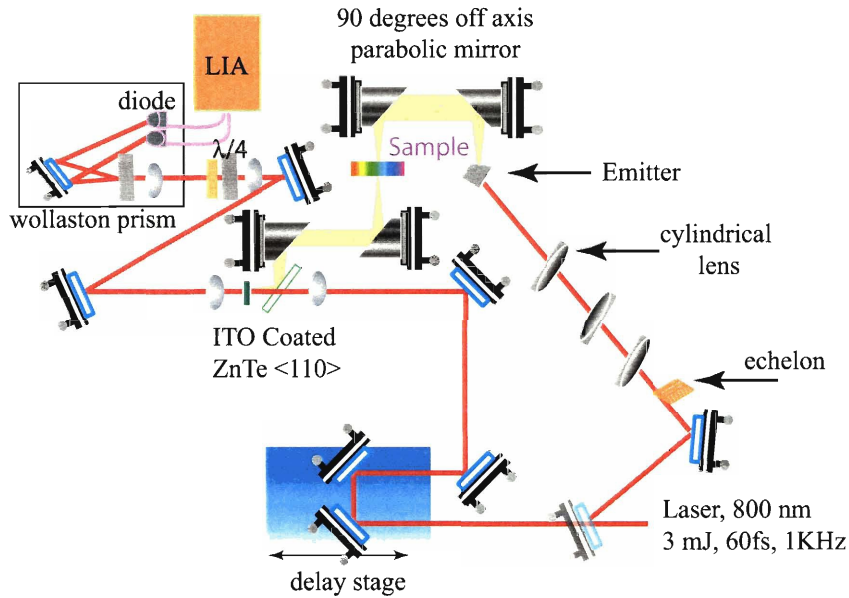


Figure 2-6: Free space THz spectrometer experimental apparatus. Phonon-polaritons are generated in LiNbO_3 and coupled to free space. The THz radiation induces birefringence in an optical probe in the ZnTe crystal. Figure prepared by Ka-Lo Yeh.

Our implementation of free space THz spectroscopy is only a small part of the work presented in this thesis, and while it is sensitive (signal-to-noise $\sim 10^{-4}$), it is not state of the art. Our free space THz spectroscopy experimental set-up is presented in figure 2-6. An amplified femtosecond laser system (Odin Quantronix) that produced 3 mJ, 60 fs pulses centered at 800 nm with 1 kHz repetition rate were used to generate phonon-polaritons in a LiNbO_3 crystal. The crystal was cut to more effectively couple THz radiation to free space. The THz radiation is collimated and focused through the sample by pair of parabolic gold mirrors ($f= 19.5$ cm). A second set of parabolic gold mirrors ($f= 19.5$ cm) is used to focus the THz radiation into a $500 \mu\text{m}$ ZnTe detection crystal ([110] cut, INGCORYS Laser Systems Ltd, UK). The ZnTe crystal

was coated with indium-tin oxide (ITO) which serves as an anti-reflection coating. The THz radiation modulates the optical index of refraction of ZnTe via the Pockel's effect [21, 22], and this modulation is measured with a circularly polarized probe beam. A Wollaston prism is used to split the probe beam to two photodiodes, and the difference signal is measured with a lockin amplifier.

A mask of ~ 1 by 2 mm is used at the focus of parabolic gold mirror that focuses the THz into the sample to ensure that the spot size of the THz radiation field is smaller than the sample and that all of the THz radiation goes through the sample. This mask does not significantly reduce the transmitted THz.

2.6 “Deathstar” Optical Pulse Shaper

The “Deathstar” is an ultrafast optical pulse shaper which generates tunable optical pulse trains with frequencies between 1-1000 GHz [9, 10]. At 1 GHz, this corresponds to 1 ns delay between pulses, which is well beyond the temporal window of conventional femtosecond pulse shapers. The Deathstar pulse shaper was designed to access these lower frequencies for acoustic measurements, and in this thesis we use it to generate multicycle polariton waveforms that are discussed in section 4.7. Figure 2-7 shows the Deathstar apparatus.

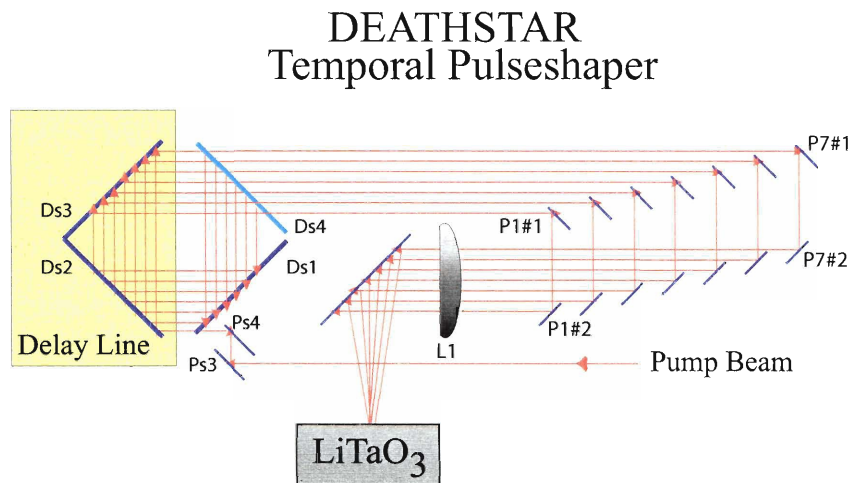


Figure 2-7: The Deathstar optical pulse shaper. Figure prepared by Jaime Choi.

A single laser pulse is introduced to the system of retro-reflectors in the pulse shaper, where it completes seven round trips around the Deathstar cavity. Each time the pulse passes the custom-designed variable reflector (part Ds4), part of the pulse is transmitted. The reflection coefficients of the different parts of the variable reflector are designed so that that temporal envelope of energies of the seven pulses leaving the pulse shaper is roughly Gaussian. The details of the variable reflector are discussed in the thesis of Dr. Jaime Choi [9]. The system of mirrors following the pulse shaper cavity compensates for the ~ 20 cm round trips that each successive pulse traverses, to temporally re-overlap the pulses when the delay line is at its zero position.

By adjusting the position of the delay line in figure 2-7 to enlarge the pulse shaper cavity, the temporal separation between successive pulses is increased evenly. When the delay line is at its maximum extension, the pulses are separated by 500 ps, resulting in a 2 GHz pulse train, and this limit could easily be lowered through use of a longer delay line. The upper frequency limit of the pulse shaper is roughly 2 THz, and is constrained here by the laser pulse duration.

The Deathstar pulse shaper was used to generate multicycle polariton radiation, but was not optimized for this purpose. In particular, two features contributed to poor polariton generation and detection. First, the RegA pulses, when cylindrically focused, are below the damage threshold of the LiTaO₃ crystal; using the Deathstar to divide this pulse into a seven pulse train provided only weak polariton generation for each pulse. To compensate for this, the pump excitation was not focused cylindrically, but to a spot of comparable size to the probe. This allowed for more intense polariton excitation, but the polaritons radiated conically away from the round excitation spot, and could not be effectively detected far from the generation location. Finally, the nonzero angles between the excitation pulses resulted in successive polariton wavefronts with small angles between them, further degrading the multicycle polariton wave and creating wavefront matching issues with the polariton probe field.

Chapter 3

Phonon-polaritons as a THz Source

Work by Dan Grischkowsky [23], David Auston, and Martin Nuss [24, 25] led to the development of broadband pulsed THz radiation sources utilizing femtosecond lasers. These advancements allowed the development of femtosecond-based sources of coherent far-infrared radiation and represented a significant technological advancement over competing THz sources. Earlier THz sources consisted of arc lamps with bolometric detection and Fourier Transform IR spectrometers that contained special far IR optics. Both of these are inherently continuous wave techniques that measure intensity and, subject to noise from thermal background radiation, are significantly less sensitive than the time gated techniques. Another important class of THz sources are synchrotron radiation and free electron lasers, but availability and expense limit their scope. Moreover, even though they are pulsed time domain sources, their pulse widths are rather long (3-10 ps) compared to the newer femtosecond based sources [1]. The THz, or far-infrared spectral region, usually considered to be 0.1-10 THz ($\lambda = 3 - 0.03 \text{ mm} \Leftrightarrow 3.3 - 330 \text{ cm}^{-1}$), is intermediate between electronic sources that can operate out into the many gigahertz regime and optical sources that can operate down to approximately the mid-infrared region. To date, THz sources based on femtosecond-laser excitation have been applied to a wide range of problems of chemical interest in both the gas and condensed phase. A comprehensive review is given by Schmuttenmaer and coworkers [1]. In comparison to more traditional IR spectroscopy which investigates intermolecular vibration, THz spec-

troscopy probes lower frequency motion, such as intramolecular modes of vibration, torsions and rotations in molecules, and phonons in solids.

The ability of THz radiation to penetrate plastics, paper, and textiles has led to a strong interest in THz technologies. THz spectroscopy has been used to noninvasively detect the chemical explosive C-4 in postal envelopes [26]. THz spectral identification, much like conventional IR spectroscopy, has gathered much interest from pharmaceutical companies, especially after THz was used to distinguish the pure enantiomers L- D- aniline from its racemic mixture [27]. THz spectroscopy has been performed on molecules within flames [28], something that would never be possible with a CW detector because of the intensity of the thermal background. In the condensed phase, both polar and non-polar liquids [29] have been studied as well biological applications like marker-free monitoring of DNA binding [30]. THz imaging has been performed on integrated chips [31], and even three-dimensional topographic imaging [32] has been demonstrated. THz sources have also been proposed for applications in coherent control [33], signal processing [34], nonlinear THz spectroscopy [35–38], and quantum computation [39].

This thesis develops a new approach to THz spectroscopy that utilizes phonon-polaritons as a time domain THz radiation source. Phonon-polaritons are coupled lattice vibrational and electromagnetic modes of an ionic crystal that travel at light like speeds. Phonon-polaritons generated in the ionic crystals LiTaO_3 and LiNbO_3 provide an attractive platform for THz spectroscopy, because of flexibility in generation and detection and the ability to integrate a THz source into a unified device. A discussion of the advantages of phonon-polaritons will be presented in chapter 4 in the context of our implementation of phonon-polariton spectroscopy. This chapter will introduce the basic theory of polaritons. Section 3.1 will introduce the basic principles and properties of polaritons. Next, Section 3.2 will introduce impulsive stimulated Raman scattering (ISRS) and its application to polariton modes. Finally Section 3.3 will introduce the basic principles of generation and detection.

3.1 Introduction to Phonon-Polaritons

Phonon-polaritons are coupled lattice vibrational and electromagnetic modes of an ionic crystal that propagate at light-like speeds with frequencies typically in the 0.1-5 THz range. A phonon-polariton is a fundamental quantized physical excitation consisting of a phonon-photon transverse wave field. Chapter 4 will demonstrate the use of localized macroscopic coherent superpositions of these excitations as a means for performing THz spectroscopy. Following the presentation of Vaughan [6], a brief theoretical description of phonon-polaritons is given below. For a more detailed analysis, the following references are useful [4, 16, 40–43].

The ionic crystals that we use for phonon-polariton generation are LiTaO_3 and LiNbO_3 . The essential character of a phonon-polariton mode stems from the coupling between transverse optic phonon modes and a macroscopic polarization. A simple mathematical model for this coupling is described by the following set of coupled differential equations.

$$\ddot{Q}(t) = -\omega_{TO}^2 Q(t) - \Gamma \dot{Q}(t) + b_{12} E(t) \quad (3.1)$$

$$P(t) = b_{21} Q(t) + b_{22} E(t) \quad (3.2)$$

$Q(t)$ is the normal coordinate of the transverse optical phonon mode with frequency ω_{TO} , Γ is a phenomenological damping constant, $E(t)$ is electric field, $P(t)$ is polarization, and $\dot{Q}(t)$ and $\ddot{Q}(t)$ represent the first and second temporal derivatives of $Q(t)$, respectively. In general, multiple modes may couple to $E(t)$, but here we will use a single oscillator model and will show later on that this is justified for LiTaO_3 and LiNbO_3 . The constants b_{12} , b_{21} , and b_{22} will be discussed below. $P(t)$, $E(t)$, $Q(t)$, etc. have been expressed as scalar quantities, which is sufficient for the present analysis. In physical terms, equation 3.1 describes a damped harmonic oscillator with an additional term $b_{12}E(t)$ governing the coupling of the polar vibrational displacements to an electric field. This coupling gives polaritons macroscopic correlation lengths and leads to dispersion in phonon-polariton propagation. Equation 3.2 describes the

dielectric response of the coupled system as the sum of two terms, where the first term describes the polarization response due to the phonon mode (essentially dipole times ionic displacement) and where the second term describes the polarization response of the crystal due to all other effects. Using equations 3.1 and 3.2 and the constitutive relation for the electric polarization $P(t)$ we will now determine the relative permittivity of the coupled system.

The constitutive relation for electric polarization in SI units is

$$\begin{aligned} P(\omega) &= \epsilon_0 \chi_e(\omega) E(\omega) \\ &= \epsilon_0 (\epsilon_r(\omega) - 1) E(\omega) \end{aligned} \quad (3.3)$$

where ϵ_0 is the permittivity of free-space, $\chi_e(\omega)$ is the dielectric susceptibility, and $\epsilon_r(\omega)$ is the relative permittivity. Inserting trial plane-wave solutions of the form $Q(t) = |Q(t)| \exp[i(kx - \omega t)]$ and $E(t) = |E(t)| \exp[i(kx - \omega t)]$ into equation 3.1 yields an expression for Q in terms of frequency.

$$Q(\omega) = \frac{b_{12} E(\omega)}{\omega_{TO}^2 - i\omega\Gamma - \omega^2} \quad (3.4)$$

Substitution of equation 3.4 into equation 3.2 yields an expression for the polarization in terms of electric field which may then be equated to equation 3.3, giving

$$P(\omega) = \left(\frac{b_{12} b_{21}}{\omega_{TO}^2 - i\omega\Gamma - \omega^2} + b_{22} \right) E(\omega) = \epsilon_0 (\epsilon_r(\omega) - 1) E(\omega) \quad (3.5)$$

Equation 3.5 may now be used to solve for $\epsilon_r(\omega)$:

$$\epsilon_r(\omega) = \left(1 + \frac{b_{22}}{\epsilon_0} \right) + \frac{1}{\epsilon_0} \frac{b_{12} b_{21}}{\omega_{TO}^2 - i\omega\Gamma - \omega^2} \quad (3.6)$$

Equation 3.6 contains two terms: the first term is nonresonant, describing the system at optical frequencies far above ω_{TO} , and the second describes the system near resonance and leads to phonon-polariton dispersion.

The constants b_{12} , b_{21} , and b_{22} will now be connected to physical quantities by considering limiting cases for the relative permittivity. When $\omega \rightarrow \infty$, the resonant

term in equation 3.6 vanishes, leaving

$$\varepsilon_r(\infty) = 1 + \frac{b_{22}}{\epsilon_0}. \quad (3.7)$$

Similarly, when $\omega \rightarrow 0$, we are left with

$$\varepsilon_r(0) = \varepsilon_r(\infty) + \frac{b_{12}b_{21}}{\epsilon_0\omega_{TO}^2}. \quad (3.8)$$

From the above equations, the constants b_{12} , b_{21} , and b_{22} are determined to be

$$\begin{aligned} b_{22} &= \epsilon_0(\varepsilon_r(\infty) - 1) \\ b_{12}b_{21} &= \omega_{TO}^2\epsilon_0(\varepsilon_r(0) - \varepsilon_r(\infty)). \end{aligned} \quad (3.9)$$

where ε_0 and ε_∞ are defined as $\varepsilon_\infty \equiv \varepsilon_r(\infty)$ and $\varepsilon_0 \equiv \varepsilon_r(0)$. Now, we may rewrite equation 3.6 as:

$$\varepsilon_r(\omega) = \varepsilon_\infty + \frac{\omega_{TO}^2(\varepsilon_0 - \varepsilon_\infty)}{\omega_{TO}^2 - i\omega\Gamma - \omega^2}. \quad (3.10)$$

Equation 3.10 was derived assuming only one oscillator mode. The crystals we use for polariton generation, LiNbO₃ and LiTaO₃, have C_{3v} lattice symmetry with four A₁ symmetry IR and Raman active modes that could be excited under our experimental conditions. There is an independent equation of the form of equation 3.10 for each of them. Table 3.1 shows the relevant parameters for each of the modes. For both LiNbO₃ and LiTaO₃ the lowest order mode has the largest oscillator strength, and this is the dominant mode observed. Additionally, the highest frequency modes have frequencies that are too high to be driven impulsively by our experimental laser pulses (250 fs duration). This justifies the use of only the single phonon mode. Each of the four modes also has its own dispersion curve. Figure 3-1 shows the dispersion curve for the dominant (lowest) A₁ mode of LiTaO₃. Two branches of solutions are obtained from the dispersion relation, an upper branch and a lower branch. An important and well-known property of LiTaO₃ and LiNbO₃ is that phonon-polaritons exhibit a large

LiNbO ₃				LiTaO ₃			
i	ω_T [THz]	Γ [THz]	S	i	ω_T [THz]	Γ [THz]	S
1	7.43	0.63	16	1	6.00	0.84	30.0
2	10.70	0.33	1.0	2	10.70	0.33	0.005
3	9.20	0.75	0.16	3	17.87	0.54	2.66
4	18.83	1.02	2.55	4	19.70	1.68	0.34

Table 3.1: A₁ symmetry transverse optical phonon modes in LiNbO₃ and LiTaO₃ obtained from ref. [44,45]. S is the coupling strength between the lattice vibration and the electromagnetic radiation.

dispersion resulting from the coupling between the polar transverse optic phonon mode and transverse electromagnetic radiation. This coupling also creates a splitting in the allowed frequencies of transverse optic phonon mode polariton propagation is forbidden. In the low wavevector limit, the upper branch of TO phonons asymptotically approaches the longitudinal optic phonon frequency ω_{LO} . In the optical regime, the dispersive properties of materials are often described in terms of a wavelength (or frequency) dependent index of refraction. Here, instead, the dispersion is customarily presented in terms of the dispersion relation $\omega(k)$. Using $\epsilon_r(\omega) = n(\omega)^2 = c^2 k^2 / \omega^2$, where n is refractive index, and assuming no damping, we obtain:

$$\omega = \sqrt{\frac{\omega_{TO}^2 \epsilon_+ + c^2 k^2}{2\epsilon_\infty} \pm \frac{1}{2} \sqrt{\left(\frac{\omega_{TO}^2 \epsilon_0 + c^2 k^2}{\epsilon_\infty}\right)^2 - \frac{4\omega_{TO}^2 c^2 k^2}{\epsilon_\infty}}} \quad (3.11)$$

As section 3.2 will show, only frequencies well below the ω_{TO} of LiTaO₃ and LiNbO₃ can be accessed within the bandwidth our femtosecond excitation pulses. This limits us to the the lower branch of the dispersion curve, and then only in the range of approximately 0.2-1 THz. In this region, the dispersion is approximately linear and the phonon-polaritons are considered to be primarily light-like. This is the useful regime for polariton spectroscopy.

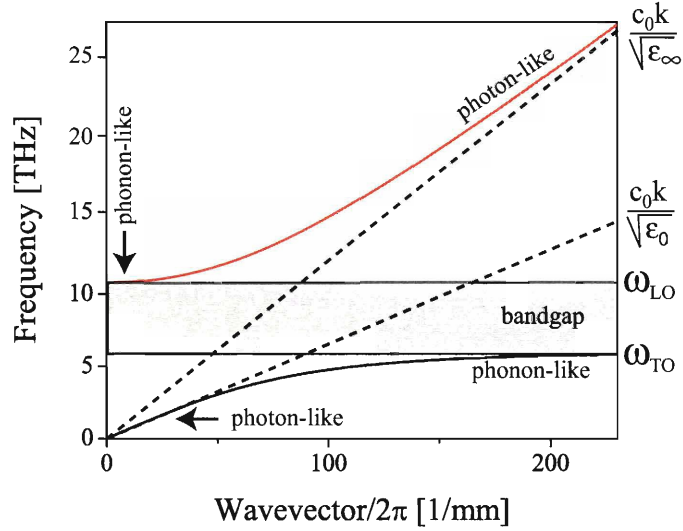


Figure 3-1: Simulated phonon-polariton dispersion curve for LiTaO₃. The solid lines indicate the upper and lower polariton branches. The dashed lines describe the dispersion of uncoupled optical radiation. The band gap describes the region where phonon-polariton propagation is forbidden. The lower branch at low wavevector is the region of interest for our experiments.

3.2 Impulsive Stimulated Raman Scattering

The phonon-polaritons that we utilize for polariton spectroscopy are generated via impulsive stimulated Raman scattering (ISRS) by irradiating either LiTaO₃ or LiNbO₃ with a short (<250 fs) laser pulse. Here we present ISRS in the general case of a single vibrational mode and then we extend it to the phonon-polariton modes, which because of their coupled nature behave differently than ordinary vibrational modes.

A basic physical picture of ISRS is that a femtosecond optical excitation pulse, with frequencies too high to drive a lattice vibration resonantly, instead drives the lattice vibrational modes indirectly through nonlinear coupling to the electrons. The electrons drive the lattice at much lower resonance frequencies (THz in our case) via difference frequency mixing among frequency components within the bandwidth of the pulse. A convenient mathematical description of ISRS in the time domain is given in terms of a damped and driven harmonic oscillator, described by the differential equation below.

$$\ddot{Q}(t) + \Gamma\dot{Q}(t) + \omega_0^2 Q(t) = F(t), \quad (3.12)$$

Q is the normal mode coordinate of a generic vibrational mode with resonant frequency ω_0 , a damping term governed by Γ , and a driving term $F(t)$. Here, the driving term is due to an optical laser excitation pulse. In the “impulsive” limit, where an excitation pulse is much shorter than the period of the mode being excited, the force exerted by the laser excitation pulse is proportional to the product of the differential polarizability $(\partial\alpha/\partial Q)_0$ and the intensity of the excitation pulse $I_{exc}(t)$ [46, 47],

$$F(t) \propto \left(\frac{\partial\alpha}{\partial Q} \right)_0 I_{exc}(t). \quad (3.13)$$

If we consider the solution of equation 3.12 when the input laser pulse is taken to be a delta-like pulse that arrives at time $t = 0$, the impulse response function of the oscillator, $G(t)$, may be determined to be

$$G(t) \propto \Theta(t) \exp\left(-\frac{\Gamma t}{2}\right) \sin(\sqrt{\omega_0^2 - \Gamma^2/4}t) \quad (3.14)$$

where $\Theta(t)$ is the Heaviside step-function given by:

$$H(t) = \begin{cases} 0 & t < 0 \\ 1 & t > 0. \end{cases} \quad (3.15)$$

The Heaviside step-function is necessary such that $G(t)$ obeys causality and is zero for negative times. When an input pulse $I(t)$ of short but finite duration is used, $Q(t)$ may be determined by convolving the input pulse with $G(t)$, such that

$$Q(t) = I_{exc}(t) \otimes G(t). \quad (3.16)$$

From equations 3.16 and 3.14, the expected response for a single underdamped vibrational mode is therefore a exponentially damped sinusoid. For multiple oscillators the total signal is given by the sum of the individual oscillators.

The range of vibrational frequencies accessible by the input laser pulse is a simple function of the duration of $I_{exc}(t)$, ~ 3 THz for our pulse duration of ~ 250 fs. We will describe the duration of our pulse as Gaussian, $I_{exc}(t) \sim I_o \exp(-\Delta\Omega^2 t^2/4)$, where $\Delta\Omega$ is the full-width half maximum of the laser pulse spectral intensity (which is inversely proportional to the pulse duration and where we have omitted the high-frequency intensity oscillations that do not contribute to the response). The range of available frequencies can then be determined by substituting equation 3.14 into equation 3.12, to yield:

$$Q(\omega) \propto \frac{\exp(-\omega^2/\Delta\Omega^2)}{\omega_o^2 - \omega^2 - i\Gamma\omega}. \quad (3.17)$$

To excite a vibrational mode in an approximately “impulsive” manner, the duration of the excitation laser pulse must be shorter than half of an oscillation period. From the inverse relationship between bandwidth and pulse duration, this necessarily implies that the pulse must have both the pump and Stokes frequency in stimulated scattering. This requirement can be seen in equation 3.17, where $\omega/\Delta\Omega$ must be sufficiently small for normal mode amplitude $Q(\omega)$ to be nonzero. This connects with the time and frequency domain descriptions of stimulated Raman scattering. Unlike conventional stimulated Raman scattering, where the pump and Stokes beams each consist of a single frequency, for ISRS, there is a continuum of pump and Stokes frequency pairs contained within the bandwidth of the laser pulse, all of which contribute to the response of the sample.

3.3 Generation and Detection of Phonon-Polaritons

3.3.1 Phonon-Polariton Generation

In the case of phonon-polariton modes, equation 3.1 can be modified to include the driving term $F(t)$, giving

$$\ddot{Q}(t) + \omega_{TO}^2 Q(t) + \Gamma \dot{Q}(t) - b_{12} E(t) = F(t), \quad (3.18)$$

which together with equation 3.2, describes the excitation of phonon-polariton modes. Unlike the general case where the motion of a given oscillator is essentially independent of the motion of other oscillators that are many unit cells away, phonon-polaritons show strong dispersion at long wavelengths due to long-range interactions among oscillators. This is caused by the coupling of oscillators through the electric field $E(t)$. Because of this collective behavior, the observed frequency of phonon-polaritons generated via ISRS is a function of the phonon-polariton wavevector, as seen in figure 3-1.

Another difference between phonon-polariton modes and ordinary vibrational modes is that phonon-polaritons, which are light-like in the experiments reported here, propagate rapidly across macroscopic distances in the host crystal. The group velocity, given by $\partial\omega/\partial k$, is a significant fraction of the speed of light in vacuum, as is evident in figure 3-1. In LiTaO₃ and LiNbO₃, it is approximately 1/6 the speed of light in vacuum ($n \approx 6$). As a consequence of this propagation speed, when polaritons are generated inside LiTaO₃ and LiNbO₃ via ISRS, they propagate in a mostly perpendicular direction to the excitation pulse with a small forward component. The angle at which the phonon-polaritons propagate is a simple geometric function of the group velocity of the excitation pulse, v_{exc} and the phase velocity of the phonon-polariton, v_{pol} . If the excitation pulse arrives at normal incidence, then relative to the front surface the the polariton waveform propagates at an angle θ_f , given by,

$$\theta_f = \arcsin\left(\frac{v_{pol}}{v_{exc}}\right). \quad (3.19)$$

A useful analogy is that phonon-polaritons resemble the wave left behind a boat that travels quickly across a pond, as seen in figure 3-2. In LiTaO₃ $\theta_f(\omega)$ is approximately 20°, and its frequency dependence is negligible for our purposes. A large THz frequency refractive index contrast between LiTaO₃ and air leads to a critical angle for total internal reflection of phonon-polaritons of only ~10°. This implies that the generated polariton waveform does not exit the crystal to air. Figure 3-3 shows a generated polariton waveform undergoing total internal reflection as it propagates

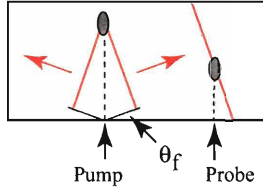


Figure 3-2: Phonon-polariton generation and detection with a short femtosecond excitation pulse.

between the back and front of the crystal while moving primarily to the right in the figure. The forward angle and critical angles for LiNbO_3 are similar to those of LiTaO_3 .

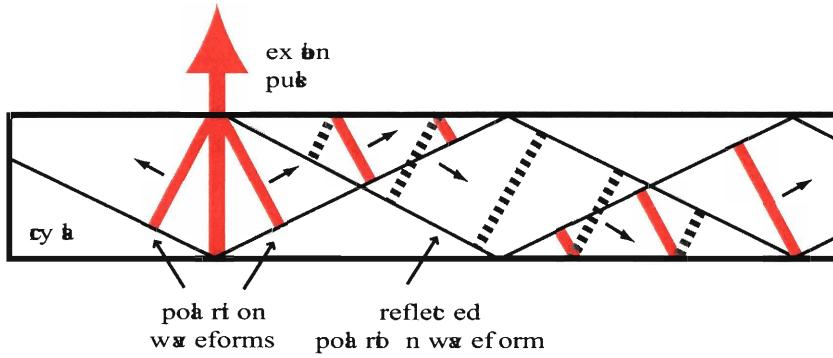


Figure 3-3: Schematic illustration of a propagating polariton waveform generated with a femtosecond excitation pulse. The right propagating polariton waveform is emphasized to show that although the primary direction of propagation is lateral, the polariton waveform undergoes total internal reflection as it propagates between the front and back surfaces.

3.3.2 Phonon-Polariton Waveforms

This section relates the polariton waveform to the spatial profile of the optical excitation beam. In one dimension it can be shown analytically that, in the impulsive plane wave excitation limit, the observed THz waveform $E(x, t)$ resembles the spatial derivative of the excitation beam profile $I_{exc}(x)$ [48, 49].

$$E\left(x \pm \frac{ct}{n}, t\right) \propto \pm \partial_x I_{exc}(x) \quad (3.20)$$

where c is the speed of light in vacuum and n is the THz frequency index of refraction which is nearly constant at frequencies well below the phonon resonance. Note that the \pm is necessary as there are two identical polariton waveforms are excited that propagate in nearly opposite directions. Figure 3-4 shows an excitation condition

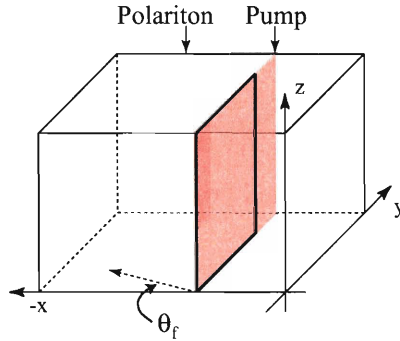


Figure 3-4: The excitation pulse is focused to a line. This launches a phonon-polariton plane wave generated throughout the volume of the crystal. The right propagating polariton waveform is not shown.

commonly used in our polariton spectrometer implementation, a cylindrically focused excitation pulse with a gaussian spatial profile that is focused to a line in along the x dimension. The intensity in the z dimension can be taken as approximately constant. Equation 3.20 then shows that the spatial derivative of the gaussian excitation profile gives a single-cycle polariton plane wave that occupies the entire height of the crystal and is non-divergent. For our typical focal parameters this results in a spatial width of $\sim 70 \mu\text{m}$ and temporal a width on the order ~ 1 ps peak-to-peak in the time domain. In practice the height of the line excitation is on the order of the generation crystal and often slightly larger. Because of this, and since the polariton waveform is probed typically only at a small spot at a z position nominally midway between the top and bottom of the crystal, the gaussian profile of the excitation pulse in the z dimension can be ignored and the polariton wave packets can be thought of as plain waves. The direction of propagation of the two polariton waveforms (the right propagating polariton waveform is not shown in figure 3-4) is in the x direction with a small y component, given by the forward angle. Equation 3.20 can be extended for spatial variation in the y dimension, and an equivalent 1D equation for the y dimension can

be written. Then the temporal profile of the polariton is given by the sum of E_x and E_y . For example, a gaussian beam focused to a spot generates a single cycle polariton waveform that radiates out in a conical direction with a cone angle given by the forward angle.

3.3.3 Phonon-Polariton Detection

Phonon-polaritons may be detected in a variety of ways, but most of them rely upon the Pockel's effect [21,22] in which an electric field modulates the index of refraction of a material. For the experiments reported here in the uniaxial crystals LiTaO₃ and LiNbO₃, the phonon-polaritons and laser excitation pulse are polarized parallel to the optic axis of the crystal (z direction), which in figure 3-3 points out of the page and in figure 3-4 points in the vertical (z direction). Analysis of the electro-optic tensor for LiTaO₃ and LiNbO₃ [21,22] yields the following equations for the ordinary ($n_o(E_{pp})$) and extraordinary ($n_e(E_{pp})$) indices of refraction at optical wavelengths in the presence of a THz electric field E_{pp} polarized along the extraordinary crystal axis,

$$n_e(E_{pp}) - n_e = -\frac{n_e^3}{2}r_{33}E_z \quad (3.21)$$

$$n_o(E_{pp}) - n_o = -\frac{n_e^3}{2}r_{13}E_z, \quad (3.22)$$

where r_{13} and r_{33} are the relevant electro-optic tensor elements, and n_e and n_o are the extraordinary and ordinary refractive indices in the absence of an applied field (see table 3.2). Many schemes can be used to detect these refractive index variations, but

material	n_o	n_e	r_{13}	r_{33}
LiNbO ₃	2.257	2.176	9.6	30.9
LiTaO ₃	2.176	2.180	8.4	30.5

Table 3.2: Constants for modulation of the index of refraction due to phonon-polaritons from reference [22]. Units for r_{13} and r_{33} are pm/V.

we will focus on interferometric detection. The phase shift induced by the polaritons

in the optical probe polarized along the extraordinary axis is given by:

$$\phi = \frac{(-n_e^3 r_{33} E_z) \omega L}{2c}, \quad (3.23)$$

here ω is the probe frequency and L is the interaction (wavefront) length. In our experiments, the electric field amplitude E_{pp} is small and the phase shift results in linear changes in signal. The measured phase shift is an integral over the phase shifts encountered by the probe pulse as it passes through the crystal, therefore to obtain quantitative measurements of the polariton amplitude it is necessary for the probe to measure the same phase point of the polariton field as it probes along the entire wave front of the polariton. In the analogy of a phonon-polariton wave resembling the wake left behind a boat traveling across a lake, the above condition is equivalent to requiring that the probe pulse act like a second boat that “surfs” along the first boat’s wake always at a fixed point of the oscillation cycle. This occurs automatically if the pump and probe beams both enter the crystal at the same angle, and have the same spectral content (implicitly the same group velocities). This is the most common condition for our experiments. If the pump or probe beam are of different wavelengths (for example, if the probe beams have been frequency-doubled from 800 to 400 nm), then the group velocity of the probe is no longer matched to the projection of the phonon-polariton phase velocity along the direction of the probe. This may be compensated for by having the pump and probe beams enter the crystal at different angles determined by the difference in group velocities.

Chapter 4

Development of Phonon-Polariton Based THz Spectroscopy

This chapter will demonstrate three configurations of simple, compact THz spectrometers based on measurement of phonon-polariton wavepacket propagation before and after interaction with a sample. Section 4.1 will motivate the use of phonon polaritons as a platform for THz spectroscopy. Next, section 4.2 will introduce the basic principles of phonon-polariton spectroscopy and section 4.3 will then show how the complex index of refraction can be extracted from measurement of the phase and amplitude of the polariton wavepacket. Section 4.4 will present some selected measurements obtained from the three spectrometer configurations. Then sections 4.5 and 4.6 will present some experiments that utilize free space THz radiation with traditional detection methods and a comparison to phonon-polariton based spectroscopy. Next section 4.7 will demonstrate simple pulse shaping techniques to generate multicycle polariton wavepackets. Finally, section 4.8 will summarize the polariton spectroscopy experiments and discuss future direction and experiments.

4.1 Motivation of Phonon-Polaritons as a THz Source

There has been a long standing effort in the Nelson group to develop optical pulse shaping techniques [50–58] to generate [59–61], visualize [2, 62, 63] and control [64, 65]

polariton lattice vibrational waves. Much of the early work was motivated by the desire to transfer more of the excitation energy to the polariton excitations by spreading out the laser excitation pulse over space and time. Although the conversion efficiencies of LiTaO_3 and LiNbO_3 are quite high compared to other ferroelectric crystals, only about $10^{-3}\%$ of the energy in a simple 800 nm excitation pulse is typically converted into polaritons. Moreover, even moderate focusing of the excitation beam can cause irreversible damage in these crystals through ablation. For our purposes here, we will divide pulse shaping into two classes. The first is simple spatial pulse shaping where a static mask is imaged into a sample. This type of shaping has proven extremely useful for its simplicity and robustness. Multicycle polariton waveforms have been generated by imaging binary phase mask patterns into LiTaO_3 and LiNbO_3 [14]. A second important example of this approach is echelon based phonon-polariton amplification, where an echelon temporally delays different spatial slices of an excitation pulse so those slices amplify a propagating polariton pulse by constructive interference with polaritons generated at different spatial positions. Because the echelon is made of glass (a stack of optical quality glass slabs), it can shape the full power of the optical excitation pulse (typically upto 4 mJ), which is substantially more laser energy than the programable pulse shaping method described subsequently can withstand. For this reason, the glass echelon is preferable for intense polariton generation, and such an echelon with a laser excitation pulse of 1.5 mJ has been used to generate polariton fields of greater than 50 kV/cm [6].

Our second class of pulse shaping techniques are dynamical techniques where the waveform generated can be programmably changed by a computer. The Nelson group developed an optical pulse shaper based on a Hamamatsu 2D liquid crystal spatial light modulator and applied it to the generation and manipulation of polaritons [54, 55]. These efforts have shown remarkable success and have demonstrated versatile programmable spatiotemporal control over phonon-polaritons with the use of all optical pulse shaping techniques [65–67]. These techniques compare favorably to other THz pulse shaping methods which have utilized either temporal-only shaped femtosecond excitation waveforms [68–71] to excite THz radiation in traditional THz

media (GaAs, ZnTe, GaSe) or specially fabricated materials or devices [72–74], with limited results in terms of the complexity and fidelity of the THz waveforms generated. The ability to completely control THz waveforms in both time and space offers many possible advantages, including multiplexing of THz waveforms into and out of patterned materials as well as generating and crossing multiple THz pulses in bulk crystals.

In addition to the pulse shaping work, there has been a parallel effort in the Nelson group to develop an integrated solid-state platform for polariton (THz) signal generation and guidance [4, 34, 75]. Femtosecond laser machining has been used to build waveguide and optical device structures in LiTaO₃ and LiNbO₃ crystals. Channels, on the order of 100 μm wide, are created by removing crystalline material through femtosecond laser ablation. Many simple structures have been demonstrated, including a reflective focusing element, a 90° waveguide turn and a diffraction grating. A more complex optical apparatus has also been demonstrated, a structure consisting of splitting and recombining elements that can be used as a THz Mach-Zehnder interferometer [76] for spectroscopy. These structures permit integrated THz signal generation, propagation through waveguide-based devices, and readout within a single compact solid-state platform. A second example of complex optical device, a resonator structure, was built and used to amplify multicycle polariton waveforms in the 50 to 250 GHz range [77]. To complement this work, finite difference time domain (FDTD) simulations on a 24 processor Beowulf cluster were performed [4, 78] to understand the propagation of complex polariton waveforms in these patterned materials.

Although there are multiple applications of this work such as signal processing and investigation of nonlinear lattice potentials [79], much of the work has been directed towards developing a platform for THz spectroscopy. This thesis presents the first quantitative measurements of the dielectric properties of samples other than the generation crystals using phonon polaritons.

4.2 Phonon-Polariton Based THz Spectroscopy

4.2.1 Principles

The use of phonon-polaritons generated in an ionic crystal through impulsive stimulated Raman scattering (ISRS) as a source for THz spectroscopy suggests itself because of the versatility of polariton waveform shaping and detection. To emphasize a few concepts that were developed in chapter 3, phonon-polaritons are lattice waves of an ionic crystal that propagate at light-like speed. When a line focus is used, two symmetric polariton planewaves are launched in opposite lateral directions that are nominally perpendicular (with a small forward component) to the incident excitation beam. For a single femtosecond excitation pulse, the polariton waveform profile is determined by the spatial derivative of the optical excitation beam profile, so cylindrically focused gaussian pulses yield single-cycle polariton plane waveforms.

This chapter will present three configurations of the spectrometer apparatus, namely a single generation crystal, reflection mode, and transmission mode. In the single crystal configuration, the material parameters of the generation crystal are measured. It is necessary to know these parameters accurately because polariton propagation in these crystals must be accounted for in the other spectrometer configurations. Figure 4-1 shows the transmission configuration, with the generation and detection crystal cut to compensate for the forward angle. In all three spectroscopic implementations, a polariton wavepacket induces a modulation in the crystal's refractive index that is detected through the use of a compact, grating-based interferometer. The polariton waveform is measured before and after interaction with the sample, permitting measurement of the phase and amplitude of the polariton electric field on both sides of the sample.

Figure 4-1 depicts one version of our spectrometer apparatus but illustrates many of the basic concepts associated with polariton spectroscopy. From a top view, it shows the polariton wavepacket propagating from the region of generation in the ionic crystal on the right, to the crystal edge where the polariton partially reflects and partially couples THz radiation into the sample. After that, THz radiation prop-

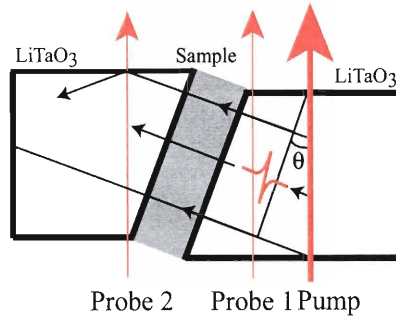


Figure 4-1: Top view - Schematic illustration of polariton-based transmission THz spectroscopy cell. The pump beam is focused to a line, and the polaritons are generated throughout the depth of the cell. The LiTaO₃ crystals are cut to compensate for the forward polariton wavevector component. The pump excitation also generates a right propagating polariton waveform that is not involved in the experiment and is not shown.

agates through the sample, couples into the second crystal as a polariton waveform, and then propagates through the second crystal where it is detected. Measurement of the transmitted and reflected polaritons allows determination of the complex dielectric constant. The generation crystals are cut such that polariton transmission occurs at approximately normal angles, compensating for the forward wavevector component of the polariton waveform. Note that many variations of the arrangement shown in figure 4-1 are possible. For example, if the dielectric contrast between LiTaO₃ and the sample is not too great (such that total internal reflection does not occur at modest angles of incidence), then compensation for the forward wavevector component may not be necessary. A purely reflection-mode arrangement, in which polaritons are generated and detected in the same LiTaO₃ crystal, is also possible. The THz radiation that is transmitted through the sample may be coupled into free space rather than a second LiTaO₃ crystal, and more conventional THz detection methods may be used, and this is done in the free space THz measurements presented. This thesis will use the term polariton spectroscopy to refer to situations in which phonon-polaritons are not coupled into free space.

Another transmission version of our spectrometer will be used to demonstrate some additional features. The example illustrated in figure 4-2 shows the raw data

from a transmission cell with “uncut” crystals, that is, crystals that are not cut at an angle that compensates for the forward propagation angle. Because the crystals are uncut, the reflections from the sample can be observed since the reflected beam retains the correct forward angle for the probe to measure a constant phase of its wavefront. The time at which a peak is observed depends on the distances A, B, and C in figure 4-

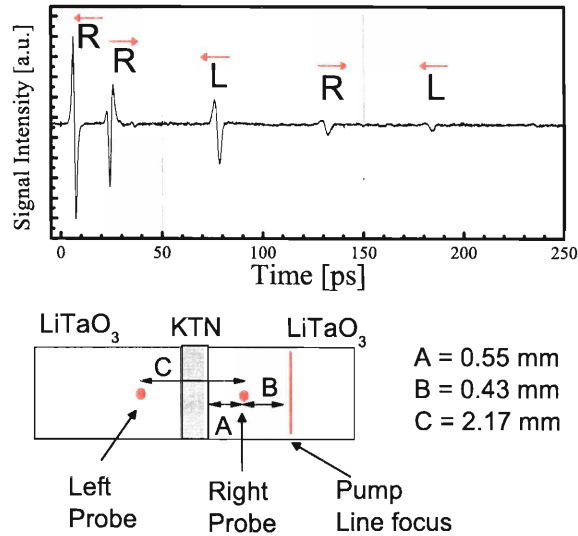


Figure 4-2: Side view THz transmission cell. The LiTaO₃ crystals are not cut to compensate for the forward propagation angle of the polariton waveform, and as such, polariton reflections are observed. The raw data shows the propagation of the left propagating polariton waveform. The labels R and L on the peaks in the raw data refer to interferometric measurements at the right and left probe arms and the arrows show the direction of polariton propagation. In chronological order, the first peak is the polariton waveform arriving at the right probe arm, the second peak is the reflection from the pump side of the sample measured at the right probe arm, the third peak is propagation through the sample arriving at the left probe arm, the fourth peak is reflection from the far side of the sample at the right probe arm, and the fifth peak is the polariton after two reflections arriving at the probe arm. Peak identification can be aided by translating the cell with respect pump and probe beams to see how the peak positions change.

2. Those distances are chosen experimentally so that only one polariton field interacts with one probe arm at a time. Peak identification can be complicated for time series

where many peaks arise from both transmission and reflection, but identification can be greatly simplified by translating the spectrometer cell with respect to the pump and probe beams. This effectively changes distance A in Figure 4-2, which changes the times at which the reflected THz waves are measured. The transit times of transmitted THz waves do not depend only on the distances B and C and are not affected by changes to the A distance. If pulse identification still proves difficult, the separation between the probe arms, C, can also be easily change by modifying the grating interferometer. The coupled nature of the polariton allows for the polariton to be probed in a direction transverse to the direction of propagation. It can be probed at any point in the propagation path and, from superposition, it can be detected without altering the polariton. These traits are unique feature of Polariton spectroscopy.

Figure 4-3 demonstrates quantitatively how the frequency range of the spectrometer can be adjusted by changing the spot size of the pump beam in the horizontal direction (“x” in figure 3-4). The temporal shape of the THz pulse is related to the spatial derivative of the optical excitation profile. The focal parameters and polariton bandwidths shown in Figure 4-3 are typical. Many experiments in this thesis explore temperature dependent features and were performed in a cryostat. This limited the minimum focal lengths and consequently the single cycle pulse excitations were limited to sub-THz frequencies. Higher frequencies can be generated using temporal pulse shaping or by crossing excitation pulses into the sample, as demonstrated in section 4.7.

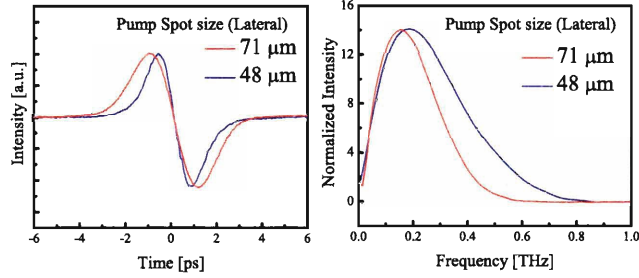


Figure 4-3: In LiTaO_3 , a line excitation is focused along the horizontal dimension with a cylindrical lens with a focal length of 30cm (red) and 20cm (blue). The polariton pulse shape is related to the spatial derivative of excitation profile. A tighter focus results in a shorter pulse in the time domain and a correspondingly larger bandwidth.

4.2.2 Crystals

This section outlines the ionic crystals used for generation and detection; their important properties and the geometries used for THz Spectroscopy. The crystals typically used are stoichiometric LiTaO_3 and LiNbO_3 , or congruent MgO doped LiNbO_3 , all of which are x-cut so the optic axis is vertical, and are approximately 1 to 2 mm thick in the direction of excitation pulse propagation. These ferroelectric crystals are chosen for their large electro-optics coefficient and nonlinear optical properties, as well as their commercial availability. The crystal structure is tetragonal and has C_{3v} symmetry. Although most of the experiments in this thesis were performed using LiTaO_3 as a generation and detection material, LiNbO_3 or MgO: LiNbO_3 have much stronger responses and are preferable. It is known that at low temperatures (<70 K) reversible photorefractive damage occurs in these materials from charge liberation and trapping effects [19], and this is observed in our experiments as increased scattering of the optical pump and probe light. MgO doped LiNbO_3 has a significantly higher photorefractive damage threshold. In the transmission experiments the crystals are often cut to compensate for the forward angle. In this case, each arm of the interferometer goes through a separate crystal. To ensure that both crystals are cut at the same angle and have the same thickness, they are obtained by cutting a single

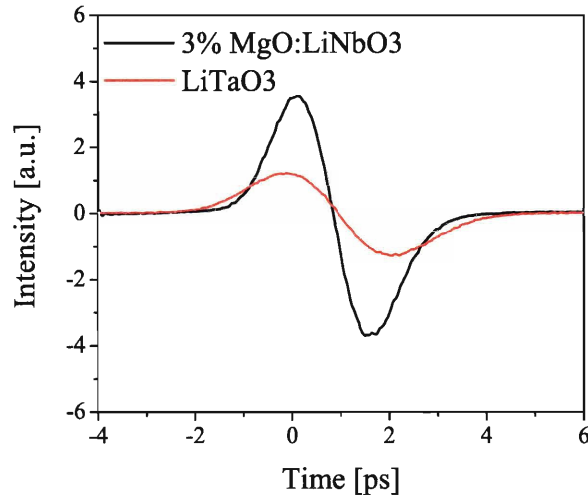


Figure 4-4: Comparison of detected polariton intensity in LiTaO_3 and 3% $\text{MgO}:\text{LiNbO}_3$. Both the generation and detection efficiencies are stronger in LiNbO_3 .

larger crystal. Cutting was performed at the MIT Crystal Grown Shared Experimental Facility using a South Bay Technology 810 Wire Saw. The cut surfaces were then polished using 300 nm grit diamond paste with the cut crystal mounted in a special jig to ensure the the polishing did not change the angle of the cut.

Figure 4-5 shows a cut crystal recombined and compared to an identical uncut crystal using the same alignment. A $\sim 5\%$ loss is observed in the area of the transmitted peak. The polaritons have much longer wavelengths ($\sim 1500 \mu\text{m}$ in air, $\sim 250 \mu\text{m}$ in LiTaO_3 , at 100 GHz) than optical light and are much less sensitive to surface roughness. Although the THz index contrast between LiTaO_3 and air is large, so that a wave at normal incidence would ordinarily undergo a 50% reflection, the gap between the two crystal when the are in pressed physical contact is far smaller than the THz wavelengths so the coupling between crystals is almost 100%.

Section 4.3 will show that compensating for the forward angle is critical to extracting the proper value for the dielectric constant. This may be done numerically for the single crystal and reflection measurements, but can only be partially done for

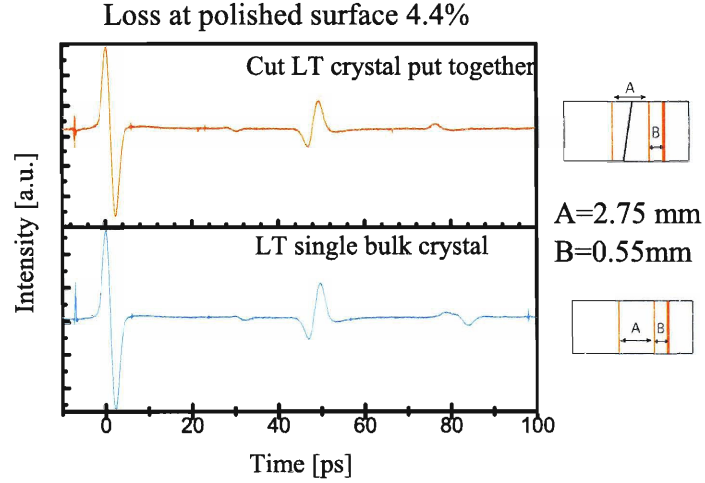


Figure 4-5: Comparison of uncut LiTaO_3 was to a cut LiTaO_3 crystal that has been physically pressed together. A 5% transmission loss was calculated from comparing the excitation peak to the transmitted peak.

the transmission experiment. Section 4.4.1 will show that the polariton group velocity in the generation crystal has a significant temperature dependence. This changes the angle of the forward component by a couple of degrees as the temperature is varied from 300 to 4 K. The angle of the forward component is given in chapter 3 and restated here,

$$\theta_f = \arcsin\left(\frac{v_{pol}}{v_{exc}}\right) \quad (4.1)$$

where v_{exc} is the group velocity of the 800nm excitation pulse, and v_{pol} is the phase velocity of the polariton waveform.

4.2.3 Phonon-Polariton Detection

A polariton waveform propagating through a crystal interacts with the crystal lattice and modulates the local index of refraction via the Pockel's effect, as is discussed in section 3.3.3. LiTaO_3 and LiNbO_3 were chosen for their strong coupling, which generates intense polariton fields, but this also necessarily implies strong coupling between the polariton field and the optical probe. The polariton waveforms are easily

detected through a variety of techniques that utilize the Pockel's effect. Polaritons are macroscopic propagating excitations, they can be imaged in real space, and a sequence of images displayed sequentially exhibits that motion as a movie. The polaritons also diffract light through refractive index modulation, and in particular for many-cycle waveforms with a well defined wavevector, such as those that will be displayed in section 4.7, diffraction can be a convenient probe. Birefringence and polariton field induced second harmonic generation are additional methods that may be used for detection.

The experiments in this chapter utilize an interferometric approach for detection. A compact grating-based, dual probe arm interferometer [13,80] is used to measure the propagating polariton waveform at two different spatial locations. The interferometer uses transmissive gratings (i.e. the binary phase mask patterns introduced in section 2.4) and common lenses for generation, imaging, and recombination of the dual probe arms. The use of all common path optics provides excellent phase stability without the need for an active feedback loop. One advantage of polariton spectroscopy is that the polariton field can be measured non-invasively at any point in its propagation path. The detection positions are chosen by selecting the separation between the interferometer arms and translating the compact polariton apparatus with respect to the pump and probe beams. Figure 4-6 illustrates the grating interferometer with

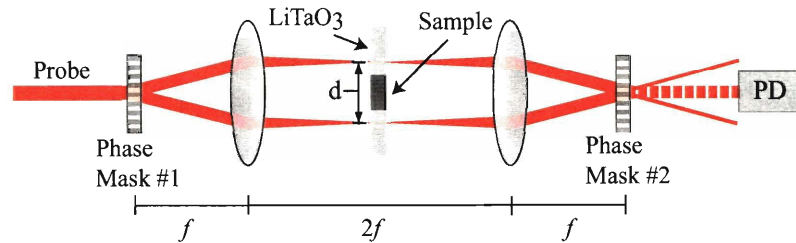


Figure 4-6: The dual arm interferometer measures the THz pulse before and after interaction with the sample.

a transmission spectrometer cell. The ± 1 orders of diffraction are collimated and

focused through the spectrometer cell by the first lens. A second lens recombines the two probe arms by focusing them into the transmissive grating where the +1 order of “Probe 1” diffracts collinearly with the −1 order of “Probe 2”. The relative phase shift of these two diffracted probe beams provides our measured signal. The separation between the probe arms are selected by choosing the grating spacing of the phase masks. The phase masks were introduced in the discussion of the transient grating experiment in section 2.4. The gratings are available in periods of 4 to 200 μm , which corresponds in our setup to probe arm separations of 72 to 1.4 mm respectively. Typically a grating period of 120 μm is used to create a probe arm separation of ~ 2.4 mm. This is calculated from the first order diffraction angle, θ_d ,

$$\theta_d = \arcsin\left(\frac{\lambda}{\Lambda_G}\right) \quad (4.2)$$

where λ is the wavelength of the diffracted light and Λ_G is the period of the diffraction grating. The separation of the probe beams, d , shown in Figure 4-6 is from simple geometry by,

$$d = 2f \tan(\theta_d) \quad (4.3)$$

where f is the focal distance. A focal distance of 18 cm is used to ensure that the Ralleigh range of the probe focus is longer than the crystal thickness. The distances between the two probe arms and the excitation beam was measured by imaging onto a CCD camera.

There are two critical points that were introduced 3.3.3, and that need to be emphasized here. First, the optical refractive index modulation due to the presence of the polariton is proportional to the strength of the THz field, E_{pp} , and is restated here,

$$n_e(E_{pp}) = n_e - \frac{n_e^3}{2} r_{33} E_{pp} \quad (4.4)$$

$$n_o(E_{pp}) = n_o - \frac{n_e^3}{2} r_{13} E_{pp}. \quad (4.5)$$

Second, the phase shift is proportional to both the change in the refractive index and

the length of interaction with the altered refractive index. A polariton waveform is a macroscopic coherent waveform, and for quantitative results, the probe beam must interact with the same portion of the waveform at different spatial positions in the crystal. This condition is guaranteed by using 800nm light for both the excitation and probe pulses, and having the pulses enter the crystal at normal incidence.

Finally, we derive the measured signal in the interferometric measurement. Both probe arms are imaged with at the same angle with the same optics onto second grating, consequently the portions of the two probe beams that are diffracted in the collinear direction have the same intensity. Define the amount diffracted from each probe are as E_{P1} and E_{P2} where $|E_{P1}| = |E_{P2}| = E_0/2$. The intensity of the signal at the photodiode detector is given below,

$$I \propto |E_{P1} + E_{P2}| = E_0^2 (1 + \cos[\Delta\phi + \phi_0]) \quad (4.6)$$

where $\Delta\phi = \phi_{P1} - \phi_{P2}$ is the phase difference between the two probe beams, and ϕ_0 is the relative phase shift from the two diffraction gratings and any difference in the crystal samples. Equation 4.4 shows that for the case of a polariton waveform propagating through the path of Probe 1 with an interaction length L ,

$$\Delta\phi_{P1} = -\frac{n_e^3 r_{33} E_{pp} \omega L}{2c} \quad (4.7)$$

and for the case of a polariton in path of Probe 2 there is an equal phase shift only of opposite sign,

$$\Delta\phi_{P2} = \frac{n_e^3 r_{33} E_{pp} \omega L}{2c}. \quad (4.8)$$

Experimentally, the phase of the second diffraction grating can modulated through multiples of 2π by translation, and the second diffraction grating is used to set the constant phase, ϕ_0 , to $\pi/2$. This is where the interferometry is most sensitive and, in the limit of small polariton fields, linearly related to the phase shift. Consider the case of the polariton waveform in Probe 1. Using the trigonometric relation

$\cos(\theta + \pi/2) = -\sin \theta$, equation 4.6 becomes,

$$I \propto E_0^2 \left(1 - \sin \left[-\frac{n_e^3 r_{33} E_{pp} \omega L}{2c} \right] \right). \quad (4.9)$$

In our experiments the polariton field is small, and the intensity at the detector can be approximated using the small angle approximation,

$$I \propto E_0^2 + E_0^2 \left(\frac{n_e^3 r_{33} E_{pp} \omega L}{2c} \right). \quad (4.10)$$

In these experiments we utilize dual frequency chopping, where the pump is chopped at f_1 and the probe is chopped at f_2 , and a lockin amplifier is used to measure signal at the sum frequency, $f_1 + f_2$. This is necessary as the probe has a constant background on the detector, and chopping only the pump causes the scattered pump light to overwhelm the signal. The AC component of the signal is given by

$$I_{AC} \propto E_0^2 \left(\frac{n_e^3 r_{33} E_{pp} \omega L}{2c} \right). \quad (4.11)$$

For the alternate case where the polariton waveform is in Probe 2, the phase shift has the opposite sign and consequently so does equation 4.11.

4.3 Dielectric Function from THz Spectroscopy

This section explains the method of data extraction for each of the three spectroscopic configurations and for free space techniques. The goal is to extract n and κ by selecting and comparing two pulses from the time series data scan.

Often in the literature, there are different but equivalent preferences for describing dielectric properties of a material. The wave propagation constants n and κ , the complex dielectric constant ε , and complex dielectric susceptibility χ_e are all equivalent ways of describing the dielectric properties of a material. For purposes of polariton spectroscopy, the wave propagation constants, i.e. the refractive index n and the extinction coefficient κ , seem natural. Although we will use κ it is sometimes convenient

to use a related quantity, α , the absorption coefficient. They are related by

$$\alpha = \frac{2\omega\kappa}{c}. \quad (4.12)$$

κ is preferred since, unlike α , it is unitless and it has no inherent frequency dependence.

In connecting our results to the ferroelectrics community however, the complex dielectric constant $\varepsilon = \varepsilon' + i\varepsilon''$ will be preferred. In a dielectric material n and κ are related to the dielectric constant by [41],

$$\varepsilon' = n^2 - \kappa^2 \quad (4.13)$$

$$\varepsilon'' = 2n\kappa \quad (4.14)$$

and often $\kappa \ll n$, so $\varepsilon' \approx n^2$. The dielectric constant is related the dielectric susceptibility in SI units is given by,

$$\varepsilon = 1 + \chi_e. \quad (4.15)$$

In an isotropic or cubic medium equation 4.15 is scalar, which for our purposes is sufficient. Finally we note that although the dielectric susceptibility and the dielectric constant are unitless, by convention $\chi_{SI} = 4\pi\chi_{CGS}$, but $\varepsilon_{SI} = \varepsilon_{CGS}$ [41].

4.3.1 Method of Data Extraction

This section explains the method of data extraction. All configurations of our phonon-polariton spectrometer measure the phase and amplitude of the polariton electric field before and after interaction with a sample. From these two measurements the frequency dependent refractive index, n , and the extinction coefficient, κ , at THz frequencies can be obtained by inverting a frequency domain transfer function, T , that governs the propagation of the polariton wavepacket.

$$E_2(\omega) = T(\omega, \{d_i, n_i, \kappa_i\})E_1(\omega) \quad (4.16)$$

where ω is the angular frequency, d_i is the distance traveled by the polariton wavepacket in a given material, and i counts the number of materials that interact with the polariton wavepacket. For simplicity and to emphasize its frequency domain nature, the transfer function will be written $T(\omega)$ and the dependence on n_i , k_i , and d will be implicit. In our implementation of phonon-polariton spectroscopy, the sample will have the only unknown pair of n and k . Values for n and k for the generation and detection crystals will be predetermined from separate experiments.

One advantage of phonon polariton spectroscopy is that a reference scan is not needed; instead, a polariton waveform is measured before and after interaction with a sample. Spectrometer parameters such as the distance between the probe arms are chosen so that the interacting polariton fields do not overlap in time. Data analysis begins by selecting the region of pulse 1 to create a data vector that represents the measured THz field at one of the probe arms, $E1(t)$, in the time domain. The edges of $E1(t)$ are set to decay exponentially to zero and the length of $E1(t)$ is zero padded for fast Fourier transform. Then a second independent data vector $E2(t)$ is created using the same procedure. In practice, most of the work presented in this section will be in the “broadband region” where a single cycle polariton wavepacket several picoseconds long will be excited, and these pulses are easily windowed. The time between when the polariton has its first probe interaction and its second probe interaction can range from 10ps to 250 ps, and is only limited by range of the probe delay stage and the losses to the polariton wavepacket during propagation. In practice data are often collected only in the temporal regions of the pulses, so data collection can be quite fast, typically on the order of 10 minutes. The data scans are typically conditioned by baseline subtraction and data smoothing in the time domain, with either a 5 or 10 point moving average depending on the resolution of the time step.

Let us examine the simplest case of propagation in a single medium as an example. In this case, as is well known, the transfer function relating the pulses is given by [76, 81],

$$T(\omega) = \exp \left[\frac{-i(n - i\kappa)\omega d}{c} \right], \quad (4.17)$$

and solving for $T(\omega)$ in terms of experimentally measured quantities gives,

$$\frac{E_2(\omega)}{E_1(\omega)} = T(\omega). \quad (4.18)$$

This relates our measurements to an analytic expression for n and κ . The transfer function must be inverted however, and in all but the simplest cases this cannot be done analytically without approximation. However since the calculation of $T(\omega)$ from n and κ is trivial, the problem lends itself to calculating the $T(\omega)$ for a range n and κ and comparing this to the experimental $T(\omega)$ with a minimization search [49, 82].

Equation 4.17 is suggestive, if we consider $T(\omega)$ in polar form and examine the log of the magnitude and the argument of T we see that,

$$\ln |T(\omega)| = \frac{-\kappa\omega d}{c} \quad (4.19)$$

$$\arg(T(\omega)) = \frac{n\omega d}{c} \quad (4.20)$$

Equations 4.19 and 4.20 are linear functions of κ and n respectively. Clearly equations 4.19 and 4.20 can be rearranged to give analytic expressions for n and k , but this form of these equations also motivates a parabolic error function, δ , of the form

$$\delta(n, \kappa) = \delta\rho^2 + \delta\varphi^2 \quad (4.21)$$

where

$$\delta\rho = \ln |T(\omega)| - \ln |T_{meas}(\omega)| \quad (4.22)$$

$$\delta\varphi = \arg(T(\omega)) - \arg(T_{meas}(\omega)) \quad (4.23)$$

where $T(\omega)$ is an analytic expression transfer function used in Eqs. 4.19 and 4.20 and $T_{meas}(\omega) = E_2(\omega)/E_1(\omega)$ is the experimentally measured transfer function. In this simple case the error function is parabolic with a well defined minimum at n and κ . For more complex transfer functions, such as those that include transmission and reflection coefficients or propagation in different media, the error function is still well

described by a parabola with a global minimum at n_{sample} and κ_{sample} .

The $\arg(T_{meas}(\omega))$ (i.e. the phase) requires further discussion. To convert the set of complex numbers that comprise $T_{meas}(\omega)$ from rectangular to polar coordinates the phase angle is constrained to lie between $-\pi$ and $+\pi$. The phase of the propagated polariton waveform is not constrained and has a physical meaning. It is the number of cycles the polariton field has oscillated during its propagation. To transform the experimental value of the phase to the physical quantity, the appropriate integer multiple of 2π for each point must be added. This multiple is chosen by unwrapping the phase of $T_{meas}(\omega)$ where the Fourier amplitudes of $E1(\omega)$ and $E2(\omega)$ are maximal. Unwrapping the data vector adds multiples of 2π to prevent adjacent points in the data vector from differing by more than 2π . If the refractive index of the material does not have a strong frequency dependence over the range of unwrapped frequencies, then the unwrapped phase is linear and defines a line. From equation 4.20, as $\omega \rightarrow 0$, it is clear that the phase also goes to zero. This is the final constraint: the unwrapped phase is shifted by a single multiple of 2π for all of the unwrapped points so that the y-intercept of the line is as close to zero as possible. The unwrapping procedure is then expanded, and the unwrapped points are shifted by a multiple of 2π to minimize the distance to the line.

Two further issues must be accounted for to obtain a quantitative data extraction. First, the amplitude of the time domain pulses must be scaled by a factor to account for the extent of the polariton that the probe pulse measures, this is the distance L in equations 4.7 and 4.8. Although the pump generates polaritons throughout the entire depth of the crystal, the polariton field at the back of the crystal is immediately reflected. The probe beam does not measure a constant phase slice of the reflected beam, and for this reason, the contribution of the integrated intensity of reflected polariton beam to the probe is negligible. The amount of polariton field reflected, and therefore invisible to the probe, depends on the length of propagation. Second, the distance the polariton waveform propagates must be determined. These two issues depend on the specific geometries of the spectrometer cell, and will be presented independently for each case. The Matlab programs used for data extraction are given

in Appendix A.

4.3.2 Single Crystal Spectrometer

The single crystal spectrometer apparatus provides the simplest case of data extraction because the polariton waveform is generated and detected in the same crystal. It is also the most important case because it is used to determine n and κ for the generation and detection crystals that are used in all of the other cases. Although the transfer function for propagation in a simple medium was presented in section 4.3.1, it is not sufficient in this case. This is because the distance the polariton waveform travels is a function of the forward angle and therefore implicitly a function n . The transfer function instead is given by,

$$T(\omega) = \exp \left[\frac{-i(n - \kappa)\omega d(n)}{c} \right] \quad (4.24)$$

where $d(n)$ emphasizes the distance dependence on n . It is possible to separate the phase and magnitude of $T(\omega)$ analytically, but it is simpler to solve it iteratively until the values of n and κ stop changing.

Figure 4-7 shows that the distance the polariton travels is given by,

$$d = \frac{\text{prpr}}{\cos(\theta_f)} \quad (4.25)$$

where prpr is the distance between the two probe arms. The scale factors shown in Figure 4-7 illustrate the amount of polariton field that the probe integrates over (i.e. the interaction length L) and can be described from simple geometry,

$$\text{Scale E1} = \text{txtal} - \text{pupr} * \tan(\theta_f) \quad (4.26)$$

$$\text{Scale E2} = \text{txtal} - (\text{prpr} + \text{pupr}) * \tan(\theta_f). \quad (4.27)$$

Each of the scaling factors should have an additional $\cos(\theta_f)$ factor to represent the true width of the polariton beam, but since only the ratio of the two scaled pulses

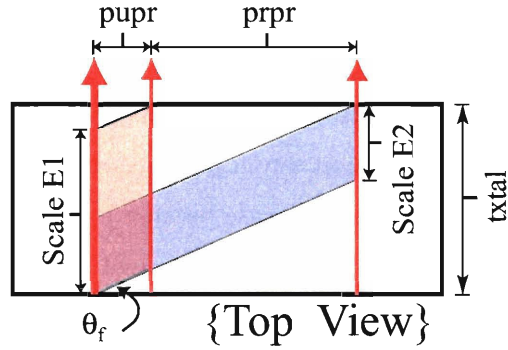


Figure 4-7: Top view of single crystal spectroscopy cell illustrating the portions of the generated polariton wavefront that probe 1 and probe 2 coherently integrate. Scale E1 and Scale E2 are used to normalize the measured polariton pulses. “pupr” is the distance between the pump and probe beams. “prpr” is the distance between the probe beams. “txtal” is the thickness of the crystal.

is used in the analysis this factor of often ignored. The distances used in the scale factors are measured by imaging the focal plane to a CCD camera. The image on the CCD is calibrated by translating the spectrometer apparatus a known distance with a micrometer stage. Although both n and κ are extracted from this analysis, at low temperatures the absorption in LiTaO_3 and LiNbO_3 is too small to be accurately resolved with this technique. This indicates that the absorption at low temperatures is too weak to have a significant influence on our measurements.

4.3.3 Reflection Spectrometer

In the reflection configuration, the generated polariton waveform reflects off the sample at an angle of incidence equal to the forward angle. It is therefore critical to know this angle well, and this requires knowledge of the refractive index of the generation crystal. The depth of the generation crystal is also chosen to be smaller than the sample, so that all of the generated polariton waveform reflects off of the sample. Although in principle, κ of the sample and generation crystal bath affect the phase of

the reflected light, this phase shift is significantly smaller than what can be measured with our spectrometer. Only the angle dependent index of refraction will be used in the reflection coefficient.

$$r_{\parallel}(\omega) = \frac{\cos \theta - \sqrt{\left(\frac{n}{n_s}\right)^2 - \sin^2 \theta}}{\cos \theta + \sqrt{\left(\frac{n}{n_s}\right)^2 - \sin^2 \theta}} \quad (4.28)$$

where n_s refers to the sample, and n refers to the generation crystal. In the reflec-

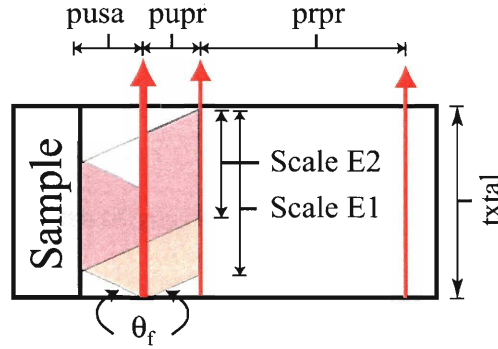


Figure 4-8: Top view of reflection spectroscopy cell illustrating the portions of the right and left generated polariton wavefronts that probe 1 coherently integrates. Scale E1 and Scale E2 are used to normalize measured polariton wavepackets.

tion case, the same polariton wavepacket is not measured in both cases. Figure 4-8 shows that instead, the right propagating polariton waveform is compared to the left propagating polariton waveform that reflects off the sample to determine $E1$ and $E2$. It should be stressed that these polariton wavepackets are equivalent for symmetric excitation pulse profiles and normal incidence. The relative distance that the two polariton wavepackets travel is given by the equation below,

$$d = \frac{(\text{pusu} + \text{pupr})}{\cos(\theta_f)}. \quad (4.29)$$

and the transfer function is given by,

$$T(\omega) = r_{\parallel}(\theta_f) \exp \left[\frac{-i(n - \nu\kappa)\omega d}{c} \right] \quad (4.30)$$

where n , κ refers to the generation (and detection) medium. The scale factors shown in Figure 4-7 are given by,

$$\text{Scale E1} = \text{txtal} - \text{pupr} * \tan(\theta_f) \quad (4.31)$$

$$\text{Scale E2} = \text{txtal} - (\text{pusa} + \text{pupr}) * \tan(\theta_f). \quad (4.32)$$

The right propagating polariton waveform is measured to obtain $E1$ but it also often measured at the second probe arm as well. In this manner, the single crystal measurement of the generation crystal can be combined with the reflection measurement and both can be done simultaneously.

4.3.4 Transmission Spectrometer with Cut Crystals

The transmission configuration is shown in Figure 4-9. The right propagating polariton waveform is generated by the pump beam and then measured at the first probe arm. At the sample interface, the polariton waveform is partially reflected and partially couples THz radiation into the sample. At the second interface the THz radiation is partially reflected and partially coupled into the detection crystal where a polariton wavepacket is regenerated. The angle of incidence is approximated as normal for both interfaces, although the forward component (hence the angle of incidence) changes with temperature. Two transmission coefficients are needed, one for each interface,

$$t_{\parallel}(\omega) = \frac{2n}{n + n_s} \quad (4.33)$$

$$t'_{\parallel}(\omega) = \frac{2n_s}{n + n_s}. \quad (4.34)$$

From Figure 4-9, the distance traveled in generation and detection crystals from the first probe to the second probe is given by,

$$d = \frac{\text{pupr}}{\cos(\theta_f)} - \text{tsam}. \quad (4.35)$$

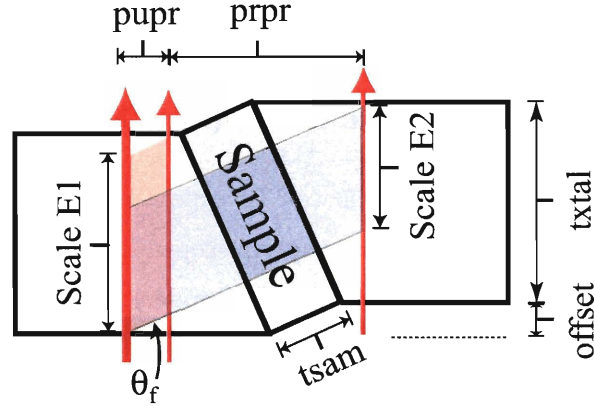


Figure 4-9: LiTaO₃ is cut at an angle of 20° and a clamp is used to hold the crystals together. Scale E1 and Scale E2 are used to normalize the measured polariton wavepacket signals.

The distances pupr, prpr in Figure 4-9 are measured by imaging the focal plane of the pump on the CCD. The thickness of the crystals and the sample are measured with calipers prior to the experiment. The transfer function for this experiment is,

$$T(\omega) = t_{\parallel} t'_{\parallel} \exp \left[\frac{-i(n - \kappa)\omega d}{c} \right] \exp \left[\frac{-i(n_s - \kappa_s)\omega \text{tsam}}{c} \right] \quad (4.36)$$

where n, κ refer to the generation/detection medium and n_s, κ_s refer to the sample.

The scale factors shown in Figure 4-9 are given by,

$$\text{Scale E1} = \text{txtal} - \text{pupr} * \tan(\theta_f) \quad (4.37)$$

$$\text{Scale E2} = \text{txtal} + \text{offset} - (\text{pupr} + \text{prpr}) * \tan(\theta_f). \quad (4.38)$$

Measurement of the crystal offset is performed in several ways: it is calculated from geometry, measured with a ruler, and it is measured as a delay in an autocorrelation

experiment. The first two methods have proved to be somewhat inaccurate, and the autocorrelation method has proved to be too impractical to be used routinely. In this experiment it is also difficult to obtain values for κ_s . Uncertainty in the offset measurement adds significant error to the scale factor for E2 and in general this prevents an accurate determination of κ_s . Suggestions for improved transmission measurements are offered subsequently.

4.3.5 Spectroscopy with Free Space THz Radiation

The data extraction for the free space THz experiments introduced in section 2.5 is similar in approach to our polariton spectroscopy. The first major difference is that two scans are needed, one in which sample is present and one in which it is absent to serve as a reference. One of the main advantages of free space THz spectroscopy is that there are no geometrical factors that add uncertainty to the data analysis, only the sample thickness is needed. The polariton peaks are selected from the two scans and windows in a manner identical to that of the polaritons. The transfer function for propagation in the sample and reflection at normal incidence for the two air-sample interfaces is give below,

$$T(\omega) = \exp \left[\frac{-i(n-1) - i\kappa\omega d}{c} \right]. \quad (4.39)$$

Equations 4.39 can be solved analytically for n and κ so no fitting procedure is required, although the phase of $T(\omega)$ must be unwrapped in the same manner discussed in Section 4.3.1.

4.4 Demonstration on LiTaO₃ and LiNbO₃

This section will present some illustrative examples of polariton spectroscopy. The polariton spectroscopy results on the relaxor ferroelectric KTN will be primarily saved for chapter 6 so that they can be discussed proper detail.

4.4.1 Temperature Dependence

The temperature dependence of LiTaO_3 and LiNbO_3 plays a crucial role in the polariton experiments, as it changes the forward angle by several degrees and this significantly affects the extraction of quantitative results. Figure 4-10 show the temperature dependence of LiTaO_3 and provides a good example of typical polariton spectroscopy data. The raw data shows much qualitative information. The area of the transmitted (right) peak provides information about absorption of the material and the time of flight gives an estimation of the refractive index. The peak area changes substantially as the temperature is decreased, and it visibly approaches the area of the generated peak at low temperatures. The shape of the polariton waveform also changes slightly but this is due more to the quality of the scans. Additionally, the phase of the peak is flipped by 180° as is expected from detection at the second probe arm. It should be emphasized that the area of the peak is only a qualitative measure of absorption and can be misleading, as the second probe arm measures a smaller polariton beam width, and therefore overestimates the amount of absorption. Variation in the time of flight is not as obvious in the raw data, although the polariton waveform clearly arrives earlier at lower temperatures. A faster polariton velocity (shorter time delay) results in a larger forward angle. This larger forward angle means that the polariton traveled a greater distance, and therefore the time delay underestimates the polariton group velocity and overestimates the index of refraction. The refractive index for two separate experimental trials on LiTaO_3 is shown in figure 4-11, and this level of agreement between values is typical.

Values for the extinction coefficient κ are much more difficult to determine because uncertainties in scaling factors cause errors on the order of the absorption. Although it is unfortunate that experiment has trouble measuring the small values of κ , the fact κ is small in these crystals makes them better suited for polariton spectroscopy. Nominally κ was determined to be ~ 0.01 in LiTaO_3 from 250 K to 300 K. This value was used in the reflection and transmission experiments, and for lower temperatures κ was approximated as zero, which is consistent with the literature [4, 44, 45].

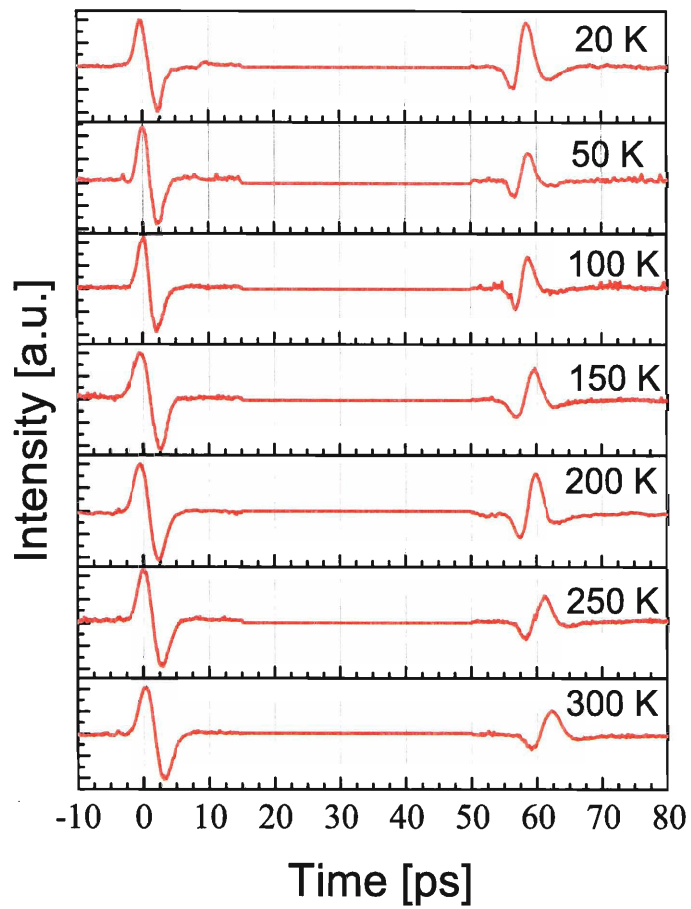


Figure 4-10: Polariton spectroscopy of LiTaO₃ as a function of temperature. See figure 4-2 for spectrometer geometry. The transmitted peaks (right) show a strong temperature dependent absorption. And while not as apparent in the raw data, the variation in time delay of the transmitted peak is also significant.

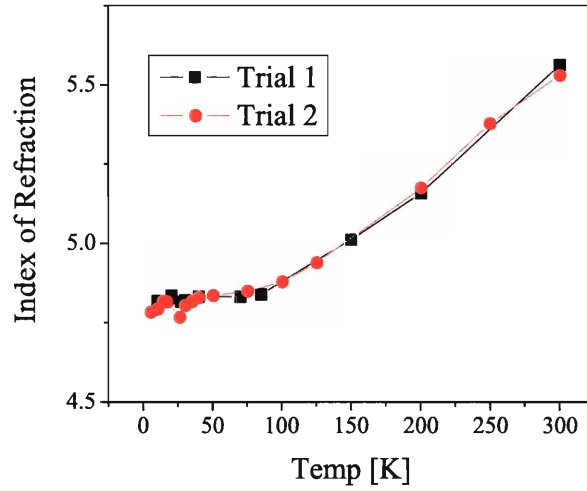


Figure 4-11: Temperature dependent refractive index for LiTaO_3 performed in two separate experimental trials. The value of the refractive index is independent of frequency in the measured range of 50-250 GHz.

4.4.2 Anisotropy

In our polariton spectroscopy experiments, the generated polaritons are polarized along the optic axis of the crystal. Figure 4-12 shows a transmission experiment with cut crystals where the sample is LiTaO_3 (LT), but with different orientations of the optic axis (out of the plane, and in the plan of the page) in the two cases. A line is drawn as an aid to the eye to show the polaritons delay through the ordinary axis of LiTaO_3 .

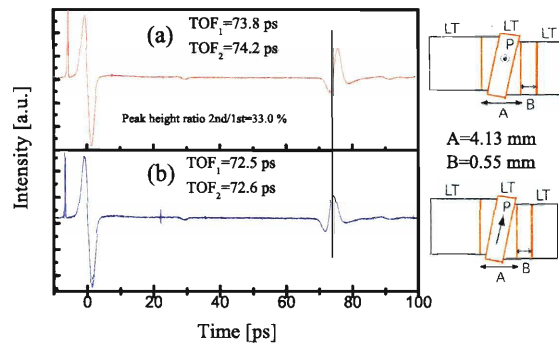


Figure 4-12: THz spectroscopy of different orientations of the optic axis of LiTaO₃. Plot (a) shows the polariton polarization parallel to the optic axis of the LiTaO₃ sample. Plot (b) shows the polariton polarization perpendicular to the optic axis of the LiTaO₃ sample. A slight increase in the time of flight is observed.

4.4.3 Horizontal Polarization of the Excitation and Probe

The lowest frequency A_1 symmetry mode in the ferroelectric crystals LiTaO_3 and LiNbO_3 (C_{3V} symmetry) is the dominant mode excited in polariton generation. The strongest polariton generation occurs when the excitation pulse is polarized parallel to the optic axis. For our cuts of crystals, in the lab frame this corresponds to a vertical polarization. It is also possible to excite the A_1 mode using an excitation pulse polarized perpendicular to the optic axis. Figure 4-13 shows polariton waveforms gen-

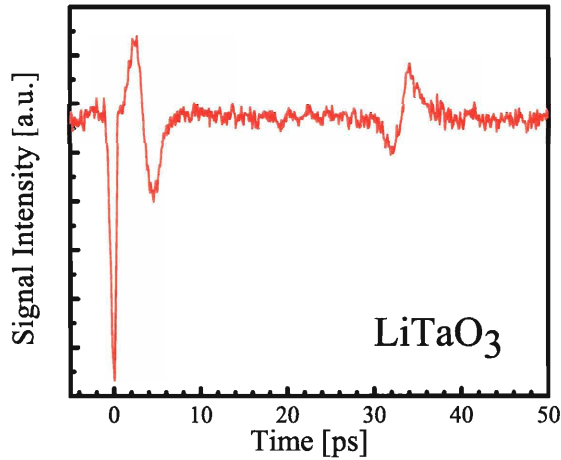


Figure 4-13: Measurement of a polariton pulse in LiTaO_3 with excitation and probe polarized parallel to the optic axis, (HH) in the lab frame. This generation and detection is much weaker than our normal (VV) excitation.

erated and measured with a horizontally polarized excitation pulse and probe pulse. The generated polariton waveform is substantially weaker because of the smaller Raman tensor component, and the phase shift in the probe beam is proportional to the smaller (factor ~ 3) electro-optic coefficient r_{13} discussed in section 3.3.3. This example verifies that our understanding of the generation and detection efficiencies in the excitation crystals, and demonstrates the feasibility of pumping and probing with different polarizations as a means separating scattered pump light from probe signal.

4.4.4 Polariton Coupling to Free Space

Although free space THz spectroscopy was described in the context of other generation materials, polaritons can be readily coupled into free space and used as a source of THz radiation. Figure 4-14 illustrates the polariton radiation being coupled to free space. The reflected pulse from the tilted edge is not visible because it is no longer propagating at the correct angle for the probe to see a constant phase of polariton waveform. The lower plot of the uncut crystal in contrast shows multiple reflections. THz radiation generated in this manner is less divergent than other sources, which

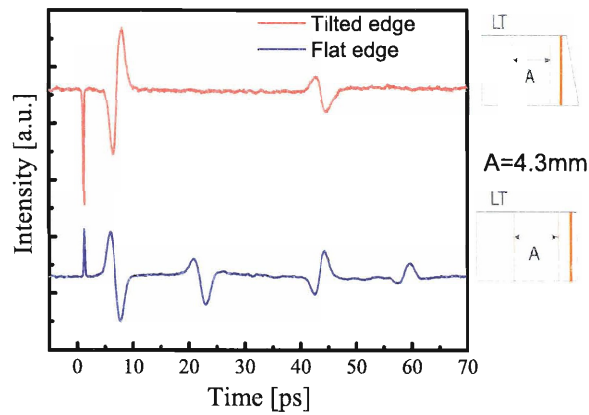


Figure 4-14: Demonstration of polariton coupling to free space. The cut crystal couples $\sim 53\%$ of its energy to free space THz radiation. The polariton waveform in the uncut crystal undergoes total internal reflection. The reflection is not seen in the cut crystal because the probe does not intersect the polariton waveform at the proper angle to see a constant phase slice.

are usually generated with a tightly focused beam. The use of polaritons as source of free space THz radiation connects the extensive polariton pulse shaping work to free space THz fields. Figure 4-15 demonstrates that a generated polariton can emit THz radiation at the crystal interface and that polariton can be recoupled into a second crystal for detection. The spacing of the two crystals is 1mm in the lower scan and 2 mm in the upper scan. An enlargement of the transmitted peak is shown, the single

cycle polariton is converted to a multicycle pulse sequence by etalon effects. The increased separation between the etalon pulses is clearly evident in the enlargement. To accommodate the increased spacing between two crystals the distance between the

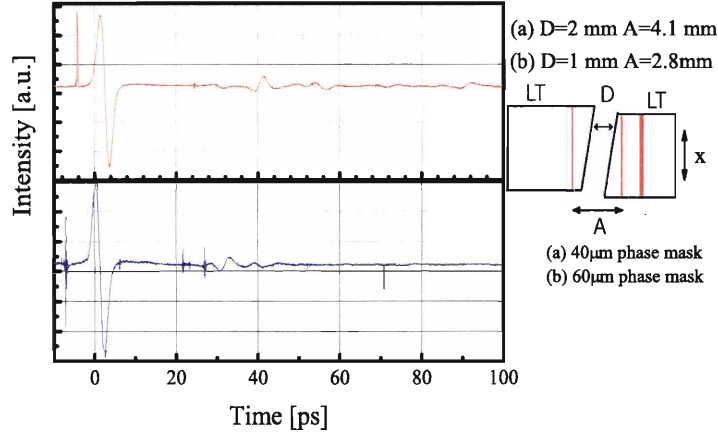


Figure 4-15: Top view: A polariton waveform generated in LiTaO_3 is used as a THz radiation emitter and recoupled into a second LiTaO_3 crystal where it is measured. The spacing, A , is 1 mm in the lower scan and 2 mm in the upper scan.

two probe arms was easily adjusted by changing the phase mask used in the grating interferometer. Note that the crystal positions are not optimized in the x direction so that the amplitude of the polaritons is not quantitative, i.e. not all of the polariton beam is necessarily entering the detection crystal.

4.5 Free Space THz Spectroscopy

A free space THz spectroscopy setup employing phonon-polariton generation methods, coupling to free space, and traditional detection methods is presented in section 2.5. Here we present a few results using free space THz spectroscopy as a comparison to polariton spectroscopy. Figure 4-16 shows the refractive index of $5\%\text{MgO}:\text{LiNbO}_3$ as a function of temperature. Several features stand out. First, the sensitivity of the technique captures the slight frequency dependence of the refractive index, and the spectral range is much larger than in the polariton measurements, covering ~ 0.2 - 1.2 THz. Figure 4-17 shows the extinction coefficient and the temperature trend that

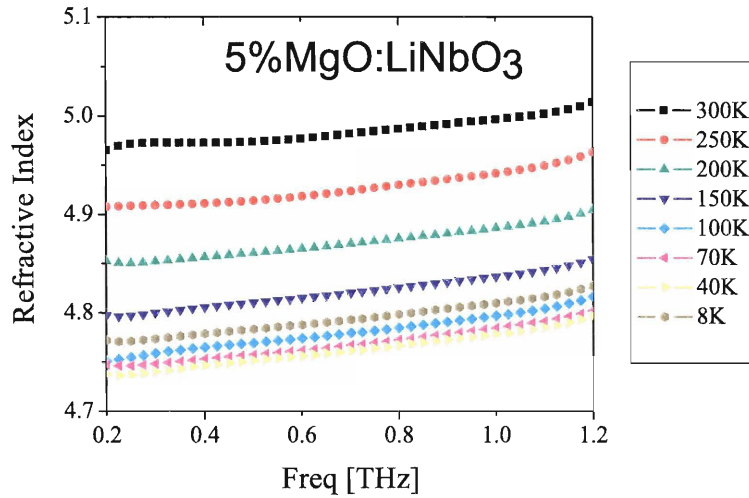


Figure 4-16: The refractive index of 5%MgO:LiNbO₃ measured with free space THz spectroscopy.

is generally expected. The strong temperature tails from 0.2 to ~ 0.4 THz and ~ 1.15 to 1.2 THz are not real, the spectral amplitude in these frequency ranges is too small for an accurate determination of κ . The spectral amplitudes of the data and reference pulses have oscillations from THz resonances of water vapor. These modulations are actually quite strong as the path length of the THz radiation is long, ~ 1.5 m, and the absorption due to water is significant. The modulations however are present in both the reference and data scans and are partially canceled when the ratio of the amplitudes is taken in the data extraction. This normalization is not perfect however, and it is a cause of bumps and oscillations in the free space spectra, which should be smooth monotonic curves. In particular the crossing of κ at 300 K and 250 K is the result of error in the experiment and is a good estimate of the uncertainty of the κ values.

Although the reference scan was also taken in the cryostat, it was performed at room temperature without purging of the atmosphere. The path length that the reference beam was exposed to water vapor where the data scan was not is the

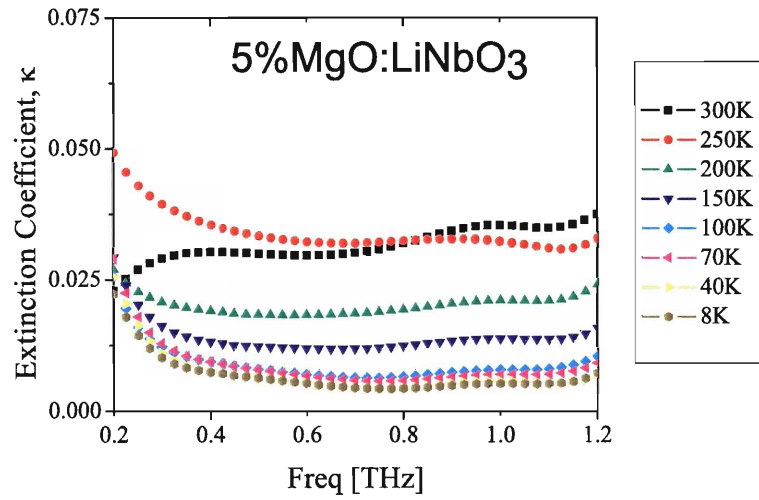


Figure 4-17: The extinction coefficient, κ , of 5%MgO:LiNbO₃ measured with free space THz spectroscopy.

length of the inner chamber of the cryostat, 2.8 inches. The relative exposure of the reference pulse to water from this small path length is enough to create distortions in the spectrum. These resonances are identified in Figure 4-18 and are labeled from the literature values [83]. This figure demonstrates potential sensitivity of the free space detection methods.

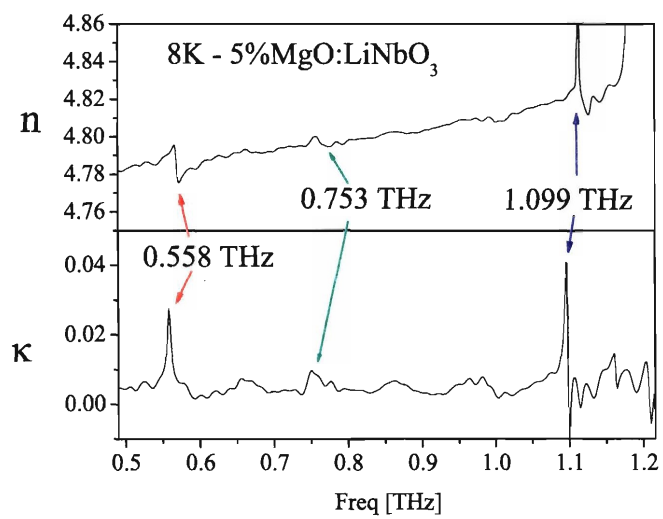


Figure 4-18: THz water resonances in measured with free space THz spectroscopy. The reference was taken in the cryostat with atmospheric water vapor present, while the low temperature measurement on 5%MgO:LiNbO₃ was dry. Assignments from Grischkowsky [83].

4.6 Comparison of Polariton based THz Spectroscopy to Free Space THz Spectroscopy

THz spectroscopy has been a field of active development. Free space techniques have been developed since the late 1980's and are now employed routinely by many groups. As Section 4.5 shows, the free space techniques based on ZnTe detection are also significantly more sensitive than the current polariton detection techniques. Of course, THz frequency phonon-polariton waveforms can also be coupled to free space and then measured by ZnTe. The sensitivity of the free space techniques enables the superior determination of κ , which is at present a more complicated measurement than with polariton spectroscopy. The bandwidth of the broadband free space techniques is larger than that of polariton based spectroscopy [1], even with tighter focusing of the polariton excitation pulse. This bandwidth can be extended to several THz by experimentally removing water vapor from the THz paths. Typically, for our polariton spectroscopy measurements the spectral range is between 50 and 250 GHz while for the free space experiments the spectral range is between 200 to 1100 GHz because of tighter focusing into the LiNbO₃ crystal.

Polariton spectroscopy has some unique advantages to the free space methods however. A major motivation for the development of polariton spectroscopy was to investigate high dielectric materials like the relaxor ferroelectric KTN. By generating the polariton in a dielectric material ($n \sim 5-6$), the dielectric contrast to the sample is significantly reduced. As will be discussed in chapter 6, the refractive index of KTN varies from 10 to 35 as the temperature is changed. Figure 4-19 compares our polariton transmission and reflection spectroscopies with our free space measurements.

There are a couple of points to highlight. First, to within the experimental error, the extracted values do agree. The values of refractive index for the polariton measurements have uncertainties from extraction, i.e. variation of the extracted value around the maximum of the Fourier amplitude, of typically ± 0.05 . In most cases, the uncertainty of extraction is not the most important source of error, and systematic error from the geometrical factors used in extracting the data give a more realistic

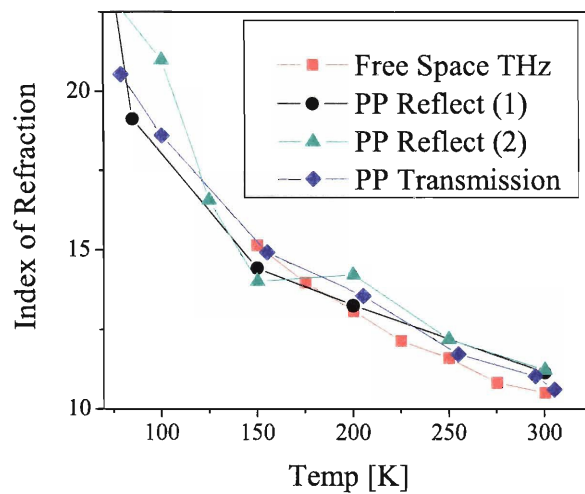


Figure 4-19: Comparison of PP polariton spectroscopy with free space methods in KTN. Polariton transmission spectroscopy is able to transmit more THz radiation through the KTN sample at lower temperatures where the dielectric constant begins to diverge. Free space measurement could not be continued below 150 K while polariton transmission measurements were performed at all temperatures down to 80 K. Polariton reflection measurements were performed down to 4 K. The results of measurements at lower temperatures are reported subsequently.

value for the uncertainty at 0.5 for the reflection and 1 for the transmission experiments. The second point is that polariton transmission spectroscopy transmits THz radiation through the sample at temperatures down to 80 K before the polariton signal was lost. In contrast free space THz spectroscopy could only be performed to 150 K before the transmitted pulse was too weak to detect. Reflection measurements that cover the entire temperature range down to 5 K will be presented in chapter 6.

These high values for the refractive index translate to high reflectivity at the LiTaO_3 –KTN interface and even higher reflectivity at the air–KTN interface. Figure 4-20 translates these refractive index values to corresponding values of the reflection coefficient, r_s , for free space THz radiation at normal and 45° incident angles and polaritons from LiTaO_3 .

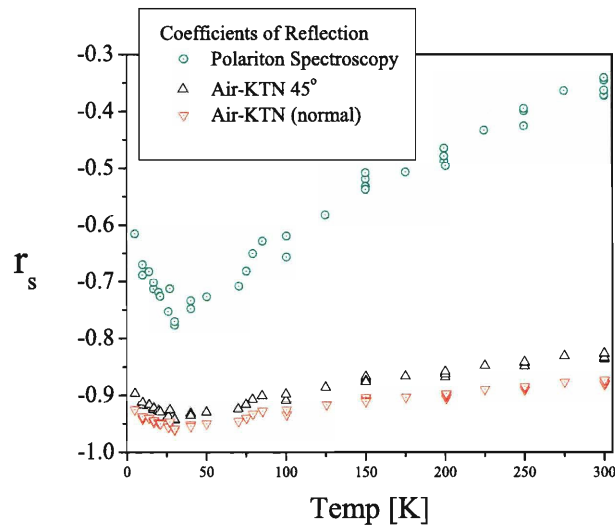


Figure 4-20: The reflection amplitude coefficients determined from our experimentally measured values of the refractive index for KTN utilizing polariton spectroscopy. The values were converted to equivalent values of what a free space reflection THz spectroscopy method would yield for air KTN interface at 45° and normal incidence.

The greater range of the reflection coefficients shows that the reflection measurements with polaritons are inherently more sensitive than free space measurements, although of course, the sensitivity of the of the detection matters too. The superior

sensitivity of the free space transmission measurements was demonstrated in section 4.5, but a free space reflection measurement has additional difficulties. In particular the reference scan is problematic. The reflection loss associated with a reference mirror must be accounted for and the reference and sample reflection must be independently aligned. In contrast, the reflection measurements in polariton spectroscopy are the easiest, since no crystal cutting is required, the dielectric constant of the generation and detection material can be measured at the same time, two not three crystals have to be mounted in contact, and the geometrical factors can be more accurately determined. For reflection from high-dielectric materials, polariton reflection spectroscopy offers clear advantages.

In addition to the generation and detection components, free space methods employ parabolic gold mirrors to collimate and focus the THz radiation. These mirrors are common, commercially available, and reasonably easy to align. They offer the experimental advantage of significantly more control in aligning beams and adjusting beam size. These tasks are much more challenging when applied to polaritons. Many research groups have contributed to free space techniques such that there exists a well established body of methodology that is robust. In contrast, manipulating polaritons in a crystal is more difficult, but the avoidance of THz optics offers some potential benefits, especially from an industrial perspective. First, an integrated polariton platform machined for specific applications would have fewer parts, potentially less need for alignment, and can be significantly more compact. Our current spectrometers are on the order of 5x2x2mm and can easily fit inside a typical cryostat. To a certain extent, using parabolic gold mirrors to focus the THz radiation will always preclude miniaturization, and a 20x20cm footprint for focusing elements of a free space THz spectrometer would be considered compact.

4.7 Multicycle Phonon-Polariton Waveform Generation

Section 4.1 introduced optical pulse shaping as a method of creating polariton waveforms. This section presents two simple forms of pulse shaping for generation of multicycle “narrowband” polariton waveforms with well defined frequencies and wavevectors. This contrasts with the single cycle polariton pulses that have been discussed previously.

4.7.1 Deathstar Temporal Pulse Shaping

The “Deathstar” introduced in Section 2.6 converts an optical pulse into sequence of 7 uniformly temporally spaced pulses with a gaussian intensity envelope. Figure 4-21 shows the use of deathstar, introduced in section 2.6, to generate a multicycle waveform with a 400 GHz frequency.

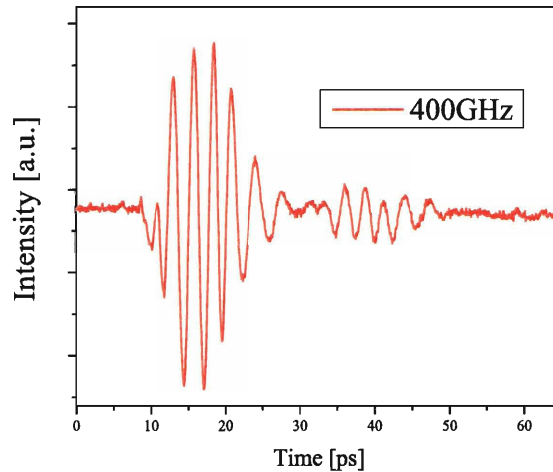


Figure 4-21: An optical temporal only pulse shaper was used to generate a 7 cycle pulse train to excite a 400 GHz polariton excitation that was detected with the standard dual arm interferometer. The rapid decay of the waveform from one probe arm to the second is an artifact of the excitation and detection used.

The polariton waveform is detected with grating interferometer. The waveform appears to rapidly damp, but this is an artifact of the experimental limitations of laser power. The Deathstar pulse shaping cavity is lossy, and since the ISRS generation process is third order, the electric field amplitude of each of the pulses of the optical pulse sequence is substantially smaller than in the broadband measurements. As a consequence, the seven cycle pulse train could not be focused to a tall line. The focus in the vertical dimension was similar to the focus of the width, and polariton waveform radiated conically away from the pump region. This led to lower signal at the second probe arm. Nevertheless, this experiment shows that temporal only pulse shaping can generate multicycle polariton waveforms. Under appropriate conditions (more energy per pulse) reliable narrowband polarization spectroscopy measurements could be conducted.

4.7.2 Transient Grating Phonon-Polariton Excitation

A more common method of pulse shaping is to image binary phase masks into the generation crystals, in a similar manner to the transient grating experiments to be discussed in Section 2.4. Unlike all of the other polariton measurements discussed in this section, diffraction from the multicycle polariton waveform was used instead of interferometry. A fourth beam was also used as a local oscillator for heterodyned detection.

Figure 4-22 shows a polariton waveform with a 1 THz frequency. The first probe measurement is with the probe completely overlapped with the pump. Because of this the polariton response suddenly appears at time zero. The signal is maximum because of complete overlap, then the envelope of the detected signal slowly decays as the polariton waveform propagates out of the probe region. The second probe shows the polariton waveform propagating into and out of the probe region, revealing a gaussian envelope. This and other measurements indicate that narrowband polariton spectroscopy can also be conducted in this manner.

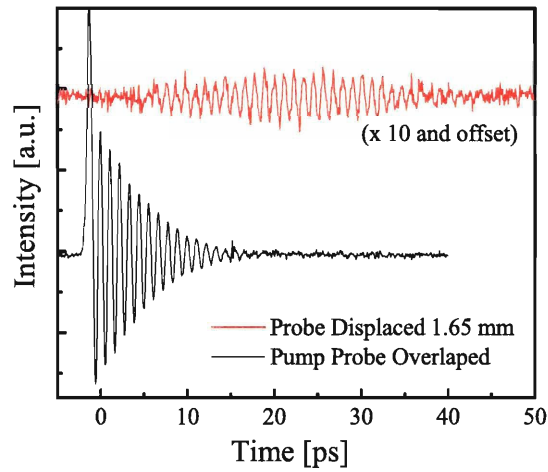


Figure 4-22: A grating is imaged into a LiNbO_3 crystal exciting a narrow band polariton waveform with a 1 THz frequency. The black plot shows the probe overlapped with the excitation pulse and the polariton propagating away from the probing region. The red plot shows polariton propagating into and out of the second probe region. The modulation amplitude of the black plot is much larger because it is measuring both the right and left propagating polariton field and measuring the polariton throughout the entire depth of the crystal.

4.8 Conclusions and Future Directions

Three configurations of compact THz spectrometers based on grating interferometric detection of phonon polariton waveforms have been demonstrated. The method for data extraction for each of the configurations was presented and several important examples of polariton spectroscopy were shown. For comparison, some free space THz spectroscopy was introduced and compared to polariton spectroscopy of the relaxor ferroelectric KTN and the relative advantages and disadvantages of polariton spectroscopy under different conditions were highlighted. The utility of polariton spectroscopy for high-dielectric samples is clear.

The most promising avenue of polariton spectroscopy is the reflection configuration. Although the grating interferometer is useful, the dual probe arms are unneeded in the reflection measurement. A single probe arm based on birefringence and dual detection similar to the free space techniques could dramatically improve the sensitivity of the polariton detection. There are several reasons to be optimistic about this approach. First, difference detection is sensitive and noise from power fluctuations in the laser is eliminated. Secondly, it removes the need for dual frequency chopping, which is necessary for the interferometric measurements but limits the amount of signal that reaches the detector. One issue that was not fully addressed was the experimental difficulty of separating scattered pump light from the dual arm interferometer. Polariton detection requires the pump and probe beams to enter the generation crystal at normal incidence. This means that the second lens of the interferometer focuses the pump beam onto the diffraction grating where it diffracts/scatters light collinearly with the interferometrically recombined probe beams. The pump can be spatially blocked before the second lens, but with the cryostat in the experimental set-up it was not always possible to fully block the pump beam. Dual frequency chopping was used to successfully suppress the stray pump light, but dual frequency chopping also limits laser pulses that contribute to the signal.

Another important direction are efforts to design cell geometries that minimize the impact of the forward component of polariton waveform propagation. One simple

approach is to cut a crystal so that the optical excitation beam enter cut portion of the crystal at normal incidence but at an angle relative to the front face of the crystal. For the proper choice of angle, the excitation beam will generate a polariton waveform that propagates parallel to the front crystal face. Eliminating the forward component simplifies the transmission experiment by reducing the uncertainties of the geometrical factors. This will improve the determination of n but will be particularly helpful in extracting κ .

Polariton spectroscopy also offers potential as a platform for compact, integrated THz spectroscopy. The pulse shaping methods show much promise for generating intense polaritons for non-linear polariton or THz spectroscopies. Laser machining can also be used to make integrated sample holders, particularly for liquids and glass forming liquids [84] where sample cells are fabrication are complicated by the need to make multiple path lengths. Interfacing of a polariton-based THz spectrometer to microfluidic systems also would be possible.

Chapter 5

Introduction to Ferroelectrics

This chapter will provide a brief overview of ferroelectric crystals, and also motivate their study by showing their broad range of properties and technical applications. Section 5.1 will provide a brief background and introduction to ferroelectrics as well as introduce some basic terminology. Next, section 5.2 will present some selected applications of ferroelectrics to demonstrate their technological importance. The third section, 5.3, will introduce the concepts of the ferroelectric transition, with an emphasis on features that differ between traditional ferroelectrics and relaxors. Finally, section 5.4 will include a discussion of relaxor ferroelectrics providing the background necessary to understand the spectroscopic studies of the relaxor ferroelectric $\text{KTa}_{0.982}\text{Nb}_{0.018}\text{O}_3$ (KTN 1.8) presented in chapter 6.

5.1 Ferroelectrics: Background and Terminology

A ferroelectric material has a spontaneous dipole moment that can be reversed by the application of an applied electric field. In a microscopic sense, this means that the microscopic structure has two or more states of equivalent energy that have associated permanent dipole moments in different orientations. The application of a sufficiently strong external field with the proper polarization will change the direction of the spontaneous dipole movement by converting the material from one state to another. Another important characteristic of a ferroelectric is a transition temperature, the

Curie temperature T_c , above which the material is paraelectric and does not have a spontaneous macroscopic polarization.

In a practical sense ferroelectrics are of theoretical and technical interest because they often have unusually high and unusually temperature dependent values for the dielectric constant, exhibit strong piezoelectric and electrostrictive effects, strong pyroelectric effects, and have useful electro-optical and nonlinear optical properties, in particular optical frequency doubling. In a more fundamental physical sense, they are interesting because all of these unusual, and technologically useful, properties arise from the delicate balance of two strong and opposing forces, long-range Coulomb forces (which favor the ferroelectric state) and short-range repulsions (which favor the non-polar phase). This balancing leads to the strong sensitivity of ferroelectrics to the details of chemistry, defects, electrical boundary conditions, pressure, and temperature. Differences in hybridization and covalency of the chemical bonds has also been shown to play an important role in ferroelectricity [85]. The sensitivity of ferroelectrics to these many factors has contributed to the difficulty in development of a first principles theoretical understanding of ferroelectrics. Much progress has been made on traditional ferroelectrics however, by applying modern first principle band structure calculations and through advances in density functional theory (DFT) calculations [86]. Now theoretical efforts are turning increasingly to more complicated ferroelectric materials [87], of which relaxors, defined below, are perhaps the most important.

To begin our discussion of ferroelectrics, we define some useful terminology. One of the most important properties of a ferroelectric is its large macroscopic polarization and associated dielectric constant; these two quantities are related by [41],

$$\varepsilon = \frac{\epsilon_0 E + P}{\epsilon_0 E} = 1 + \chi_e. \quad (5.1)$$

In an isotropic or cubic medium Equation 5.1 reduces to a scalar equation, which is sufficient for our purposes since at all times we will only be concerned with single tensor components. ϵ_0 is the permittivity of free space, E is the macroscopic polarization,

P is the dipole moment per unit volume, and χ_e is the dielectric susceptibility. By convention $\chi_{SI} = 4\pi\chi_{CGS}$, but $\epsilon_{SI} = \epsilon_{CGS}$.

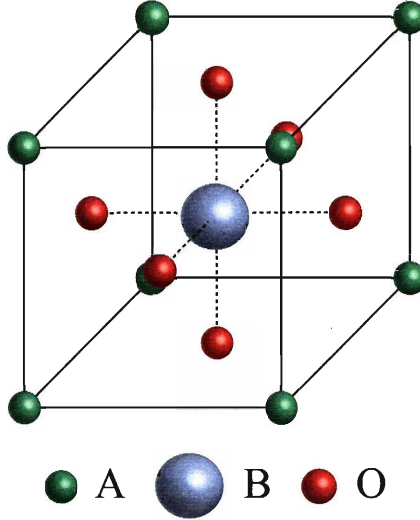


Figure 5-1: Structure of an ABO_3 perovskite in the cubic paraelectric phase. The A cations site is on the corners of the cube, the B cation is situated at the center, and Oxygen on the face centers.

An important class of ferroelectrics are ABO_3 perovskites whose simple chemical and crystallographic structures have contributed significantly to the understanding of ferroelectric and antiferroelectric phenomena since the discovery of $BaTiO_3$ by Wul and Goldman in 1946 [88]. This thesis will focus on the ABO_3 perovskites, for both conventional ferroelectrics and for relaxors. Two examples of ABO_3 ferroelectrics of special interest are $LiTaO_3$ and $LiNbO_3$, which serve as transducers in our implementation of phonon-polaritons spectroscopy, but these materials have a somewhat more complicated crystal structure. Mixtures of different ABO_3 perovskites can have dramatically different properties from either pure material, and some mixtures can display relaxor behavior. Our KTN sample is based on two perovskite structures, $KTaO_3$ which does not have a ferroelectric phase transition and $KNbO_3$ which is a typical soft mode ferroelectric. From soft mode theory $KTaO_3$ is expected to have a ferroelectric transition around several Kelvin, but quantum fluctuations intervene to frustrate this ferroelectric phase and $KTaO_3$ is often referred to as an incipient

ferroelectric or a quantum paraelectric. The sensitivity of ferroelectrics to chemical composition is shown in Table 5.1, which shows the Curie temperatures for our four ferroelectrics discussed so far.

material	LiTaO ₃	LiNbO ₃	KTaO ₃	KNbO ₃
T _c [K]	938	1483	-	708

Table 5.1: Values of the ferroelectric transition temperature T_c [88] for four chemical analog ABO₃ ferroelectrics that are of particular interest in this thesis. KTaO₃ and KNbO₃ are simple cubic perovskites in the paraelectric state while LiTaO₃ and LiNbO₃ have a more complicated structures. Note that changes in chemical compositions can cause substantial changes in ferroelectric behavior. KTaO₃ is an incipient ferroelectric which low temperature ferroelectric transition is frustrated by quantum fluctuations.

As the temperature of a ferroelectric is decreased below a transition temperature, T_c, the spontaneous polarization increases in magnitude, usually following a mean-field power law temperature dependence $P \propto (T_c - T)^{1/2}$, and the coercive field needed to change the polarization moment of the ferroelectric increases correspondingly. If electrical breakdown occurs from the applied field before the macroscopic polarization of the crystal changes, then the ferroelectric crystal is said to be pyroelectric. Even before the pyroelectric state is reached, ferroelectrics often also have sizeable pyroelectric coefficients, which relate the macroscopic polarization of the crystal to temperature.

When a crystal is in the ferroelectric state, it is also necessarily piezoelectric. The piezoelectric effect relates mechanical stress to an electric field.

$$P = Zd + \epsilon_0 E \quad \text{and} \quad e = Zs + Ed \tag{5.2}$$

where P is the polarization, Z is elastic stress, d is the piezoelectric strain constant, E is the electric field, χ is the dielectric susceptibility, e is the elastic strain and, s is the elastic compliance constant,

$$d_{ik} = \left(\frac{\partial e_k}{\partial E_i} \right)_Z \tag{5.3}$$

The piezoelectric strain constants are a third rank tensor, given in contracted notation where $i \equiv x, y, z$ and $k \equiv xx, yy, zz, yx, zy, xy$. So if an electric field is applied to a piezoelectric it will become strained, and similarly if the piezoelectric is stressed it will undergo a change in polarization. Only non-centrosymmetric materials will display the piezoelectric effect, as it is first order in the electric field. All materials will display the electrostrictive effect however, which is the second order coupling of strain to an electric field. Ferroelectrics, and relaxors in particular, also have large electrostrictive responses. Ferroelectric crystals are a subset of piezoelectric crystals, which are a subset of piezoelectric crystals.

Ferroelectric displacements are not the only type of structural rearrangements that can take place in a dielectric material. An antiferroelectric deformation occurs when neighboring lines of ions pair up and the unit cell of the crystal doubles. Several types of structural deformations are illustrated in figure 5.1. The ABO_3 perovskite structures will often display all of these deformations with little energy difference between them. The above discussion has focused on properties of the bulk crystal, however it should be acknowledged that domain size effects, interfaces, and thin films, all play important roles in ferroelectric applications and current research.

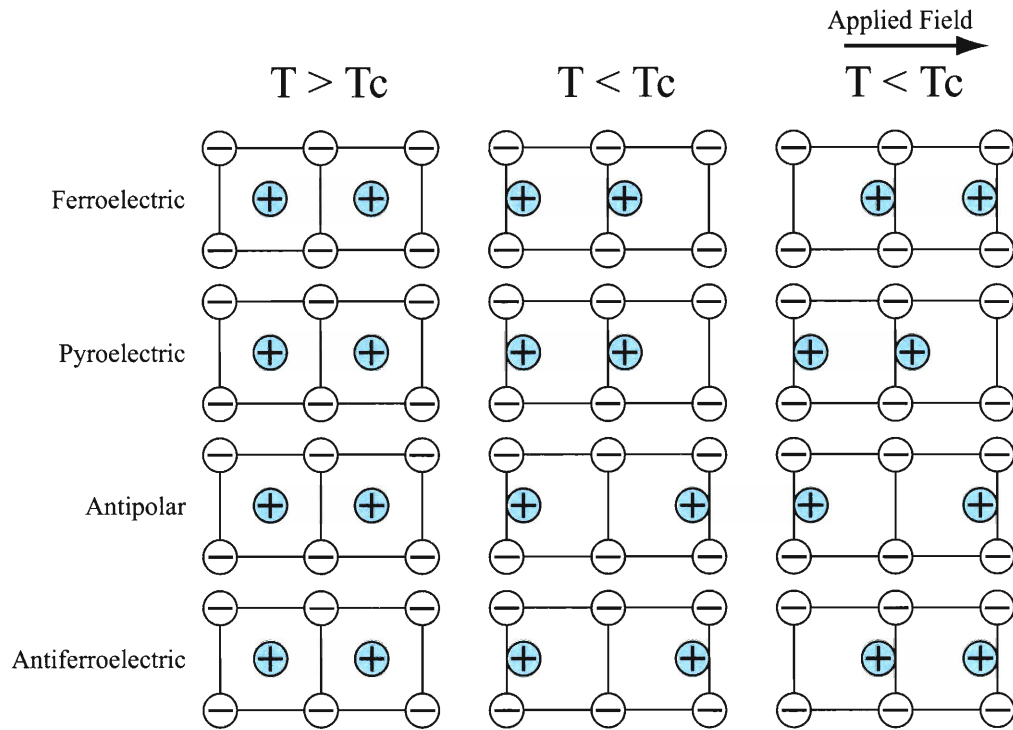


Figure 5-2: Schematic representation of a pair of unit cells undergoing several fundamental types of structural phase transitions from a centrosymmetric prototype. Adapted from Lines and Glass [88].

5.2 Applications of Ferroelectrics

Ferroelectrics are an immensely important class of materials. This section will motivate interest in ferroelectrics, and relaxors in particular, by briefly outlining some applications for each type of distinctive ferroelectric material property: dielectric constant, piezoelectric, pyroelectric, and electro-optic properties [89,90].

Ferroelectrics serve in a wide range of dielectric applications as capacitors. Not only do they have extremely large dielectric constants (10^4 - 10^5 is common), but that response is often uniform (non dispersive) over a wide frequency range. Capacitance is nominally proportional to the dielectric constant, and ferroelectric capacitors are especially important in multilayer thin films, which are used in, among other applications, computer memory. Although they are mostly used for their capacitive properties (DRAM), some types of computer memory exploit ferroelectrics directly

for memory storage. For example, Fujitsu has commercially produced ferroelectric random access memory (FeRAM or FRAM) based on the relaxor lead zirconate titanate PZT since 1998. The dominant non-volatile writeable erasable memory form is FLASH, a MOSFET based technology [91] but, in its current form, FRAM offers significant advantages to it. FRAM has faster write times ($\times 100$) and read-write cycle endurance ($\times 1000$) [92] although it has a significant disadvantage in expense [91]. This disadvantage is not inherent however, as FLASH is inherently a complicated many layer structure, this limits expected costs savings and storage densities, FRAM has fewer structural layers and could therefore be potentially mass produced at lower cost with higher storage densities. FRAM is currently used in a variety of applications ranging from RFID, automotive telematics and air bags, remote digital metering systems, office equipment such as copiers and printers, and televisions [92]. Several radiation hardened FRAMs have been developed for specific space missions [92].

Piezoelectric and electrostrictive responses in poled and unpoled ferroelectric and relaxor ferroelectric compositions are of importance in transducers for interconverting electrical and mechanical responses. For actuation the strong electrostrictive coupling of relaxors can be exploited for very high precision position control, and is often preferred because having little or no spontaneous polarization causes electrostrictors to have little or no hysteretic loss even at high frequencies (100 KHz) of operation. Although as a second order effect the electrostrictive response is quite small (10^{-5} to 10^{-7} % strain) in most materials [89], relaxors such as lead magnesium niobate - lead titanate (PMN-PT) can show strains (10^{-1} % strain) comparable to those based on piezoelectric effect and are found in many commercial systems [93]. Ferroelectric crystals are also used widely in SONAR hydrophone applications, and have been since World War II.

Pyroelectric systems rely upon the strong temperature sensitivity of the electric polarization for bolometric detection of long wavelength infra-red radiation. Simple point detectors are widely used in domestic and industrial applications. There is also a strong demand for pyroelectric imaging systems for use in night vision and thermal-medical diagnostics [89].

Electro-optic applications are also common because of high quadratic and linear electro-optic coefficients that occur in ferroelectrics. LiTaO_3 and LiNbO_3 are used heavily in the telecommunications industry for frequency doubling, in acoustic wave modulators, switches, guided wave structures and photo refractive devices [89]. This has a special consequence for our phonon-polariton spectroscopy as this demand has created a supply of high quality crystal manufactures and suppliers.

5.3 Basic Concepts

This section introduces the basic concepts and terminology of the ferroelectric transition and is guided heavily by an introduction to ferroelectrics by Kittel [41] and one of the canonical works on ferroelectrics by Lines and Glass [88].

5.3.1 Classification of Ferroelectric Crystals

The ferroelectric transition can be thought of in terms of two limiting cases: displacive and order-disorder. To illustrate these two cases in terms of our perovskite structure, consider KNbO_3 as an example. In the paraelectric phase it has eight equivalent sites in the $[111]$ directions. The Nb cation moves between these sites with an average position at the center of the crystal. In a displacive picture, this is as an oscillation around a non-polar site. At the ferroelectric transition the center of this oscillation moves to a polar site offset from the center of the crystal. In the order-disorder picture, the Nb cation is moving between eight equivalent potential wells in an activated process, and after the ferroelectric transition motion is limited to an ordered subset of these wells. In the case of KNbO_3 and often other perovskites there are actually three transitions, as the Nb is restricted from 8 sites (cubic) to 4 (tetragonal) to 2 (orthorhombic) to 1 (rhombohedral) as illustrated in figure 5.3.1. It has been established by Dougherty et. al. [16] that KNbO_3 has predominately displacive character.

It is common to consider the character of the ferroelectric transition in terms of its lowest frequency optical phonon mode [94], which is necessarily the transverse optic (TO) mode. The Nb motion dominates this low frequency TO phonon mode and is

used in our discussion as a proxy for the soft mode. This mode is called “soft” because its frequency decreases dramatically as each of the three ferroelectric transitions are approached. In a displacive transition, the the Nb motion is part of a true a phonon mode, implying that there is vibrational dynamics. In the order-disorder picture the soft mode near the transition becomes diffusive, and is it not a true phonon mode but is a large amplitude correlated hopping motion between the wells of the order disorder system. Many ferroelectrics have soft modes that fall within these extremes.

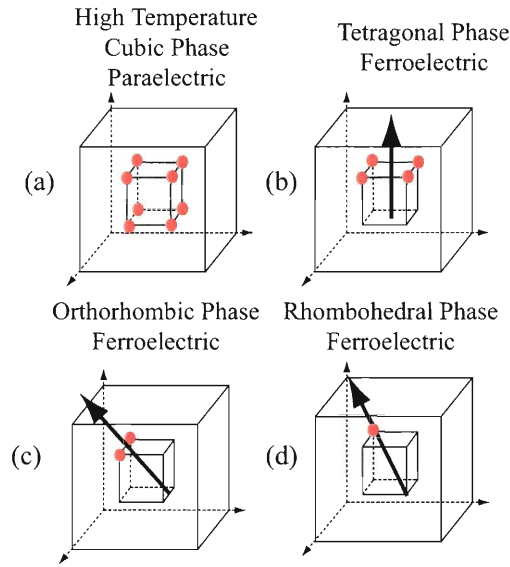


Figure 5-3: Schematic illustration of B cation occupation sites within the framework of the eight site model for an ABO_3 perovskite. Adapted from Dougherty [17].

Another fundamental concept is the thermodynamic order of the transition under the phenomenological Devonshire-Landau description of the ferroelectric transition. A first order phase transition is defined by a discontinuous change of the saturation polarization at the transition temperature. In contrast, the polarization of the second order transition goes continuously to zero at the transition temperature.

5.3.2 Curie-Weiss Law

In the soft-mode description of structural phase transitions, at each phase transition, the frequency of the soft mode decreases as the transition temperature is approached

from above or below. In a mean field picture, the soft mode has the following temperature dependence [95],

$$\omega_{soft}^2 \propto (T - T_c) \quad (5.4)$$

where T_c is the curie temperature for a second order transition. From the Lyddane-Sachs-Teller relation [41] for one optic mode;

$$\frac{\omega_T^2}{\omega_L^2} = \frac{\varepsilon(\infty)}{\varepsilon(0)}. \quad (5.5)$$

The high frequency dielectric constant, $\varepsilon(\infty)$, and ω_{LO} are approximately temperature independent, which suggests that the low frequency dielectric constant $\varepsilon(0)$ extrapolates to a singularity. This is the Curie-Weiss Law,

$$\frac{1}{\varepsilon(0)} = \frac{C}{T - T_c} \quad (5.6)$$

where C is the Curie Constant and T_c is the curie temperature. Physically the divergence can be expected and understood from the idea that as the soft mode frequency goes to zero, the crystal becomes unstable and an small applied field can cause a enormous change in the polarization of the crystal. Equation 5.1 shows that this situation implies a large dielectric constant. Relaxors have large dielectric constants, but do not show Curie-Weiss behavior near their dielectric maxima.

5.4 Relaxor Ferroelectrics

Relaxor ferroelectric behavior is characterized by a broad frequency dependent peak in the real part of the temperature dependant dielectric constant. Relaxor ferroelectrics are perhaps the most important class of ferroelectrics, for example La doped $\text{Pb}(\text{Zr}_{1-x}\text{Ti}_x)\text{O}_3$ (PLZT), $\text{Pb}(\text{Zn}_{1/3}\text{Nb}_{2/3})\text{O}_3$ - PbTiO_3 (PZN-PT) and $\text{Pb}(\text{Mg}_{1/3}\text{Nb}_{2/3})\text{O}_3$ - PbTiO_3 (PMN-PT) are some of the most common high performance actuators [93] and as previously mentioned PLZT is used in both conventional DRAM and FRAM applications.

Relaxor behavior in ferroelectric materials has been observed and studied most extensively in disordered ABO_3 perovskites and has been an important topic of current research. This discussion follows a review by Samara [7] on the relaxation properties of compositionally disordered ABO_3 perovskites. Random lattice disorder produced by chemical substitution in ABO_3 perovskites can lead to the formation of dipolar impurities and defects that have a profound influence on the static and dynamic properties of these materials that are prototypical soft ferroelectric mode systems. In these highly polarizable host lattices, dipolar entities form polar nanoregions (PNRs) whose size and orientations fluctuate dynamically with the average size given by the dipolar correlation length, r_c . These PNR's exhibit dielectric relaxation in an applied AC electric field. This is precisely the condition in our KTN sample, where KTaO_3 serves as the highly polarizable host, and Nb acts as the dipolar impurity. In the very dilute limit ($<0.1\%$ Nb in the case of KTN) each domain behaves as a non-interacting dipolar entity with a single relaxation time. At higher concentrations of disorder, however, the domains can interact leading to more complex relaxational behavior. This behavior is observed in our KTN sample for low frequency dielectric spectroscopy (<10 MHz). Among the manifestations of such behavior is the formation of a glass-like relaxor state, or even an ordered FE state for a sufficiently high concentration of impurities.

Figure 5.4 summarizes the main differences between conventional ferroelectrics and relaxors. The polarization (P) versus applied field (E) hysteresis loop (Figure 5.4a) is the signature of the low temperature ferroelectric phase. The large remnant polarization, P_R , is a manifestation of the cooperative nature of the ferroelectric phenomenon. In contrast, the relaxor exhibits a so-called slim loop, with only a small P_R value. For sufficiently high electric fields the PNRs of the relaxor can be oriented with the field leading to large polarization; however, on removing the field most of these domains re-acquire their random orientations resulting in a small P_R . The small, but non-zero P_R is evidence for the presence of some degree of cooperative freezing of dipolar (or PNR) orientations.

The next major difference is that both the saturation and remnant polarizations

of a ferroelectric decrease as the temperature is increased towards the ferroelectric transition, and vanish at a distinct temperature (T_c). The vanishing of saturation polarization (P_S) and remnant polarization (P_R) at T_c is continuous for a second-order phase transition (Figure 5.4 (b)) and discontinuous for a first-order transition. In traditional ferroelectrics no polar domains exist above T_c . In contrast, the field-induced polarization of a relaxor decreases smoothly through the dynamic transition (or relaxational condition, $\omega\tau = 1$, where ω is the ac field frequency and τ is a relaxation time) temperature T_f (as defined roughly from dielectric spectra) and retains finite values to rather high temperatures due to the fact that nano-size polar domains persist to well above T_f , as demonstrated through Raman, x-ray and neutron scattering experiments [96–99]. These PNR play a critical role in the behavior of relaxors, and their formation will be discussed in detail for our KTN 1.8 system in Chapter 6. The temperature at which the PNRs begin to form is the Burns temperature, T_B .

The third major difference, the one that was first discovered experimentally and often categorizes a material as a relaxor, is the behavior of the dielectric response. In a ferroelectric, the real part of the dielectric constant, ϵ' , exhibits a sharp, narrow peak at T_c (Figure 5.4(c)). For a single crystal the peak is very sharp and the width at half max is 1020 K. The FE response is frequency independent to several hundred KHz. By contrast a relaxor exhibits a very broad $\epsilon'(T)$ peak and strong frequency dispersion in the temperature of the peak maximum, T_f and in the magnitude of ϵ' below T_f . The temperature dependence of ϵ' of a ferroelectric obeys a Curie-Weiss law, $\epsilon' = C/(T - T_0)$, above T_c as shown by the linear $1/\epsilon'$ versus T response in Figure 5.4(c). By contrast $\epsilon'(T)$ of a relaxor exhibits strong deviation from this law for temperatures up to the Burns temperature and the disappearance of the polar nanodomains. It is only at high temperatures that a linear $1/\epsilon'$ versus T response is obtained.

Normal Ferroelectric

Relaxors

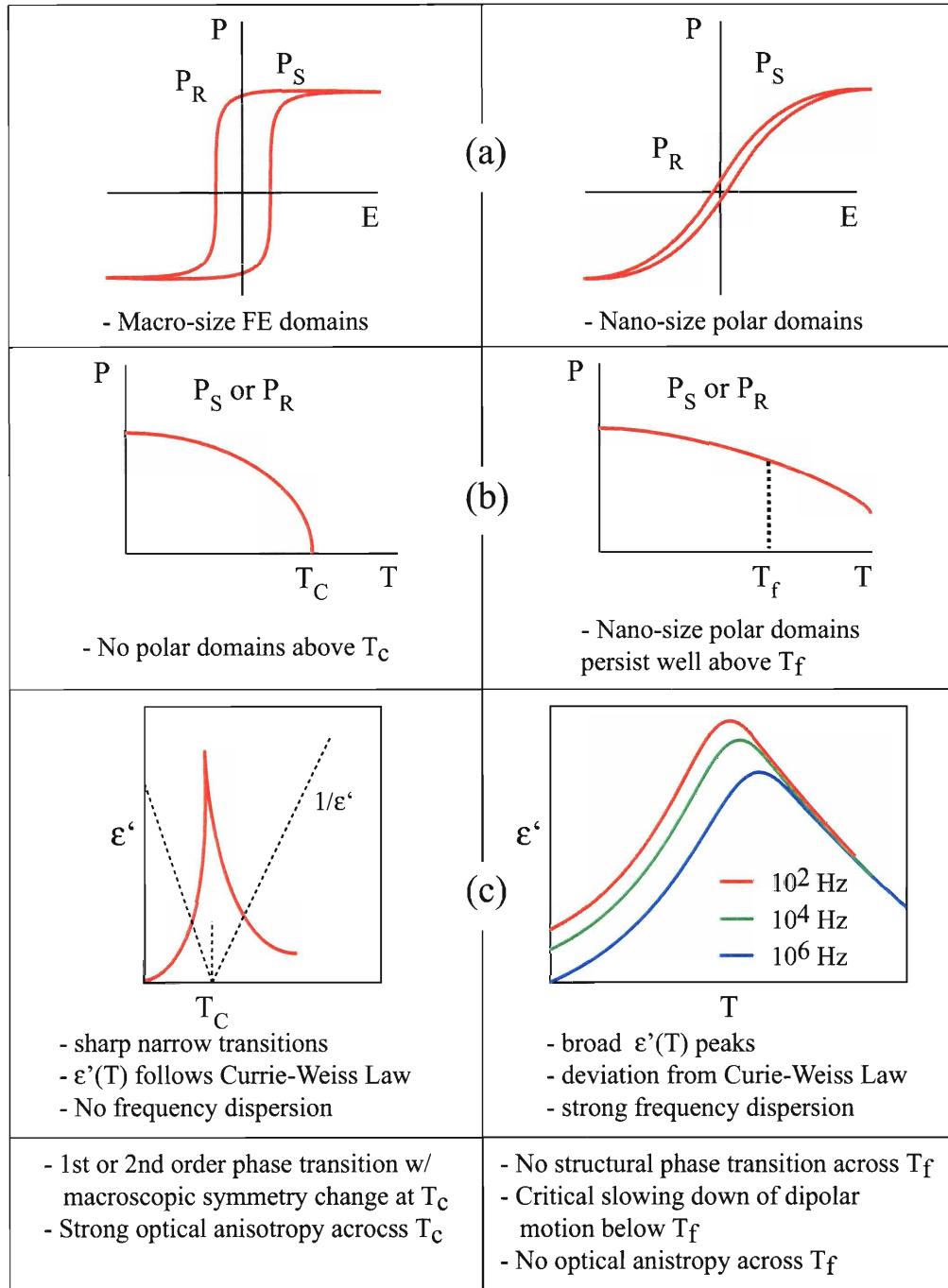


Figure 5-4: Overview of differences between normal ferroelectrics and relaxors. Adapted from Samara [7].

Chapter 6

Spectroscopic Studies of Nb Dynamics in KTN

Relaxor ferroelectrics are an important and complex class of materials. Extensive experimental and theoretical efforts have been directed toward understanding their basic physics, and although much progress has been made, fundamental questions remain [7, 99, 100]. This thesis examines a model class of relaxors, dilute Nb substituted $\text{KTa}_{1-x}\text{Nb}_x\text{O}_3$ (KTN), and provides new insights into the dynamics of the Nb impurities. It is well known that the Nb ions displace off center and act as dipole impurities in the polarizable KTaO_3 host. At low temperatures and low concentrations the Nb ions induce dynamically fluctuating polar nano-regions (PNRs), and it has been proposed by Toulouse [8, 101] that the dynamics of the Nb ions and the PNR occur on separable time scales, a fast time scale associated with soft mode assisted hopping of the Nb ions and a slower reorientation of the PNRs. This motivates our two main experiments, high frequency dielectric spectroscopy and ISRS measurement of the KTN soft mode frequency. Phonon-polariton spectroscopy is used to make the first dielectric measurements in the $\sim 50\text{-}250$ GHz range on KTN, and our results indicate significant differences from low frequency ($< 10^{-7}\text{Hz}$) dynamics that we attribute to Nb motion separated from the PNR dynamics. The lowest transverse optic phonon mode (the soft mode) is also measured through ISRS and related to the Nb dynamics.

Section 6.1 introduces KTN and motivates it as a model system for understanding relaxor behavior. Next, sections 6.3 and 6.4 introduce the polariton spectroscopy results and the ISRS soft mode experiments. Then, section 6.5 demonstrates some free space THz spectroscopy results at high temperatures. Finally section 6.6 summarizes our results and discusses future directions for experiments.

6.1 Introduction to KTN

The ABO_3 perovskite relaxors are the most studied and technologically important class of relaxors [100]. They are based on three main parent compounds, $PbNbO_3$, $PbTiO_3$, and $KTaO_3$, that are all prototypical soft mode systems whose dielectric properties and phase transitions are well understood in terms of a displacive soft mode. As disorder is introduced into the parent compounds with chemical impurities, they begin to display relaxor behavior, characterized by a diffuse frequency dependant dielectric maximum, and local ordering via the formation of the polar nano-regions (PNRs). The chemical nature of the disorder that induces the relaxor behavior can be introduced in a variety ways: (1) in $PbMg_{1/3}Nb_{1/3}O_3$ (PMN), the substituents, Nb^{5+} and Mg^{2+} on the B cation site, have differences in valences, ionic radii (0.64 Å vs. 0.72 Å) and electronegativities (1.6 vs 1.2 Pauling scale); (2) in the La-substituted $PbZr_{1-x}Ti_xO_3$ (PLZT) relaxors, high concentrations (but still random distributions) of Pb^{2+} vacancies are created by substitution of La^{3+} for Pb^{2+} (one vacancy for every two La^{3+}) at the A site, producing the relaxor behavior; and (3) in $KTaO_3$ the substitution of Nb^{5+} for Ta^{5+} (B site) and Li^+ and K^+ (A site) leads to dipolar defects at low concentrations [100]. Although it is clear that the chemical interactions are important for relaxor behavior, the variety of ABO_3 relaxors suggests that structure plays an important role as well. The $KTaO_3$ parent compound has some advantages as a model system for studying relaxor behavior, and in particular the effect of structure on relaxor behavior. The advantages consist of the similarity of cation substituents, the small amount of substitution needed to induce relaxor behavior, and the relative simplicity of host. $KTaO_3$ is one of the few ternary perovskites that does not have a

ferroelectric phase transition, and it is also well understood by soft mode theory. It is also notable that the substituted KTaO_3 relaxors constitute one of the few known classes of non-lead based relaxors [102]. The dilute impurities in soft mode crystals also are connected more easily to existing first principles models [103, 104]. For these reasons the substituted KTaO_3 compounds have been extensively studied [7, 8, 105], by Raman [96, 99, 106, 107], hyper Raman [108], x-ray [97, 98], neutron [109], dielectric [107, 110], and NMR [8, 111] spectroscopies.

The phase composition diagram of $\text{KTa}_{1-x}\text{O}_3$ (KTN) is well known. From $0.1 < x \leq 1$, on cooling KTN undergoes structural phase transitions from paraelectric cubic to FE tetragonal to FE orthorhombic to FE rhombohedral just like pure KNbO_3 discussed in chapter 5. For $0.04 < x < 1$, the situation is less clear. There is some evidence for three transitions while other evidence indicates a single phase transition to a ferroelectric state. In the dilute limit ($x \leq 0.04$) evidence now strongly indicates that there is no structural phase transition and no long range ferroelectric order [97]. This was not immediately clear however [103, 112, 113], for two main reasons. First, dilute KTN displays only slight frequency dependence in its low frequency dielectric spectra (an early defining characteristic of a relaxor). Second, in the literature [99, 108], and in our own data presented in section 6.4, the maximum of the dielectric spectra is connected with a change in the average local symmetry [96] which was suggestive of a structural transition. It was not until pressure experiments that readily induced frequency dispersion were reported by Samara in 1984 [110] that dilute KTN was understood to be a relaxor. Relaxor behavior has subsequently been well established by demonstration of the existence of PNR's under normal pressure. Work by Toulouse [8] has estimated that these regions form in dilute KTN $\sim 25\text{-}30$ K above the the maximum of the dielectric spectra T^* . This temperature is the Burns temperature, T_B . This discovery of relaxor behavior in KTN motivated much interest in the location of the substituted Nb ions, which because of their similar size to Ta^{5+} ($r \sim 0.72 \text{ \AA}$ for both) were often assumed to occupy the center of the perovskite until X-ray absorption fine structure (XAFS) experiments by Hanske-Petitpierre [98] showed that in KTN 9% Nb ions are displaced by 0.15 \AA to the eight symmetrical

[111] off center positions, while the Ta ions stayed on center in the temperature range studied (well above T_B). This work also showed that both of these positions did not seem to change with composition or with the ferroelectric transition temperature (T_c) that occurred at this concentration. Moreover, it also showed that there is Nb related disorder above and below this transition. The off center displacement of the Nb ions is easily rationalized because in this position they can simultaneously bond to three O ions, and that KNbO_3 has this bonding in its ferroelectric phase while KTaO_3 does not have a ferroelectric transition. These experiments imply that the Nb displacement is due to short range cooperative effects and not long range ferroelectric ordering.

We can now describe an intuitive picture of KTN and the PNR dynamics. The offset Nb ions have a polar soft mode vibration about an offset position. The triply degenerate soft mode has a vibrational coordinate in the direction of the hopping between equivalent sites, and in this manner the soft mode assists the Nb ion. At high temperatures, the Nb ions hop rapidly among the eight sites and are on average on center. The neighboring Ta ions are not polarized (i.e. not correlated to the Nb ions). As the temperature begins to cool, PNRs begin forming around Nb ions (or clusters of Nb ions, since they are randomly distributed) and Ta ions begin to move off center (in contrast to higher temperature where they remain on center). This should occur around $\sim 60\text{K}$ for our particular KTN sample. These PNRs are dynamical in size and follow the correlated motion of the Nb ions in the cluster. As the temperature is lowered further, the average correlation length r_c of these PNRs continues to grow. This is depicted schematically in figure 6-1.

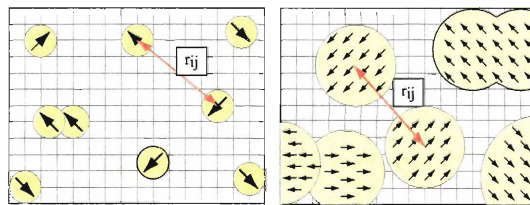


Figure 6-1: Schematic drawing of PNR formation. At high temperature the correlation length r_c is on the order of one lattice constant. At lower temperatures the dipole induces a polarization in several unit cells around it forming a PNR. Adapted from Samara [7].

The correlation length is determined by the polarizability of the host KTaO_3 crystal which is inversely proportional to the KTaO_3 host soft mode frequency. For low frequencies ($<10^{-7}$ Hz at which the PNRs can respond) the correlation length is also related to the index of refraction ($n = \sqrt{\varepsilon'}$),

$$r_c(T) \sim \frac{1}{\omega_s(T)} \sim \sqrt{\varepsilon'(T)}. \quad (6.1)$$

ω_s is the soft mode of the host lattice, and r_c is the correlation length. The large dielectric constant of dilute KTN can be intuitively understood from the behavior of these PNRs. They are essentially a large dipole moments dynamically fluctuating in size and orientation. The fluctuations in orientation are believed to follow the Nb ions as they hop between equivalent sites. A small applied field can align the fluctuating PNRs and induce a large change in the polarization, yielding a large dielectric constant (60,000 to 100,000 measured in KTN) [105]. There are two competing effects as the temperature is lowered. The dipole moment ($\sim r_c$) increases, but the PNRs (and the Nb motion) begins to “freeze” as the off center Nb and Ta ions are restricted from 8 to 4 to 2 and finally 1 site within the unit cell, as occurs in KNbO_3 in its sequence of phase transitions. The set of allowed sites in a PNR defines its polar orientation and, in this dilute limit, the polar orientation of different PNRs are randomly distributed. The soft mode assisted hopping of the Nb ions between allowed sites (at a given temperature) is an activated process, and it has been modeled with the Arrhenius equation or more commonly, to account approximately for the dipolar interactions, with a Vogel-Fulcher expression [7],

$$\tau^{-1} = \nu_0 \exp \left[\frac{-E_a}{k(T - T_0)} \right] \quad (6.2)$$

where τ is the average relaxation time, ν_0 is an attempt frequency, E_a is an activation energy, and T_0 is a reference temperature. For KTN, E_a/k has been measured to be ~ 70 K (50 cm^{-1}) [114]. This a relatively low activation barrier, which leads Nb ions to reorient very rapidly among allowed sites and to strongly couple via the soft phonon mode, which they can follow adiabatically [105].

Eventually as the temperature is lowered far enough the PNRs eventually freeze into what is commonly described as a dipole glass. When the PNR (or Nb ions) begins to freeze, the polarization realignment begins to rapidly decrease with temperature and consequently so does ε' . Therefore T^* , which marks the onset of freezing, is also associated with the maximum of the $\varepsilon'(T)$, and for this reason is loosely defined as a dynamical transition temperature, or more properly as a relaxation condition. A freezing temperature $T_f < T^*$, can be defined from the dielectric spectra by dramatic drop in the dielectric constant.

The frequency dependence of dielectric constant stems from the distribution of dipole sizes, but strain effects seem to play an important role too, particularly in the case of KTN and KLT. The Nb offset of KTN is small compared to the offset of the Li in KLT. Toulouse [105] has argued that in some relaxors, like KLT, the relaxation of the electric dipole moments associated with offset Li atom is strongly coupled to the relaxation of their associated strain field induced by this displacement, and this coupling leads to a large frequency dispersion. In other relaxors, such in our KTN sample, the coupling between the Nb and the lattice through strain is weak and this allows the Nb relaxation to occur at higher frequencies decoupled from the lower frequency lattice.

To summarize, it is clear that the Nb ions, their displacements and dynamics, play an important role in the relaxor behavior of KTN. The microscopic picture is complicated, and in spite of many investigations, the origin of the Nb off center shifts and the Nb dynamics in KTN are still not well understood [8]. To emphasize several important points however, (1) It has been well established that PNR exist and dominate the dielectric spectrum at low frequency, and (2) the soft mode plays an important role in the Nb dynamics. This thesis uses phonon-polariton spectroscopy to probe the Nb dynamics at high frequency (50-250 GHz) where it appears the Nb contribution can be separated from the PNR dynamics, in contrast to low frequency dielectric measurements both the Nb and the PNR contribute simultaneously and cannot be separated. Secondly, we present optical ISRS measurements to measure the temperature dependence of the soft mode in KTN at multiple wavevectors.

The $\text{KTa}_{0.982}\text{Nb}_{0.018}\text{O}_3$ (KTN 1.8) sample used in the following experiments is sample number 32b provided Prof. Jean Toulouse of Lehigh University. Physically its dimensions are 5.0 x 2.5 x 1 mm, and the large face is the [100] orientation. The sample was prepared on 17-9-87 with a composition of Nb = 0.018, and will subsequently be referred to as KTN 1.8. For this concentration, the mean Nb-Nb distance is 3.8 unit cells. It has been well established that for KTN 1.8 there is no structural phase transition and no long range macroscopic ferroelectric order at low temperatures.

6.2 Phonon-Polariton Spectroscopy of KTN

Phonon polariton spectroscopy was used to measure the real part of the dielectric constant, ε' (or equivalently n) from 300 to 4 K at a frequency of ~ 50 -250 GHz. To our knowledge, these are the first measurements performed on KTN (or any relaxor) in this frequency range. The entire range was covered with polariton reflection spectroscopy. Transmission polariton and free space THz spectroscopy proved more difficult because of the dielectric contrast and strong absorption of the sample and were limited to temperatures above 80 and 150 K respectively. One of the main motivations of phonon-polariton spectroscopy was to investigate these types of high dielectric materials. The dielectric spectroscopy results are shown in figure 6-2. This is the culmination of extensive experimental efforts in developing our implementation of polariton spectroscopy and a more thorough discussion of the raw data of these experiments is warranted. Figure 6-3 shows unprocessed polariton transmission spectroscopy results for a cut three crystal geometry. Several features of the transmission data stand out. At 150 K the polariton signal that is measured in the second crystal has been appreciably delayed by the change in refractive index of KTN. The peak is well defined, which stands in stark contrast to our free space transmission THz spectroscopy measurements where the transmitted peak was barely detectable at 150 K. The cut crystals used in the transmission measurements were optimized for room temperature experiments, and at lower temperatures the polariton waveform does

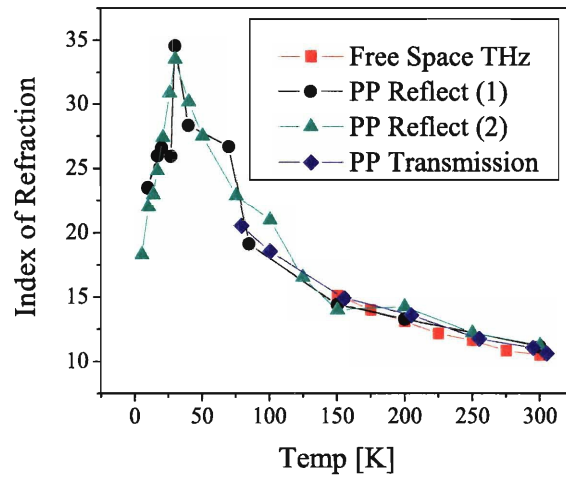


Figure 6-2: The temperature dependence of KTN's index of refraction at ~50 to 250 GHz measured with free space THz spectroscopy, two trials of phonon-polariton reflection spectroscopy, and phonon-polariton transmission spectroscopy with cut crystals.

not strike the sample at normal incidence. Nevertheless, weak polariton propagation is observed down to 80 K where figure 6-2 shows that the refractive index of KTN 1.8 begins to dramatically rise.

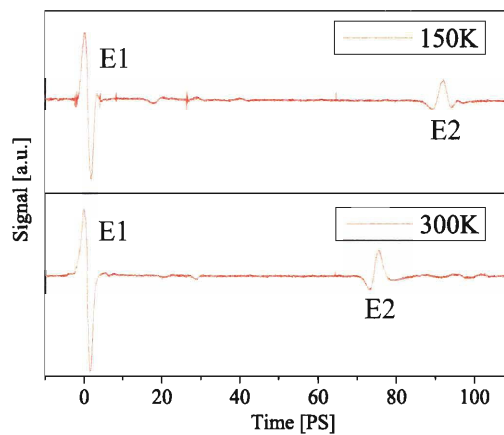


Figure 6-3: Unprocessed data from polariton transmission measurements of KTN 1.8. At 150 K the time of flight of the transmitted peak E2 significantly increased due to the refractive index change of KTN.

The bandwidth of the transmitted polariton waveform pulse varies with temperature, but at room temperature it is similar to the bandwidth of a reflected polariton waveform. Figure 6-4 shows the power spectrum for a polariton waveform before and after it has reflected from KTN 1.8 at room temperature. The bandwidth of the reflected polariton is does not differ significantly as a function of temperature, even when reflection at the KTN interface at its maximum. The spectral amplitude of E2 is an important determinant of the data extraction at a given frequency, however the high frequency side of the spectra generally produces better extracted values for the n and, when relevant, κ too.

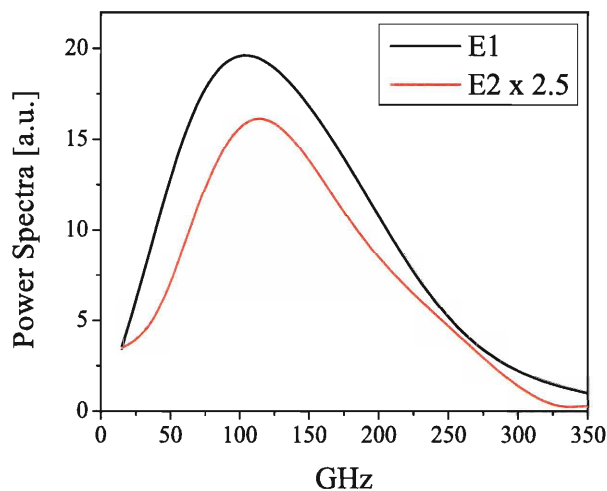


Figure 6-4: Power spectra of a polariton waveform generated with cylindrical lens ($f = 20$ cm) before and after reflection from KTN 1.8 at 300 K.

Figure 6-5 presents unprocessed data from polariton reflection spectroscopy measurements of KTN 1.8 as a function of temperature. A blue box is used to highlight the reflected polariton waveform. The reflected polariton waveform clearly increases in area as the temperature is lowered to 30K, and this change in area forms the basis of the determination of KTN dielectric properties through reflection measurements. A pink box is used to signify the polariton waveform that propagated leftward through

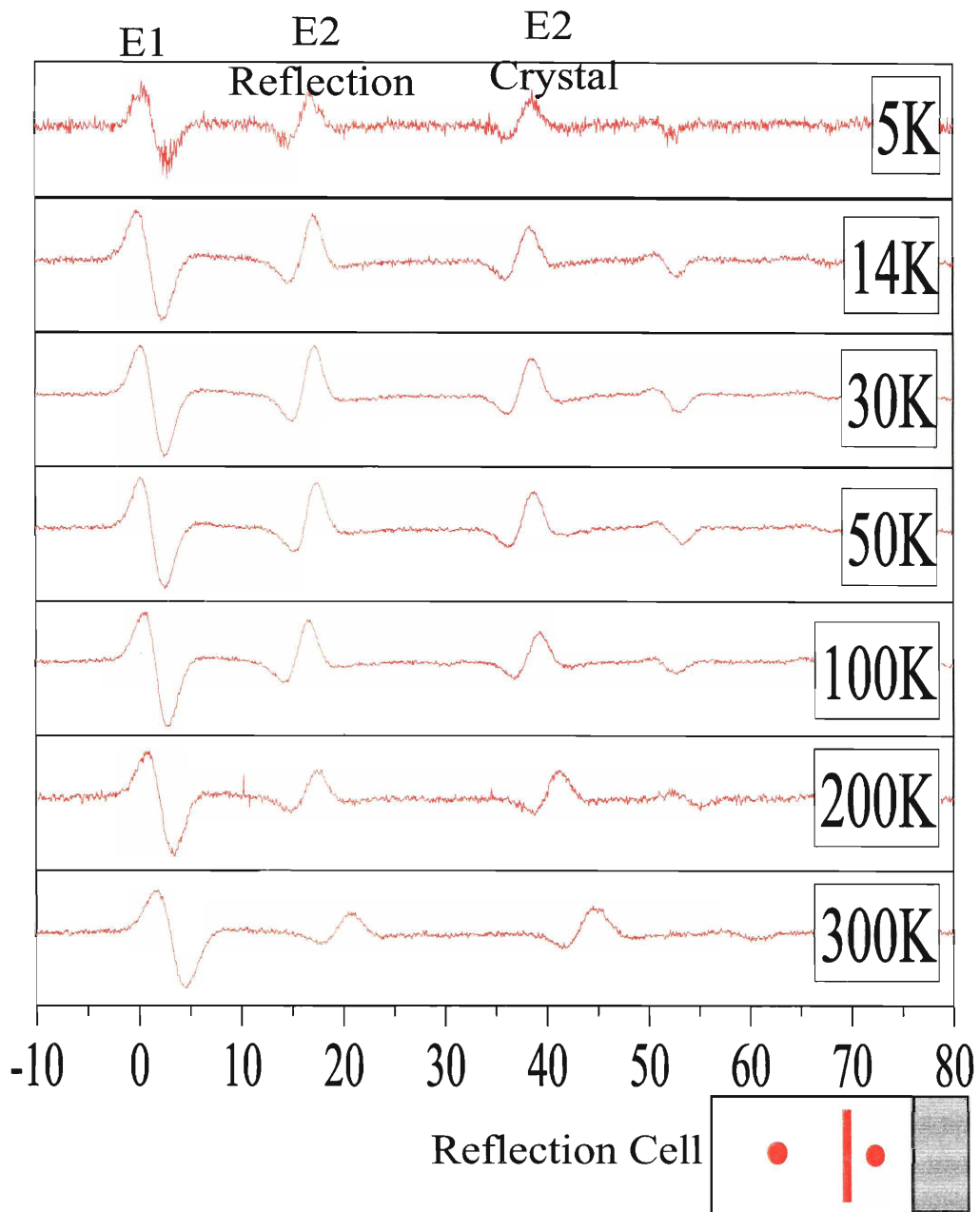


Figure 6-5: Unprocessed data from polariton reflection spectroscopy measurements of KTN 1.8. A schematic of the relative positions of the pump and probe beams is shown at the bottom of the figure. The blue region designates the the reflected polariton signal. The pink region designates the left propagating polariton passing through the left probe arm and can be used to determine the temperature dependent dielectric properties of the LiTaO_3 crystal.

the LiTaO₃ crystal away from the sample. This waveform can be used to measure the temperature dependent dielectric constant of the generation crystal, as in the single crystal experiment detailed in section 4.3.2. A fourth pulse is present in the time series. This is a reflection from the end of the crystal and does not provide any useful information.

6.3 Discussion of KTN Polariton Spectroscopy

The dielectric spectroscopy measurements show a maximum, T^* , in n of approximately ~ 30 K. This is consistent with lower frequency dielectric measurements. It is instructive to compare our high frequency results to some low frequency measurements on KTN 2.0 by Samara [110], as is done in figure 6-6. KTN shows negligible

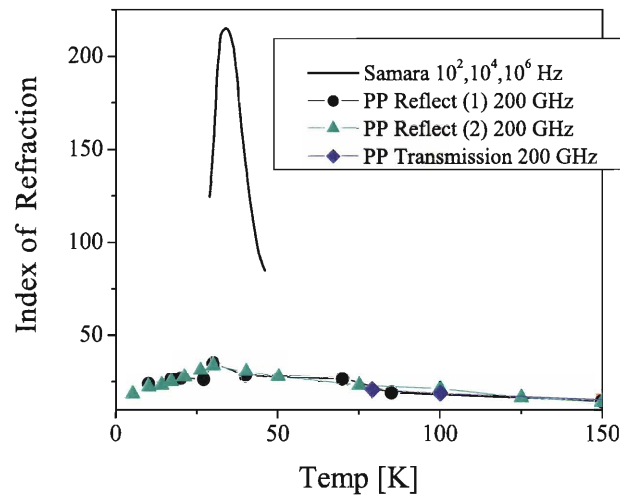


Figure 6-6: Refractive index measured with polariton transmission and reflection spectroscopies (~ 50 -250 GHz) on KTN 1.8, presented alongside dielectric spectroscopy at lower frequencies by Samara on KTN 2.0 [110].

low frequency dispersion at ambient pressure, so data from 10^2 , 10^4 , and 10^6 Hz plots are indistinguishable. The most striking feature of the comparison is the dramatic difference in amplitude. Clearly, relaxation processes that occur on the slower

timescales are not occurring at GHz frequencies. It will be subsequently argued that these relaxation processes are related to the PNRs and that our measurements reveal distinct Nb dynamics.

The maximum value of the refractive index, ~ 35 , over our bandwidth is too high to be significantly electronic. It must contain an ionic contribution and the polarization due to motions of niobium ions is a likely candidate. Three features of our experiments suggest this. First, the Curie-Weiss dependence of the dielectric constant, presented in figure 6-7, strongly suggests that it is measuring the contribution of the soft mode to the index. Secondly, the maximum of $n(T^*)$ occurs at a slightly slower temperature than T^* at low frequency which hints that the freezing dynamics differ from those of the PNRs. Finally, at 250 GHz, the polariton frequency is approaching the soft mode frequency, but is below it, and this IR active mode can be driven at this frequency. The most compelling evidence that the high frequency

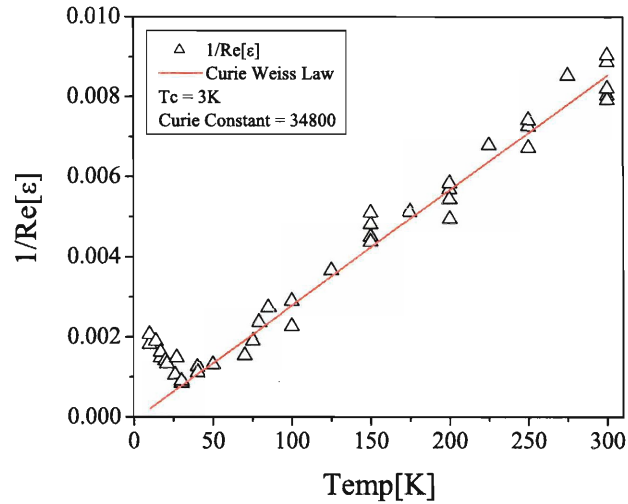


Figure 6-7: Curie-Weiss plot of $1/\epsilon'$ for all polariton spectroscopy data. A linear regression was fit to the high temperature data (150-300 K) and appears to describe all of the dielectric data above T_f at ~ 30 K.

dielectric spectroscopy is measuring the Nb dynamics is the linear dependence (above T_f) of the Curie-Weiss plot shown in figure 6-7. A fit of the high temperature data

(150-300 K) was performed and plotted against the entire dielectric data set. These temperatures are well above the temperatures that the PNRs form and where low frequency dielectric measurements also have a Curie-Weiss dependence. This linear dependence suggests that the experiment is measuring the contribution from the soft mode to ϵ' , with the associated contribution from the niobium ions hopping between allowed sites. The fast hopping motion of the niobium will easily follow the soft mode and should contribute to the index down to the freezing temperature. In contrast, it is a well known property of relaxors that the PNRs cause deviations from the Curie-Weiss law, and in particular the plot of $1/\epsilon'$ vs T based on dielectric measurements at lower frequencies extrapolates to a temperature above T^* . In fact deviation of Curie-Weiss behavior at low temperatures, but above T_f , is often used as evidence for the formation of the PNRs. The estimate of the Curie constant of 34,800 also seems reasonable (although quite large for most materials), and is similar to the Curie Constant of $\sim 65,000$ derived from low frequency dielectric measurements on a KTN 1.2 sample [115]. While the linear dependence of the Curie-Weiss plot is physically meaningful, the extrapolation below T_f to T_c suggests what would have occurred if the condensation of the PNRs had not intervened.

The second observation is that the maximum of $n(T^*)$ in our high frequency data occurs at slightly lower temperature than at lower frequencies in a sample of KTN 2.0. This may be because higher concentrations of KTN have higher T^* values, but when evaluated in conjunction with the Curie-Weiss behavior it may suggest that the Nb dynamics “freeze” separately for the PNRs. T^* usually corresponds to the lowest frequency point of the soft optic mode and in conventional ferroelectrics it marks the transition. In KTN 1.8, there is no ferroelectric transition and the maximum in relaxors does not mark a phase transition but only corresponds to the relaxation condition, $\omega\tau=1$, where ω is the attempt frequency (believed to be the soft mode frequency in KTN) and τ is the average relaxation time. In KTN at higher Nb concentrations, a sharp drop becomes visible on the low temperature side of the dielectric peak. This is where “freezing” occurs, denoted T_f . Several experiments indicate that most dynamics stops below this temperature, most notably the fast

niobium dynamics, yet without long range ferroelectric order being established [8]. Our maximum T^* is closer to this Nb freezing T_f , and therefore suggests that we are measuring the Nb dynamics. It is not clear that at our Nb concentration the Nb dynamics stop (i.e. the Nb ions are restricted to one site) at T^* and the magnitude of the low temperature tail of the refractive index seem to indicate that Nb dynamics continue at lower temperatures. By 20 K, however, the soft mode is well defined, indicating that the Nb ions have become more localized.

6.4 ISRS Measurement of the KTN Soft Mode

ISRS measurement using the transient grating geometry described in section 2.4 was used to examine the temperature and wavevector dependence of the transverse optic soft mode in KTN. The frequency of the soft mode was found to be wavevector independent at 10 and 20 K. The wavevector dependence at 10 K is presented in figure 6-9. This strongly supports the literature picture that in KTN 1.8 there is no long

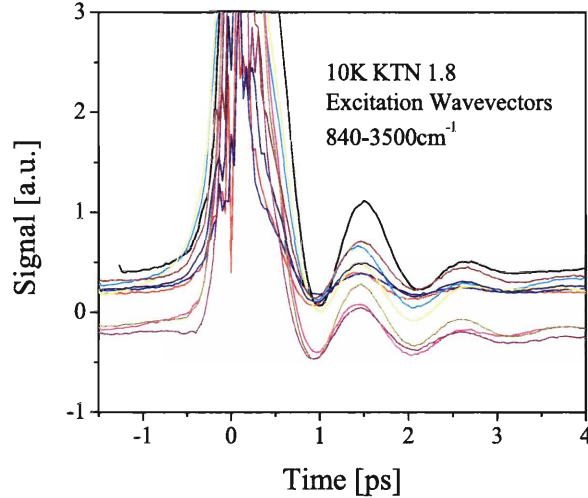


Figure 6-8: Wavevector dependence of the KTN 1.8 soft mode at 10 K, where the magnitude of the wavevector ranged from 840 to 3500 cm^{-1} .

range ferroelectric order, as this would be expected to lead to phonon-polariton modes

and wavevector dispersion (as in the case of LiTaO_3 and LiNbO_3) in the transverse optic phonon mode. Measurement of the temperature dependence of the soft mode

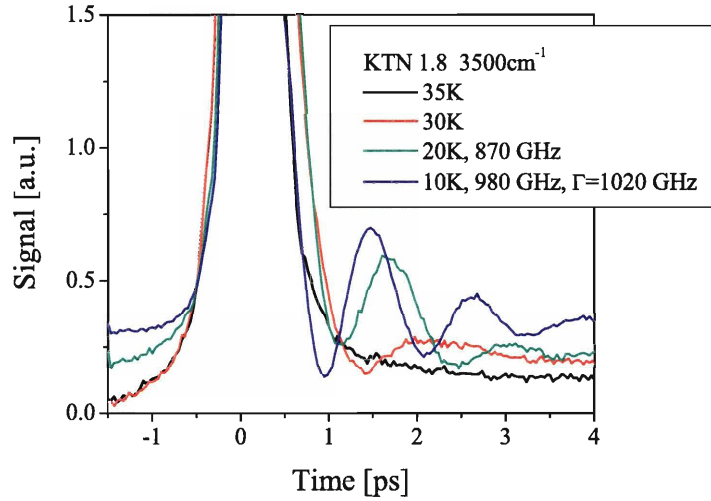


Figure 6-9: Transient grating ISRS measurement of the KTN 1.8 soft mode as a function of temperature. The magnitude of the excitation wavevector is 3500 cm^{-1} .

was possible over a limited temperature range. The temperature dependence of the soft mode is presented in figure 6-9. Above the dynamical freezing temperature, T^* , the soft mode was not observed. It is observed at low temperatures despite the overall cubic symmetry of the sample (in which the mode is Raman inactive) because of local symmetry breaking associated with the PNRs. As the temperature is increased from 10 K to through T^* , the damping of the soft mode increases and the multiple oscillations disappear. At higher temperatures than T^* , the absence of the soft mode in our studies is attributed to insufficient symmetry breaking in the PNRs at temperatures well away from T^* and strong damping near T^* . The soft mode response in figure 6-9 was fitted to a damped sinusoid, and at 10 K the soft mode frequency was determined to be 980 GHz with a damping rate of 1020 GHz. Attempts to fit the response at higher temperatures were unsuccessful, although at 20 K the soft mode frequency was determined to be 870 GHz but a reliable damping

rate could not be extracted.

Physically the soft mode damping rate can be thought of as a result of increased coupling to the Nb hopping as the soft mode frequency approaches the hopping rate. This results in the soft mode changing from underdamped (oscillatory) to overdamped. This change was suggested in Raman measurements of the soft mode [96, 106], but the measurement is far more difficult in the frequency domain where broad Raman lines overlap with the central peak. This is very similar to what is observed in inelastic neutron scattering: the soft mode measured at small wavevectors disappears from the spectrum [115]. The disappearance of the short wavevector soft mode from the spectrum coincides with the beginning of freezing (condensation) of the PNRs.

In an optical alignment similar to our polariton spectroscopy measurements, an optical pump beam was focused to a line over one arm of the dual arm grating based interferometer in KTN 1.8. This interferometer measures the same response as the transient grating experiment, only instead of having a well defined wavevector, a spread of wavevectors is measured. The soft mode behavior observed was similar to that seen in the transient grating experiments and is presented in figure 6-10.

The pump probe overlap shown in figure 6-10 was also varied from complete overlap to a small amount of overlap. There was no evidence for propagating polariton modes; again this is consistent with KTN 1.8 having no long range ferroelectric order.

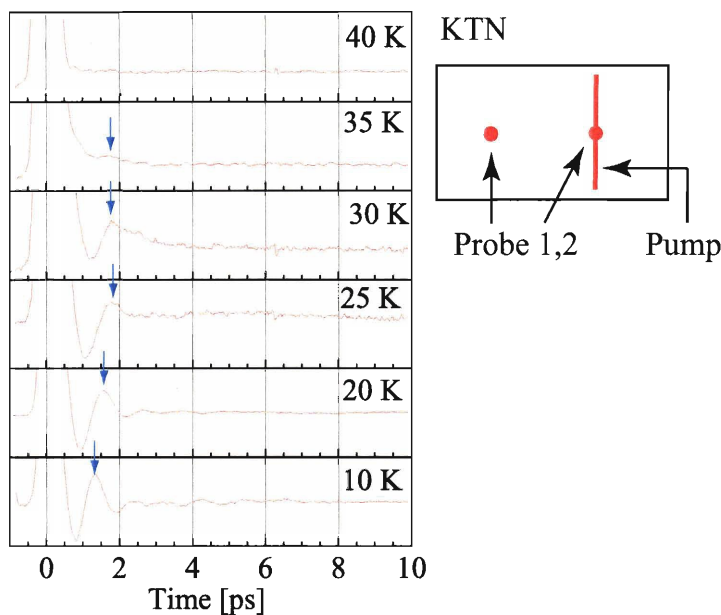


Figure 6-10: Temperature dependence of soft mode in KTN 1.8 measured interferometrically. As the temperature goes from 10 to 40 K the soft mode oscillation (blue arrows) change from underdamped to overdamped, until it disappears completely by 40 K.

6.5 Free Space THz Spectroscopy of KTN

Free space THz transmission spectroscopy measurements on KTN 1.8 were performed to serve as a comparison to the polariton spectroscopy measurements. The free space measurements permitted better frequency extraction over a wider frequency range (0.4 to 2.0 THz) and allowed for the determination of the extinction coefficient, but were only possible at relatively high temperatures. Figure 6-11 presents unprocessed times series for a reference and a transmission measurement of KTN 1.8 at 300 K.

The THz waveform that propagates through the sample is substantially reduced by a factor of ~ 50 . This is in sharp contrast to the polariton measurements where the polaritons before and after transmission are of similar size. For our temperature range of interest, 300 K should provide the highest quality free space transmission signal, as reflection, and presumably absorption, losses are greater at lower temperatures.

Figure 6-12 shows the relative spectral bandwidths for the reference and trans-

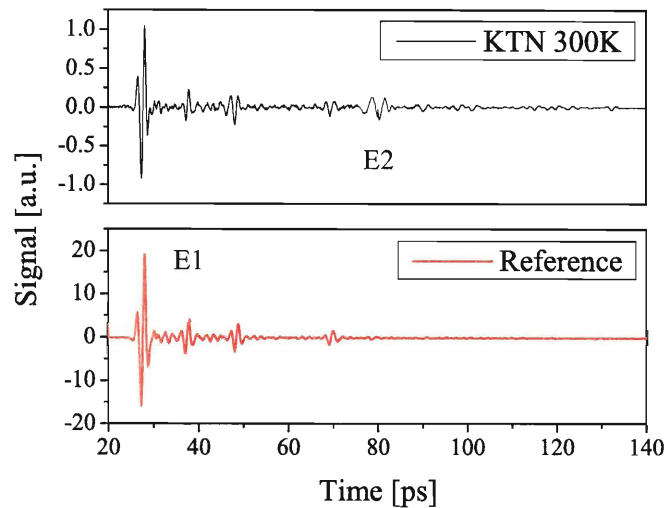


Figure 6-11: Unprocessed times series of THz transmission spectroscopy of KTN 1.8 at 300 K and a reference. The blue boxes represent the windowed portion of the time series used for data extraction. The y-axes are to the same scale.

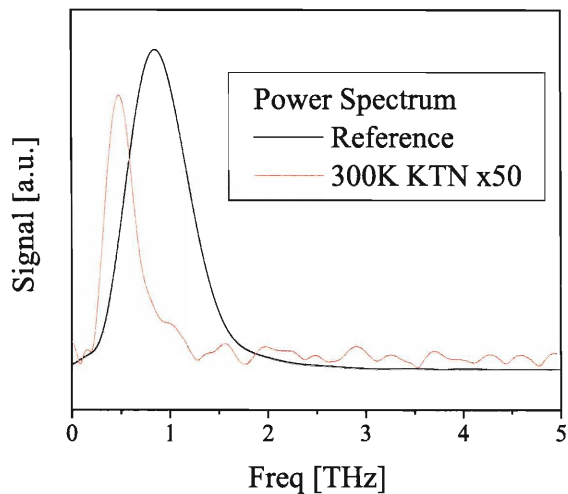


Figure 6-12: Bandwidth of the reference THz field and a THz field transmitted through KTN 1.8 at 300 K.

mitted THz fields. The overall loss of spectral amplitude and especially increased loss of spectral amplitude at higher frequencies stand out. The increased loss at high frequencies is suggestive of soft mode mediated Nb dynamics. However, Rytz [114] estimates Nb jump frequency at 300 K to be ~ 7250 GHz. Further phonon-polariton based measurements over a wide temperature and frequency range should clarify the dynamics and their underpinnings.

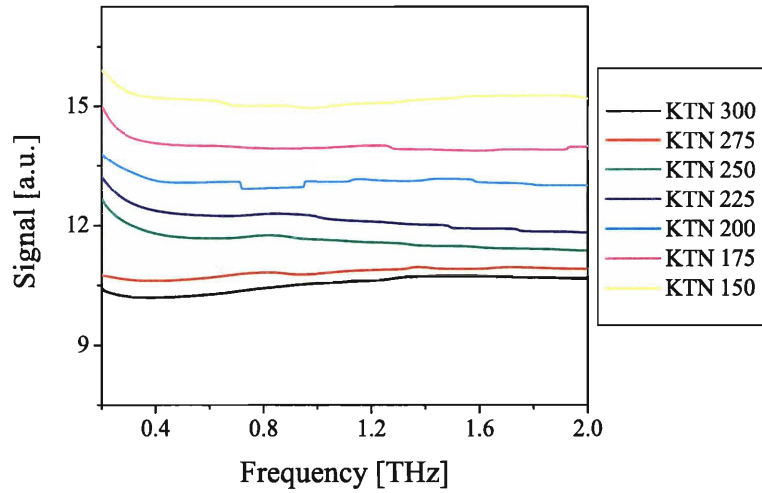


Figure 6-13: THz free space measurement of the index of refraction of KTN 1.8. Below 150 K no transmitted signal could be detected.

The results free space THz transmission spectroscopy are presented in figures 6-13 and 6-14. Unfortunately, it was not possible to obtain transmission data at temperatures below 150 K. This would actually be a quite interesting measurement as the ISRS measurements of the soft mode frequency near the transition indicate that the frequency should fall within the free space THz bandwidth. This implies that it may be possible to see frequency dependence in the THz spectrum as the Nb is unable to move between off center sites at the higher THz frequencies. The extinction coefficients, κ were also obtained from the free space measurements. They show strong absorption that appears to increase with temperature. κ could not be extracted over

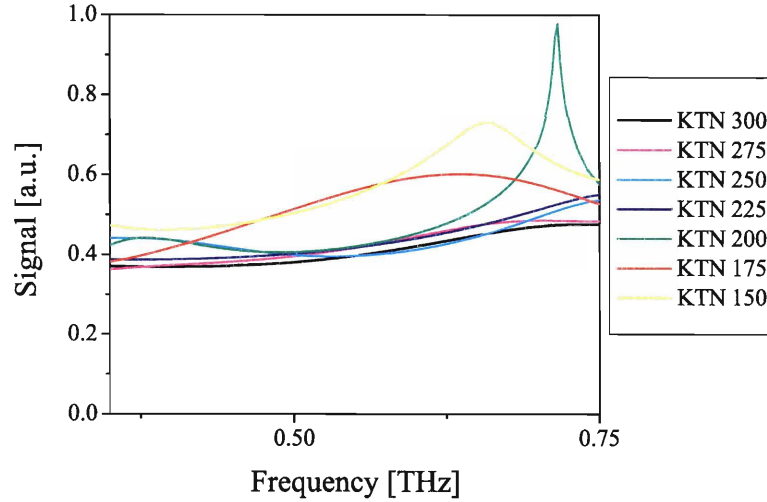


Figure 6-14: THz free space measurement of the extinction coefficient κ of KTN 1.8. Below 150 K, no transmitted signal could be detected.

the same range the refractive index, and in particular is more sensitive to spectral amplitude. The overlap and crossing of temperatures in the 300-200 K range show the relative accuracy of the THz data and not any real phenomena. In particular, for 200, 175, and 150 K the strong temperature frequency dependant features show that noise is beginning to dominate the signal as the transmitted polariton field becomes increasingly smaller.

6.6 Conclusions and Future Directions

Phonon-polariton spectroscopy was used to measure the high frequency dielectric spectrum of KTN 1.8. This is a first of kind measurement of the dielectric spectrum near the soft mode frequency of KTN. The linear dependence of the Curie-Weiss plot down to T_f strongly indicates that the dielectric spectrum is measuring the Nb and soft mode dynamics separately from PNR dynamics. This assertion is supported by the lower value of T^* which is closer to the expected freezing temperature of the Nb ions. This picture is consistent with ^{93}Nb NMR results on KTN 15 ($T_c \approx 135$ K

and ≈ 115 K) which shows that near the ferroelectric transitions, the flipping of the non-cubic domains occurs on time scales separable from those of Nb ion intersite hopping [8]. It should be noted that the NMR measurements are not directly measuring the polar dynamics of the PNR and Nb ions, but only the environment of the ^{93}Nb ions. Therefore inferring dynamics from the NMR measurements becomes significantly more challenging in the case of dilute KTN. Our dielectric spectra measure polar dynamics of the Nb ions and PNR directly without limitations due to concentration.

The soft mode experiments are also interesting, and show that THz spectroscopy should be able to span the soft mode frequency near the dynamical transition T_f . This should give a strong frequency dependent response as the polar lattice dynamics become unable to respond to the higher frequency THz radiation. As the frequency of the far-IR probe radiation is increased past the minimum soft mode frequency, the maximum of the dielectric spectrum should shift to the temperature where the soft mode and probe frequencies match. Thus extending the frequency range of the dielectric spectroscopy of KTN 1.8 would provide important confirmation that the high frequency dynamics are Nb motion along the soft mode and would provide an estimate of the soft mode properties at higher temperatures.

Another interesting experiment would be to use our phonon-polariton spectroscopy to investigate another KTaO_3 based relaxor, dilute $\text{K}_{1-x}\text{Li}_x\text{TaO}_3$ (KLT). KLT is also a relatively simple relaxor with randomly distributed Li ions in the A site which form PNR in the polarizable KTaO_3 lattice much like KTN. The relaxation is believed to be more complex though, with two relaxation processes that occur on similar timescales, one which couples to the local strain field and one that does not [105]. Furthermore the activation barrier for the Li ion is ~ 1000 K [116] which is an order of magnitude larger than that of Nb in KTN. This implies that the local distortion and strain field associated with the Li ion is much stronger than with Nb. It is therefore believed that the Li ion jump frequency is smaller than the soft mode frequency, and therefore our current implementation of polariton spectroscopy could span the frequency range where the fastest ionic polar motion occurs.

Methods are currently under development in the Nelson group to excite and probe polaritons with no forward wavevector component relative to the front and back crystals faces in LiTaO_3 and LiNbO_3 . If these efforts are successful, considerable simplifications of phonon-polariton based THz spectroscopy may be possible. In particular, they could reduce the need for cut crystals and permit a substantial improvement for transmission mode spectroscopy which could enable the extraction of both n and κ .

Chapter 7

Summary and Future Directions

Three configurations of compact THz spectrometers based on grating interferometric detection of phonon polaritons waveforms have been demonstrated. The methods for accurately analyzing spectroscopic data from the measured polariton waveforms for each of the three configurations were presented, and several important examples of polariton spectroscopy were shown over a variety of temperatures. Multicycle polariton waveforms were demonstrated with crossed pulse excitation and temporal pulse shaping. Simple free space THz spectroscopy experiments were conducted, and the relative advantages and disadvantages of polariton spectroscopy under different conditions was highlighted. For the investigation of high-dielectric materials, both reflection and transmission polariton spectroscopy offer clear advantages over free space methods, as the large refractive index of LiNbO_3 and LiTaO_3 ($n \sim 6$) at THz frequencies minimizes the dielectric contrast.

In the short term, the reflection spectroscopy configuration offers the most promise. The need to measure the polariton waveform at only one spatial location allows for a more thorough testing of various detection schemes. The most obvious candidate for a more sensitive detection scheme would be the use of polariton induced birefringence. More far-reaching directions can be grouped into two broad categories, pulse shaping and cell fabrication. Much effort has been directed toward optical pulse shaping techniques [50–58] which can generate a wide variety of polariton waveforms and this work can be extended in a spectroscopic direction. This offers many possibilities

for generating large amplitude polariton waveforms, for addressing of selected spectroscopic structures, and directing and manipulating polariton waveforms through shaping of the optical excitation pulse. Cell fabrication covers a variety of directions, the two most important of which are cell designs that minimize the impact of the forward polariton wavevector component and laser machining of submillimeter integrated spectroscopic structures, including those that might be microfluidically compatible.

Phonon-polariton based THz spectroscopy was used to make the first THz frequency dielectric measurements of a relaxor ferroelectric crystal. The refractive index of $\text{KTa}_{0.982}\text{Nb}_{0.018}\text{O}_3$ (KTN 1.8) is determined in the $\sim 50\text{-}250$ GHz range from 4-300 K. At low temperatures, the Nb ions in our sample induce dynamically fluctuating polar nano-regions (PNRs) that dominate the dielectric response at low frequencies ($< 10^{-7}$ Hz). Our results differed from low frequency measurements in two ways: a significantly smaller dielectric response was observed, and the response obeys a Curie-Weiss temperature dependence which reflects properties of the soft mode. ISRS transient grating measurements of the KTN soft mode in the low temperature disordered state show that the mode softens to sub-THz frequencies near the dielectric maximum. The soft mode frequency serves as an upper limit to the Nb dynamics, and therefore implies that our polariton spectroscopy measurements are probing the fastest structural dynamics in KTN. We attribute our GHz frequency dielectric response to soft mode mediated fast Nb intersite hopping, distinct from slower PNR dynamics.

The results of our new dielectric measurements at $\sim 50\text{-}250$ GHz suggest several interesting further experiments. Foremost is to span the soft mode frequency with dielectric spectroscopy. This should be possible with narrowband polariton or free space spectroscopy techniques. Currently the dielectric maximum is associated with the minimum of the soft mode frequency because our dielectric probe frequency is below the minimum soft mode frequency. For narrowband THz measurements that span the soft mode frequency, there should be maximum values of $n(\omega)$ at various temperatures at which the soft mode frequency reaches the THz frequency. This

will permit determination of the soft mode frequency where it is heavily damped and at temperatures where the KTN soft mode is not Raman active and cannot be observed directly in ISRS measurements. The magnitudes of the maximum $n(\omega)$ values should reveal the extent of soft mode induced Nb hopping at these frequencies and temperatures.

Phonon-polariton spectroscopy of many other relaxor ferroelectrics will provide important new insights. For example, another KTaO_3 based relaxor, dilute $\text{K}_{1-x}\text{Li}_x\text{TaO}_3$ (KLT) is also a relatively simple relaxor with randomly distributed Li ions in the A site. This relaxor forms PNRs in the polarizable KTaO_3 lattice much like KTN. The relaxation is believed to be more complex though, with two relaxation processes that occur on similar timescales, one of which couples to the local strain field and one which does not [105]. For our purposes, the two main differences between KTN and KLT are that the Li ion, which falls into a far deeper local potential minima than the Nb ions in KTN, is not believed to follow the soft mode frequency and the soft mode frequency at its minimum is expected to be lower. This is due to stronger coupling to local strain fields that hinder the faster dynamics. These two features should be readily probed with our polariton spectroscopy experiments. More generally, the complex chemically induced dynamics in different families of relaxor materials can be revealed through this class of measurements.

Appendix A

Extraction Programs

A.1 Transmission Single Crystal

```
0001 % PP transmission spectroscopy single crystal
0002
0003 % Define Conventions
0004 % complex(n) = n-ik
0005 % epsilon' = n^2-k^2
0006 % epsilon'' = 2n*k
0007 % all frequencies are in THz
0008 % all distances are in um
0009 % all velocities are in um/ps
0010
0011 %#####
0012 %#####
0013 % Clear all variables & workspace
0014 clear all
0015 addpath('E:\Data\matlab_functions');
0016 homepath = pwd;
0017
0018 % Define constants
0019 c = 300; %um/ps
0020 n_LiTaO3_800 = 2.1578;
0021
0022 % Data Files
0023 datapath = 'E:\Data\';
0024
0025 % Experimental Parameters
0026 forward_angle = asin(n_LiTaO3_800/n_LT);
0027 pr_pr = 0; %um distance between probe arms
0028 pu_pr = 0; %um distance between pump and closest probe
0029 pu_sample = 0; %um distance between pump and sample
0030 T_s = 0; %um Thickness of the sample
0031
```

```

0032 % initial guess
0033 initialguess = [n_LT,k_LT]; %[n kappal]
0034
0035 % Process Data File
0036 t = processfile(:,1); %time vector in ps
0037 dt = abs(t(2)-t(1)); %time increment in ps
0038 d1 = processfile(:,2); %signal in arbitraty units
0039 nop_raw = length(t); %nop in data time vector
0040
0041 % Geometrical Factors for cell alignment from system parameters
0042 d_s = pr_pr/cos(forward_angle); %Sample Path length
0043 dd1 = T_s - pu_pr*tan(forward_angle); %Probe Scaling factor pulse 1
0044 dd2 = T_s - (pr_pr+pu_pr)*tan(forward_angle); %Probe factor pulse 2
0045
0046 % Smooth Time Domain Data and subtract baseline
0047 windowSize = 10;
0048 d1_smooth = filter(ones(1,windowSize)/windowSize,1,d1);
0049 d1=d1_smooth;
0050 baseline = mean(d1(20:80));
0051 d1=d1-baseline;
0052
0053 % Set figure parameters
0054 figc = 0; %fig counter
0055
0056 % Select Peaks E1 & E2 from data,
0057 figc = figc+1;
0058 figure(figc);
0059 set(figc,'position','NumberTitle','off','Name','Select Data')
0060 txt = 'click on left then right bound for E1';
0061 subplot(2,1,1); plot(t,d1);xlim([min(t), max(t)]);
0062 subplot(2,1,2); plot(t,d1);xlim([min(t), max(t)]);
0063 % Select Data
0064 r1 = ginput(2);
0065 idxkeep1 = find(r1(1,1) < t & t < r1(2,1));
0066 E1 = zeros(1,nop_raw);
0067 E1(idxkeep1) = d1(idxkeep1);
0068 E1(1:idxkeep1(1)-1) = E1(idxkeep1(1))*exp(-.03*(idxkeep1(1)-1:-1:1));
0069 E1(idxkeep1(end)+1:end) =...
0070 E1(idxkeep1(end))*exp(-.03*(1:1:length(E1)-idxkeep1(end)));
0071 subplot(2,1,1); plot(t,E1); ylabel('data');
0072 % Select Reference
0073 subplot(2,1,2); plot(t,d1);xlim([min(t), max(t)]);
0074 txt = 'click on left then right bound for E2';
0075 title(txt);
0076 r2 = ginput(2);
0077 idxkeep2 = find(r2(1,1) < t & t < r2(2,1));
0078 E2 = zeros(1,nop_raw);
0079 E2(idxkeep2) = d1(idxkeep2);
0080 E2(1:idxkeep2(1)-1) = E2(idxkeep2(1))*exp(-.03*(idxkeep2(1)-1:-1:1));
0081 E2(idxkeep2(end)+1:end) =...
0082 E2(idxkeep2(end))*exp(-.03*(1:1:length(E2)-idxkeep2(end)));
0083 E2 = -E2*dd1/dd2; %Scale & negate peak 2 by the geometrical factors,
0084 subplot(2,1,2); plot(t,E2);
0085 set(figc,'NumberTitle','off','Name','Selected Reference','Position',pos2);

```

```

0086 close(figc)
0087 figure(figc); set(1,'position','NumberTitle','off','Name','Selected Data')
0088 plot(t,E1+E2); title('E1+E2')
0089
0090 % Pad Data for FFT
0091 nop      = 2^12;                               % nop for padded vector
0092 ny_ind   = 1 + nop/2;                           % index of nyquist freq
0093 E1(nop_raw+1:nop) = zeros(1,nop-nop_raw); % E1 padded
0094 E2(nop_raw+1:nop) = zeros(1,nop-nop_raw); % E2 padded
0095 t = t(1):dt:(dt*(nop-1)-abs(t(1))); % padded time vector
0096
0097 % Create Frequency vector for FFT's
0098 nu_real = (0:(nop-1))./(dt*nop); % Postive freq vector
0099 nu_fft = nu_real; % Total freq vector, +/- frequencies
0100 nu_fft(ny_ind+1:nop) = -fliplr(nu_fft(2:ny_ind-1));
0101 nu_idx = find(0 <= nu_real & nu_real < nu_plot_high); % idx's of freq
0102 nu = nu_real(nu_idx); % Freq of interest
0103 om = nu*2*pi; % Angular freq of interest
0104 % idx's for unwrapping phase
0105 nu_unwrap_idx = find(nu_unwrap_low < nu & nu < nu_unwrap_high);
0106 % idx's for extrapolating phase
0107 nu_extrap_idx = find(nu_extrap_low < nu & nu < nu_extrap_high);
0108 % Calculate FFT's & Power Spectrums
0109 E1_nu = fft(E1);
0110 E2_nu = fft(E2);
0111 E1_power = abs(E1_nu);
0112 E2_power = abs(E2_nu);
0113 [E1_power_max, E1_power_max_idx] = max(E1_power);
0114 [E2_power_max, E2_power_max_idx] = max(E2_power);
0115
0116 % Plot Power Spectrum
0117 figc = figc+1;
0118 figure(figc)
0119 set(figc,'position','NumberTitle','off','Name','Power Spectrums')
0120 subplot(1,1,1)
0121 title('Power Spectrumst');xlabel('Freq [THz]');ylabel('Signal [arb]');
0122 plot(nu, E1_power(nu_idx),nu, E2_power(nu_idx));legend('E1','E2');
0123
0124 % Calculate experimental transfer function;
0125 T_meas_nu = E2_nu(nu_idx)./E1_nu(nu_idx);
0126
0127 % Unwrap Phase of transfer function;
0128 angle_T_meas_nu = zeros(1,nu_idx(end));
0129 angle_T_meas_nu(nu_unwrap_idx) = unwrap(angle(T_meas_nu(nu_unwrap_idx)));
0130 coef = polyfit(nu(nu_extrap_idx),angle_T_meas_nu(nu_extrap_idx),2);
0131 angle_T_meas_nu = abs(angle_T_meas_nu - 2*pi*round(coef(3)/(2*pi)));
0132 % Use extrapolation to correct phase at low frequencies
0133 angle_T_meas_nu(1:nu_unwrap_idx(1)-1) = ...
0134     abs(polyval(coef,nu(1:nu_unwrap_idx(1)-1))-2*pi*round(coef(3)/(2*pi)));
0135 % Check y-intercept of unwrapped phase
0136 coef_corrected = polyfit(nu(nu_unwrap_idx),angle_T_meas_nu(nu_unwrap_idx),2);
0137 yint = coef_corrected(3)
0138 % Magnitued of Transfer Function
0139 amp_T_meas_nu = log(abs(T_meas_nu));

```

```

0140
0141 % Prepare diagnostic vectors
0142 angle_T_calc_nu = zeros(1,nu_idx(end));
0143 EF_value = zeros(1,nu_idx(end));
0144
0145 % Fit at max spectral amplitude to determin intial guess paramter
0146     clear('x')
0147     ii=E1_power_max_idx;
0148     w = nu(ii)*2*pi;
0149     ang = angle_T_meas_nu(ii);
0150     amp = amp_T_meas_nu(ii);
0151 Error_Func = @(x)(-x(2)*w.*d_s/c - amp).^2+(((x(1).*w.*d_s)./c)-ang).^2;
0152     options = optimset('MaxIter',200,'MaxFunEvals',400);
0153     [nk, EF_value(ii),exitflag,output]...
0154         = fminsearch(Error_Func, initialguess, options);
0155     EF_iter(ii) = getfield(output, 'iterations');
0156     EF_count(ii) = getfield(output, 'funcCount');
0157     initialguess(1) = nk(1);
0158     initialguess(2) = nk(2);
0159 %Clear the first few values of nextr
0160 for ii=1:4
0161     nextr(ii) = initialguess(1);
0162     kextr(ii) = initialguess(2);
0163 end
0164 tic
0165 % Fit freq middle to high
0166 for ii = 5:nu_idx(end);
0167     clear('x')
0168     w = nu(ii)*2*pi;
0169     ang = angle_T_meas_nu(ii);
0170     amp = amp_T_meas_nu(ii);
0171 Error_Func = @(x)(-x(2)*w.*d_s/c - amp).^2 + (((x(1).*w.*d_s)./c)-ang).^2;
0172     [nk, EF_value(ii), exitflag, output]...textcolorcomment
0173         = fminsearch(Error_Func, initialguess, options);
0174     EF_iter(ii) = getfield(output, 'iterations');
0175     EF_count(ii) = getfield(output, 'funcCount');
0176     nextr(ii) = nk(1);
0177     kextr(ii) = nk(2);
0178 end
0179 clear('ii')
0180 fitting_loop_time = toc
0181
0182 % Calculation of
0183 real_eps = nextr.^2-kextr.^2;
0184 imag_eps = 2*nextr.*kextr;
0185
0186 % Comparison with n & kappa from analytic solution
0187 % From moments of E1 & E2
0188 moment = norm(E2_nu)/norm(E1_nu)/exp(-k_LT*om(E1_power_max_idx)*d_s/c);
0189 n_moment = n_LT*abs((1+moment)./(moment-1));
0190 % Frequency Dependent
0191
0192 nanal = angle_T_meas_nu.*c./(d_s*om);
0193 kanal = -amp_T_meas_nu*c./(om*d_s);

```



```

0194 % Mean & std of n over region of phase extrap
0195 avg_n = mean(nextr(nu_extrap_idx));
0196 std_n = std(nextr(nu_extrap_idx));
0197 [avg_n,std_n]
0198
0199 % Plot and select n
0200 figc = figc+1;
0201 figure(figc)
0202 set(figc)
0203 plot(nu, nextr,nu, nanal);
0204 legend('nextr','nanal');ylim([4 7]);
0205 title(txt);
0206 txt = 'click on left then right bound for n';
0207 n_good=ginput(2);
0208 idx_n_good = find(n_good(1,1) < nu & nu < n_good(2,1));
0209
0210 % Plot and select k
0211 figure(figc)
0212 set(figc,'position',[85 500 800 500],'NumberTitle','off','Name','kappa')
0213 plot(nu, kextr,nu, kanal);
0214 legend('kextr','kanal');
0215 title(txt);
0216 txt = 'click on left then right bound for n';
0217 k_good=ginput(2);
0218 idx_k_good = find(k_good(1,1) < nu & nu < k_good(2,1));
0219
0220 % Plot Minimization iterations
0221 figc = figc+1;
0222 figure(figc)
0223 set(figc)
0224 plot(nu, EF_iter, nu, EF_count); legend('# of iter','# of func Eval');
0225 title('Function Minimization Diagnostic'); xlabel('\nu [THz]');
0226
0227 pause
0228 for i = 1:figc
0229 close(i)
0230 end

```

A.2 Reflection Spectroscopy

```

0001 % Program for determination of the complex dielectric spectrum
0002 % for a single crystal
0003
0004
0005 % Define Conventions
0006 % complex(n) = n-ik
0007 % epsilon' = n^2-k^2
0008 % epsilon'' = 2n*k
0009 % alpha = 4*pi*nu*kappa/c;
0010 % ifft t -> freq
0011 % fft freq -> t

```

```

0012 % all frequencies are in THz
0013 % all distances are in um
0014 % all velocities are in um/ps
0015
0016 #####
0017 #####
0018 % Clear all variables & workspace
0019 clear all
0020 homedir = pwd;
0021
0022 % Define constants
0023 c = 300; %um/ps
0024 n_LiTaO3_800 = 2.1578; %2.4;
0025
0026 forward_angle = asin(n_LiTaO3_800/n_LT);
0027 pr_pr = 0; %um distance between probe arms
0028 pu_pr = 0; %um distance between pump and closest probe
0029 pu_sample = 0; %um distance between pump and sample
0030 T_s = 0; %um Thickness of the sample
0031
0032 % initial guess
0033 initialguess = [12,.5]; %[n kappa]
0034
0035 % Name output and input files
0036 processfile = load(strcat(dataroot,day,'\ ',day,'_',time,'_a.dat'));
0037 writefile = strcat(strcat(homedir,'\ ',day,'_',time,'processed.dat'));
0038
0039 % Process Data File
0040 t = processfile(:,1); %time vector in ps
0041 dt = abs(t(2)-t(1)); %time increment in ps
0042 d1 = processfile(:,2); %signal in arbitrary units
0043 nopr = length(t); %nop in data time vector
0044
0045 % Geometrical Factors for cell alignment from system parameters
0046 d_s = (pu_sample+pu_pr)/cos(forward_angle); %Sample Path length
0047 dd1 = T_s - pu_pr*tan(forward_angle); %Probe Scaling factor pulse 1
0048 dd2 = T_s - (pu_sample+pu_pr)*tan(forward_angle); %Probe factor pulse 2
0049
0050 % Smooth Time Domain Data and subtract baseline
0051 windowSize = 10;
0052 d1_smooth = filter(ones(1,windowSize)/windowSize,1,d1);
0053 d1 = d1_smooth;
0054 baseline = mean(d1(20:80));
0055 d1 = d1-baseline;
0056
0057 % Set figure parameters
0058 figc = 0; %fig counter
0059
0060 % Select Peaks E1 & E2 from data,
0061 figc = figc+1;
0062 figure(figc);
0063 set(figc,'position','Name','Select Data')
0064 txt = 'click on left then right bound for E1';
0065 subplot(2,1,1); plot(t,d1);xlim([min(t), max(t)]);

```

```

0066 subplot(2,1,2); plot(t,d1);xlim([min(t), max(t)]);
0067 % Select Data
0068 r1 = ginput(2);
0069 idxkeep1 = find(r1(1,1) < t & t < r1(2,1));
0070 E1 = zeros(1,nop_raw);
0071 E1(idxkeep1) = d1(idxkeep1);
0072 E1(1:idxkeep1(1)-1) = E1(idxkeep1(1))*exp(-.03*(idxkeep1(1)-1:-1:1));
0073 E1(idxkeep1(end)+1:end) = ...
0074 E1(idxkeep1(end))*exp(-.03*(1:1:length(E1)-idxkeep1(end)));
0075 subplot(2,1,1); plot(t,E1); ylabel('data');
0076 % Select Reference
0077 subplot(2,1,2); plot(t,d1);ylabel('E2'); xlabel('time (ps)');
0078 txt = 'click on left then right bound for E2';
0079 title(txt);
0080 r2 = ginput(2);
0081 idxkeep2 = find(r2(1,1) < t & t < r2(2,1));
0082 E2 = zeros(1,nop_raw);
0083 E2(idxkeep2) = d1(idxkeep2);
0084 E2(1:idxkeep2(1)-1) = E2(idxkeep2(1))*exp(-.03*(idxkeep2(1)-1:-1:1));
0085 E2(idxkeep2(end)+1:end) = E2(idxkeep2(end))...
0086 *exp(-.03*(1:1:length(E2)-idxkeep2(end)));
0087 E2 = E2*dd1/dd2; %Scale peak 2 by the geometrical factors
0088 subplot(2,1,2); plot(t,E2); ylabel('Reference');
0089 set(figc,'Name','Selected Reference','Position',pos2);
0090 close(figc)
0091 figure(figc); set(1,'position',,'NumberTitle','off','Name','Selected Data')
0092 plot(t,E1+E2); title('E1+E2')
0093
0094 % Pad Data for FFT
0095 nop = 2^12; % nop for padded vector
0096 ny_ind = 1 + nop/2; % index of nyquist freq
0097 E1(nop_raw+1:nop) = zeros(1,nop-nop_raw); % E1 padded
0098 E2(nop_raw+1:nop) = zeros(1,nop-nop_raw); % E2 padded
0099 t = t(1):dt:(dt*(nop-1)-abs(t(1))); % padded time vector
0100
0101 % Create Frequency vector for FFT's
0102 nu_real = (0:(nop-1))./(dt*nop); % Postive freq vector
0103 nu_fft = nu_real; % Total freq vector, +/- frequencies
0104 nu_fft(ny_ind+1:nop) = -fliplr(nu_fft(2:ny_ind-1));
0105 nu_idx = find(0 <= nu_real & nu_real < nu_plot_high); % idx's of freq
0106 nu = nu_real(nu_idx); % Freq of interest
0107 om = nu*2*pi; % Angular freq of interest
0108 % idx's for unwrapping phase
0109 nu_unwrap_idx = find(nu_unwrap_low < nu & nu < nu_unwrap_high);
0110 % idx's for extrapolating phase
0111 nu_extrap_idx = find(nu_extrap_low < nu & nu < nu_extrap_high);
0112
0113 % Calculate FFT's & Power Spectrums
0114 E1_nu = fft(E1);
0115 E2_nu = fft(E2);
0116 E1_power = abs(E1_nu);
0117 E2_power = abs(E2_nu);
0118 [E1_power_max, E1_power_max_idx] = max(E1_power);
0119 [E2_power_max, E2_power_max_idx] = max(E2_power);

```

```

0120
0121 % Plot Power Spectrum
0122 figc = figc+1;
0123 figure(figc)
0124 set(figc,'position','NumberTitle','off','Name','Power Spectrums')
0125 subplot(1,1,1)
0126 title('Power Spectrumst');xlabel('Freq [THz]');ylabel('Signal [arb]');
0127 plot(nu, E1_power(nu_idx),nu, E2_power(nu_idx));legend('E1','E2');
0128
0129 % Calculate experimental transfer function;
0130 T_meas_nu = E2_nu(nu_idx)./E1_nu(nu_idx);
0131
0132 % Unwrap Phase of transfer function;
0133 angle_T_meas_nu = zeros(nu_idx(end));
0134 angle_T_meas_nu(nu_unwrap_idx) = unwrap(angle(T_meas_nu(nu_unwrap_idx)));
0135 coef = polyfit(nu(nu_extrap_idx),angle_T_meas_nu(nu_extrap_idx),2);
0136 angle_T_meas_nu = abs(angle_T_meas_nu - 2*pi*round(coef(3)/(2*pi)));
0137 % Use extrapolation to correct phase at low frequencies
0138 angle_T_meas_nu(1:nu_unwrap_idx(1)-1) = ...
0139     abs(polyval(coef,nu(1:nu_unwrap_idx(1)-1))-2*pi*round(coef(3)/(2*pi)));
0140 % Check y-intercept of unwrapped phase
0141 coef_corrected = polyfit(nu(nu_unwrap_idx),angle_T_meas_nu(nu_unwrap_idx),2);
0142 yint = coef_corrected(3)
0143 % Magnitude of transfer function
0144 amp_T_meas_nu = log(abs(T_meas_nu));
0145
0146 % Prepare diagnostic vectors
0147 angle_T_calc_nu = zeros(1,nu_idx(end));
0148 EF_value = zeros(1,nu_idx(end));
0149
0150 % Prepare constants for reflection coefficient
0151 COS = cos(forward_angle);
0152 SIN2 = (sin(forward_angle))^2;
0153 n1 = n_LT^2;
0154
0155 % Fit at max spectral amplitude to determin intial guess paramter
0156 clear('x')
0157 ii=E1_power_max_idx;
0158 w = nu(ii)*2*pi;
0159 ang = angle_T_meas_nu(ii);
0160 amp = amp_T_meas_nu(ii);
0161 angle_T_measured = angle_T_meas_nu(E1_power_max_idx);
0162 amp_measured = amp_T_meas_nu(E1_power_max_idx);
0163 Error_Func = @(x)(log(abs(exp(-k_LT*w.*d_s/c)*...
0164 ((COS-sqrt((x^2/n1)-SIN2))/(COS+sqrt((x^2/n1)-SIN2)))))- amp).^2;
0165 options = optimset('MaxIter',200,'MaxFunEvals',400);
0166 [nk, EF_value(ii),exitflag,output] = ...
0167     fminsearch(Error_Func, initialguess(1), options);
0168 EF_iter(ii) = getfield(output, 'iterations');
0169 EF_count(ii) = getfield(output, 'funcCount');
0170 initialguess(1) = nk(1);
0171 %Clear the first few values of nextx
0172 for ii=1:4
0173     nextx(ii) = initialguess(1);

```

```

0174 end
0175 tic
0176 % Fit freq middle to high
0177 for ii = 5:nu_idx(end);
0178     clear('x')
0179     w = nu(ii)*2*pi;
0180     ang = angle_T_meas_nu(ii);
0181     amp = amp_T_meas_nu(ii);
0182 Error_Func = @(x)(log(abs(exp(-k*LT*w.*d.s/c)*...
0183     ((COS-sqrt((x^2/n1)-SIN2))/(COS+sqrt((x^2/n1)-SIN2)))))- amp).^2;
0184     [nk, EF_value(ii), exitflag, output] = ...
0185     fminsearch(Error_Func, initialguess(1), options);
0186     EF_iter(ii) = getfield(output, 'iterations');
0187     EF_count(ii) = getfield(output, 'funcCount');
0188     nextr(ii) = nk(1);
0189 end
0190 clear('ii')
0191 fitting_loop_time = toc
0192
0193 % Mean & std of n over region of phase extrap
0194 avg_n = mean(nextr(nu_extrap_idx));
0195 std_n = std(nextr(nu_extrap_idx));
0196 [avg_n,std_n]
0197
0198 % Plot and select n
0199 figc = figc+1;
0200 figure(figc)
0201 set(figc,'position','NumberTitle','off','Name','Index of Refraction')
0202 plot(nu, nextr,nu, n_normal);legend('nextr','n normal incid');ylim([0 40]);
0203 title(txt);
0204 txt = 'click on left then right bound for n';
0205 n_good=ginput(2);
0206 idxn_good = find(n_good(1,1) < nu & nu < n_good(2,1));
0207
0208 % Plot Minimization iterations
0209 figc = figc+1;
0210 figure(figc)
0211 set(figc,'position','NumberTitle','off','Name','Diagnostic')
0212 plot(nu, EF_iter, nu, EF_count); legend('# of iter','# of func eval');
0213 title('Function Mimization Diagnostic'); xlabel('\nu [THz]');

```

A.3 Transmission Spectroscopy Cut Crystal

```

0001 % PP Transmission spectroscopy Cut Crystals
0002
0003 % Define Conventions
0004 % complex(n) = n-ik
0005 % epsilon' = n^2-k^2
0006 % epsilon'' = 2n*k
0007 % all frequencies are in THz
0008 % all distances are in um

```

```

0009 % all velocities are in um/ps
0010 #####
0011 #####
0012 % Clear all variables & workspace
0013 clear all
0014 homepath = pwd;
0015
0016 % Define constants
0017 c = 300; %um/ps
0018 nLiTa03.800 = 2.1578;
0019
0020 % intial guess
0021 initialguess = [16,.5]; %[n kappa]
0022
0023 % Process Data File
0024 t = processfile(:,1); %time vector in ps
0025 dt = abs(t(2)-t(1)); %time increment in ps
0026 d1 = processfile(:,2); %signal in arbitraty units
0027 nop_raw = length(t); %nop in data time vector
0028
0029 % Experimental Paremeters
0030 forward_angle = asin(nLiTa03.800/nLT);
0031 pr_pr = 0; %um distance between probe arms
0032 pu_pr = 0; %um distance between pump and closest probe
0033 pu_sample = 0; %um distance between pump and sample
0034 T_s = 0; %um thickness of xtals
0035 xtal_dis = 0; %um offset of detection crystal
0036
0037 % Geometrical Factors for cell alignment from system parameters
0038 d_s = 1080; %thickness Sample
0039 d_LT = ((pr_pr/cos(forward_angle))-T_s); %propagation distance LT
0040 dd1 = T_s - pu_pr*tan(forward_angle); %scale factor E1
0041 dd2 = T_s -(pr_pr + pu_pr)*tan(forward_angle)+xtal_dis;%scale factor E2
0042
0043 % Smooth Time Domain Data and subtract baseline
0044 windowSize = 10;
0045 d1_smooth = filter(ones(1,windowSize)/windowSize,1,d1);
0046 d1 = d1_smooth;
0047 baseline = mean(d1(20:80));
0048 d1 = d1-baseline;
0049
0050 % Select Peaks E1 & E2 from data,
0051 figc = figc+1;
0052 figure(figc);
0053 set(figc,'NumberTitle','off','Name','Select Data')
0054 txt = 'click on left then right bound for E1';
0055 subplot(2,1,1); plot(t,d1);xlim([min(t), max(t)]);
0056 ylabel('E1'); xlabel('time (ps)');
0057 subplot(2,1,2); plot(t,d1);xlim([min(t), max(t)]);
0058 ylabel('E2'); xlabel('time (ps)');
0059 % Select Data
0060 r1 = ginput(2);
0061 idxkeep1 = find(r1(1,1) < t & t < r1(2,1));
0062 E1 = zeros(1,nop_raw);

```

```

0063 E1(idxkeep1) = d1(idxkeep1);
0064 E1(1:idxkeep1(1)-1) = E1(idxkeep1(1))*exp(-.03*(idxkeep1(1)-1:-1:1));
0065 E1(idxkeep1(end)+1:end) = E1(idxkeep1(end))*...
0066     exp(-.03*(1:1:length(E1)-idxkeep1(end)));
0067 subplot(2,1,1); plot(t,E1); ylabel('data');
0068 % Select Reference
0069 subplot(2,1,2); plot(t,d1);xlim([min(t), max(t)]);
0070 ylabel('E2'); xlabel('time (ps)');
0071 txt = 'click on left then right bound for E2';
0072 title(txt);
0073 r2 = ginput(2);
0074 idxkeep2 = find(r2(1,1) < t & t < r2(2,1));
0075 E2 = zeros(1,nop_raw);
0076 E2(idxkeep2) = d1(idxkeep2);
0077 E2(1:idxkeep2(1)-1) = E2(idxkeep2(1))*exp(-.03*(idxkeep2(1)-1:-1:1));
0078 E2(idxkeep2(end)+1:end) = E2(idxkeep2(end))*...
0079     exp(-.03*(1:1:length(E2)-idxkeep2(end)));
0080 E2 = -E2*dd1/dd2; %Scale E2 and flip
0081 subplot(2,1,2); plot(t,E2); ylabel('Reference'); xlabel('time (ps)');
0082 xlim([min(t), max(t)]);
0083 set(figc,'NumberTitle','off','Name','Selected Reference','Position',pos2);
0084 close(figc)
0085 figure(figc); set(1,'NumberTitle','off','Name','Selected Data')
0086 plot(t,E1+E2); title('E1+E2')
0087
0088 % Pad Data for FFT
0089 nop = 2^14; % nop for padded vector
0090 ny_ind = 1 + nop/2; % index of nyquist freq
0091 E1(nop_raw+1:nop) = zeros(1,nop-nop_raw); % E1 padded
0092 E2(nop_raw+1:nop) = zeros(1,nop-nop_raw); % E2 padded
0093 t = t(1):dt:(dt*(nop-1)-abs(t(1))); % padded time vector
0094
0095 % Create Frequency vector for FFT's
0096 nu_real = (0:(nop-1))./(dt*nop); % Postive freq vector
0097 nu_fft = nu_real; % Total freq vector, +/- freq
0098 nu_fft(ny_ind+1:nop) = -fliplr(nu_fft(2:ny_ind-1));
0099 nu_idx = find(0 <= nu_real & nu_real < nu_plot_high); % idx's of freq
0100 nu = nu_real(nu_idx); % Freq of interest
0101 om = nu*2*pi; % Angular freq of interest
0102 % idx's for unwrapping phase
0103 nu_unwrap_idx = find(nu_unwrap_low < nu & nu < nu_unwrap_high);
0104 % idx's for extrapolating phase
0105 nu_extrap_idx = find(nu_extrap_low < nu & nu < nu_extrap_high);
0106
0107 % Calculate FFT's & Power Spectrums
0108 E1_nu = fft(E1);
0109 E2_nu = fft(E2);
0110 E1_power = abs(E1_nu);
0111 E2_power = abs(E2_nu);
0112 [E1_power_max, E1_power_max_idx] = max(E1_power);
0113 [E2_power_max, E2_power_max_idx] = max(E2_power);
0114
0115 % Calculate experimental transfer function;
0116 T_meas_nu = E2_nu(nu_idx)./E1_nu(nu_idx);

```

```

0117
0118 % Unwrap Phase of transfer function;
0119 angle_T_meas_nu = zeros(1,nu_idx(end));
0120 angle_T_meas_nu(nu_unwrap_idx) = unwrap(angle(T_meas_nu(nu_unwrap_idx)));
0121 coef = polyfit(nu(nu_extrap_idx),angle_T_meas_nu(nu_extrap_idx),2);
0122 angle_T_meas_nu = abs(angle_T_meas_nu - 2*pi*round(coef(3)/(2*pi)));
0123 % Use extrapolation to correct phase at low frequencies
0124 angle_T_meas_nu(1:nu_unwrap_idx(1)-1) = ...
0125     abs(polyval(coef,nu(1:nu_unwrap_idx(1)-1))-2*pi*round(coef(3)/(2*pi)));
0126 % Check y-intercept of unwrapped phase
0127 coef_corrected = polyfit(nu(nu_unwrap_idx),angle_T_meas_nu(nu_unwrap_idx),2);
0128 yint = coef_corrected(3)
0129 % Magnitued of Transfer Function
0130 amp_T_meas_nu = log(abs(T_meas_nu));
0131
0132 % Fit at max spectral amplitude to determin intial guess paramter
0133 clear('x')
0134 ii=E1_power_max_idx;
0135 w = om(ii);
0136 ang = angle_T_meas_nu(ii);
0137 amp = amp_T_meas_nu(ii);
0138 ampLT = ampLT_nu(ii);
0139 angLT = angLT_nu(ii);
0140 Error_Func = @(x)(log((4x(1)*n_LT)/((x(1)+n_LT)^2)*...
0141     ampLT*exp(-x(2)*w.*d_s/c))- amp).^2+(angLT+((x(1).*w.*d_s)./c)-ang).^2;
0142 options = optimset('MaxIter',200,'MaxFunEvals',400);
0143 [nk, EF_value(ii),exitflag,output]=fminsearch(Error_Func, initialguess, options);
0144 EF_iter(ii) = getfield(output, 'iterations');
0145 EF_count(ii) = getfield(output, 'funcCount');
0146 initialguess(1) = nk(1);
0147 initialguess(2) = nk(2);
0148 %Clear the first few values of next
0149 for ii=1:4
0150     next(ii) = initialguess(1);
0151     kextr(ii) = initialguess(2);
0152 end
0153 tic
0154 % Fit freq middle to high
0155 for ii = 5:nu_idx(end);
0156 clear('x')
0157 w = nu(ii)*2*pi;
0158 ang = angle_T_meas_nu(ii);
0159 amp = amp_T_meas_nu(ii);
0160 Error_Func = @(x)(log((4x(1)*n_LT)/((x(1)+n_LT)^2)*ampLT*exp(-x(2)*w.*d_s/c))...
0161     - amp).^2+(angLT+((x(1).*w.*d_s)./c)-ang).^2;
0162 [nk, EF_value(ii), exitflag, output] = fminsearch(Error_Func, initialguess, options);
0163 EF_iter(ii) = getfield(output, 'iterations');
0164 EF_count(ii) = getfield(output, 'funcCount');
0165 next(ii) = nk(1);
0166 kextr(ii) = nk(2);
0167 end
0168 clear('ii')
0169 fitting_loop_time = toc
0170

```



```

0171 % Calculation of
0172 real_eps = nextr.^2-kextr.^2;
0173 imag_eps = 2*nextr.*kextr;
0174
0175 % Plot and select n
0176 figc = figc+1;
0177 figure(figc)
0178 set(figc,'NumberTitle','off','Name','Index of Refraction')
0179 plot(nu, nextr,nu, nanal);
0180 legend('nextr','nanal');ylim([10 25]);
0181 title(txt);
0182 txt = 'click on left then right bound for n';
0183 n_good=ginput(2);
0184 idx_n_good = find(n_good(1,1) < nu & nu < n_good(2,1));
0185 nstd_sel = std(nextr(idx_n_good));
0186
0187 % Plot and select k
0188 figure(figc)
0189 set(figc,'NumberTitle','off','Name','kappa')
0190 plot(nu, kextr,nu, kanal);
0191 legend('kextr','kanal');
0192 title(txt);
0193 txt = 'click on left then right bound for n';
0194 k_good=ginput(2);
0195 idx_k_good = find(k_good(1,1) < nu & nu < k_good(2,1));
0196 kstd_sel = std(nextr(idx_n_good));

```


Bibliography

- [1] M.C. Beard, G.M. Turner, and C.A. Schmuttenmaer. Terahertz spectroscopy. *J. Phys. Chem. B.*, 106:7146, 2002.
- [2] Richard Koehl. *Spatial and temporal ultrafast imaging and control of terahertz wavepackets*. PhD thesis, Massachusetts Institute of Technology, 2000.
- [3] T.F. Crimmins, M. J. Gleason, D.W. Ward, and K.A. Nelson. A simple terahertz spectrometer. In M.M. Murnane T. Elsaesser, S. Mukamel and N. F. Scherer, editors, *Ultrafast Phenomena XII*, pages 221–223. Springer-Verlag, 2001.
- [4] Nikolay Staykov Stoyanov. *Phonon-Polaritons in Bulk and Patterned Materials*. PhD thesis, Massachusetts Institute of Technology, 2003.
- [5] D.W. Weard. *Polaritonics: An Intermediate Regime Between Electronics and Photonics*. PhD thesis, Massachusetts Institute of Technology, 2005.
- [6] Joshua Charles Vaughan. *Two-Dimensional Ultrafast Pulse Shaping and its Application to Coherent Control and Spectroscopy*. PhD thesis, Massachusetts Institute of Technology, 2005.
- [7] George A Samara. The relaxational properties of compositionally disorderd ABO₃ perovskites. *J. Phys. Cond. Mat.*, 15:R367–R411, 1003.
- [8] S. Rankel, B Zalar, V.V. Laguta, R. Blinc, and J. Toulouse. ⁹³Nb NMR study of disorder K_{1-x}Li_xTaO₃. *Phys. Rev B.*, 71:144110, 2005.
- [9] Jaime Dawn Choi. *Generation of Ultrahigh Frequency Acoustic Waves for Characterization of Complex Materials*. PhD thesis, Massachusetts Institute of Technology, 2005.
- [10] J. D. Choi, T. Feurer, M. Yamaguchi, B. Paxton, and K. A. Nelson. Generation of ultrahigh-frequency tunable acoustic waves. *Appl. Phys. Lett.*, 87:081907, 2005.
- [11] H.J. Eichler, P. Gnter, and D.W. Pohl. *Laser-induced dynamic gratings*. Springer-Verlag, New York, 1986.
- [12] Lisa Dhar, John A. Rogers, and Keith A. Nelson. Time-resolved vibrational spectroscopy in the impulsive limit. *Chem. Rev.*, 94:157–193, 1994.

- [13] A.A. Maznev, K.A. Nelson, and J.A. Rogers. Optical heterodyne detection of laser-induced gratings. *Optics Letters*, 23:1319–1321, 200.
- [14] T.F. Crimmins, N.S. Stoyanov, and K.A. Nelson. Heterodyned impulsive stimulated raman scattering of phonon-polaritons in LiTaO_3 and LiNbO_3 . *J. Chem. Phys.*, 117:2882–2896, 2002.
- [15] A.A. Maznev, T.F. Crimmins, and K.A. Nelson. How to make femtosecond pulses overlap. *Opt. Lett.*, 23(17):1378, 1998.
- [16] T.P. Dougherty, G.P. Wiederrecht, and K.A. Nelson. Impulsive stimulated raman scattering experiments in the polariton regime. *J. Opt. Soc. Am. B*, 9:2179–2189, 1992.
- [17] Thomas P. Dougherty, Gary P. Wiederrecht, Keith A. Nelson, Mark H. Garrett, Hans P. Jenssen, and Cardinal Warde. Femtosecond time-resolved spectroscopy of soft modes in structural phase transitions of perovskites. *Phys. Rev. B.*, 1994.
- [18] T. Watanuki, S. Yoshioka, M. Kasahara, T.F. Crimmins, K.A. Nelson, and T. Yagi. Reinvestigation of the dispersion relation of A_1 phonon-polariton in LiNbO_3 by the improved heterodyne ISRS study. *Journal of the Physical Society of Japan*, 70:2784–2787, 2001.
- [19] G.P. Wiederrecht, T.P. Dougherty, L. Dhar, K.A. Nelson, D.E. Leaird, and A.M. Weiner. Explanation of anomalous polariton dynamics in LiTaO_3 . *Rev. Rev. B*, 51:916–931, 1995.
- [20] R.A. Cheville. Internet, 2006.
- [21] R.W. Boyd. *Nonlinear Optics*. Academic Press, San Diego, 1992.
- [22] A. Yariv. *Quantum Electronics*. John Wiley and Sons, New York, 1989.
- [23] C. Fattinger and D. Grischkowsky. Terahz beams. *Appl. Phys. Lett.*, 54:490–492, 1989.
- [24] D.H. Auston, K.P. Cheung, J.A. Valdamis, and D.A. Kleinman. Cherenkov radiation from femtosecond optical pulses in electro-optic media. *Phys. Rev. Lett.*, 53:1555–1558, 1984.
- [25] D.H. Auston and M.C. Nuss. Electrooptic generation and detection of femtosecond electrical transients. *IEEE J. Quant. Electron.*, 24(2):184, 1988.
- [26] Kohji Yamamoto, Mariko Yamaguchi, Fumiaki Miyamaru, Masahiko Tani, Masanori Hangyo, Takeshi Ikeda, Akira Matsushita, Kenji Koide, Michiaki Tatsuno, and Yukio Minami. Noninvasive Inspection of C-4 Explosive in Mails by Terahertz Time-Domain Spectroscopy. *Jpn. J. Appl. Phys.*, 43:L414–L417, 2004.
- [27] Mariko Yamaguchi, Fumiaki Miyamaru, Kohji Yamamoto, Masahiko Tani, and Masanori Hangyo. Terahertz absorption spectra of L-, D-, and DL-alanine and their application to determination of enantiometric composition. *Appl. Phys. Lett.*, 86:053903–053905, 2005.

- [28] R.A. Cheville and D. Grishkowsky. Far-infrared terahertz time-domain spectroscopy of flames. *Opt. Lett.*, 30:1646–1648, 1995.
- [29] L.Thrane, R.H. Jacobsen, P.U. Jepsen, and S.R. Keiding. *Chem. Phys. Lett.*, 240:330–333, 1995.
- [30] M. Brucherseifer, M. Nagel, P.H. Bolivar, H. Kurz, A. Bosserhoff, and R. Buttner. Label-free probing of the binding state of dna by time-domain terahertz sensing. *Appl. Phys. Lett.*, 77:4049, 2000.
- [31] M.C. Nuss and R.L. Morrison. Time-domain images. *Opt. Lett.*, 20:740–742, 1995.
- [32] B.B. Hu and M.C. Nuss. Imaging with terahertz waves. *Opt. Lett.*, 20:1716–1718, 1995.
- [33] P.I. Tamborenea and H. Metiu. Coherent control of multisubband wavepackets with terahertz (thz) pulses. *J. Chem. Phys.*, 110:9202–9213, 1999.
- [34] N.S. Stoyanov, D.W. Ward, T. Feurer, and K.A. Nelson. Terahertz polariton propagation in patterned materials. *Nature Materials*, 1:95–98, 2002.
- [35] C. Flytzanis. Infrared dispersion of second-order electric susceptibilities in semiconducting compounds. *Phys. Rev. B*, 6:1264–1290, 1972.
- [36] L. Xu, D.H. Auston, and A. Hasegawa. Propagation of electromagnetic solitary waves in dispersive nonlinear dielectrics. *Phys. Rev. A*, 45:3184–3193, 1992.
- [37] K. Okumura and Y. Tanimura. Two-dimensional thz spectroscopy of liquids: non-linear vibrational response to a series of thz laser pulses. *Chem. Phys. Lett.*, 4:298–304, 1998.
- [38] U. Haberle and G. Diezemann. Nonresonant holeburning in the terahertz range: Brownian oscillator model. *J. Chem. Phys.*, 120(3):1466–1476, 2004.
- [39] C. Rangan and P.H. Bucksbaum. Optimally shaped terahertz pulses for phase retrieval in rydberg-atom data register. *Phys. Rev. A*, 64:033417, 2001.
- [40] C.J. Brennan. *Femtosecond Wavevector Overtone Spectroscopy of Anharmonic Lattice Dynamics in Ferroelectric Crystals*. PhD thesis, Massachusetts Institute of Technology, 1997.
- [41] C. Kittel. *Introduction to Solid State Physics*. John Wiley and Sons, Inc., New York, 1996.
- [42] A.S. Barker and R. Loudon. Response functions in the theory of raman scattering by vibrational and polariton modes in dielectric crystals. *Rev. Mod. Phys.*, 44:18–46, 1972.
- [43] M. Born and K. Huang. *Dynamical Theory of Crystal Lattices*. Oxford, 1988.
- [44] A.S. Barker Jr. and R. Loudon. Dielectric Properties and Optical Phonons in LiNbO₃. *Phys. Rev.*, 158(2):433, 1967.

- [45] A.S. Barker Jr., A.A. Ballman, and J.A. Ditzenberger. Infrared Study of the Lattice Vibration LiTaO_3 . *Phys. Rev. B*, 2(10):4233, 1970.
- [46] Y.X. Yan and K.A. Nelson. Impulsive stimulated light scattering. i. general theory. *J. Chem. Phys.*, 87:6240–6256, 1987.
- [47] K.A. Nelson and E.P. Ippen. Femtosecond coherent spectroscopy. *Adv. Chem. Phys.*, 75:1–35, 1989.
- [48] D.A. Kleinman and D.H. Auston. Theory of electrooptic shock radiation in nonlinear optical media. *IEEE J. Quant. Elec.*, 20:964–970, 1984.
- [49] D. Cote, J.E. Sipe, and H.M. vanDriel. Simple method for calculating the propagation of terahertz radiation in experimental geometries. *J. Opt. Soc. Am. B*, 20:1374–1385, 2003.
- [50] M.M. Wefers and K.A. Nelson. Generation of high-fidelity programmable ultrafast optical waveforms. *Opt. Lett.*, 20:1047–1049, 1995.
- [51] M.M. Wefers and K.A. Nelson. Analysis of programmable ultrashort waveform generation using liquid-crystal spatial light modulators. *J. Opt. Soc. Am. B*, 12:1343–1362, 1995.
- [52] R.M. Koehl, T. Hattori, and K.A. Nelson. Automated spatial and temporal shaping of femtosecond pulses. *Opt. Commun.*, 157:57–61, 1998.
- [53] A.M. Weiner. Femtosecond pulse shaping using spatial light modulators. *Rev. Sci. Instr.*, 71:1929–1969, 2000.
- [54] J.C. Vaughan, T. Feurer, and K.A. Nelson. Automated two-dimensional femtosecond pulse shaping. *J. Opt. Soc. Am. B*, 19:2489–2495, 2002.
- [55] T. Feurer, J.C. Vaughan, R. Koehl, and K.A. Nelson. Multidimensional control of femtosecond pulses by use of a programmable liquid crystal matrix. *Opt. Lett.*, 27:652–654, 2002.
- [56] J.C. Vaughan, T. Feurer, and K.A. Nelson. Automated spatiotemporal diffraction of ultrashort laser pulses. *Opt. Lett.*, 28:2408–2410, 2003.
- [57] M.M. Wefers and K.A. Nelson. Space-time profiles of shaped ultrafast optical waveforms. *IEEE J. Quant. Elec.*, 32:161–172, 1996.
- [58] J.C. Vaughan, T. Hornung, T. Feurer, and K.A. Nelson. Diffraction-based femtosecond pulse shaping with a 2d slm. *Opt. Lett.*, 30:323–325, 2005.
- [59] M.M. Wefers, H. Kawashima, and K.A. Nelson. Optical control over two-dimensional lattice vibrational trajectories in crystalline quartz. *J. Chem. Phys.*, 108:10248–10255, 1998.
- [60] R.M. Koehl and K.A. Nelson. Terahertz polaritons: Automated spatiotemporal control over propagating lattice waves. *Chemical Physics*, 267:151–159, 2001.

- [61] R.M. Koehl and K.A. Nelson. Coherent optical control over collective vibrations traveling at lightlike speeds. *J. Chem. Phys. B*, 114:1443–1446, 2001.
- [62] R.M. Koehl, S. Adachi, and K.A. Nelson. Direct visualization of collective wavepacket dynamics. *J. Phys. Chem. A*, 103:10260–10267, 1999.
- [63] N.S. Stoyanov, T. Feurer, D.W. Ward, and K.A. Nelson. Direct visualization of phonon-polariton focusing and amplitude enhancement. *J. Chem. Phys.*, 117:2897–2901, 2002.
- [64] A.M. Weiner, D.E. Leaird, G.P. Wiederrecht, and K.A. Nelson. Femtosecond pulse sequences used for optical manipulation of molecular motion. *Science*, 247:1317–1319, 1990.
- [65] T. Feurer, J.C. Vaughan, and K.A. Nelson. Spatiotemporal control of lattice vibrational waves. *Science*, 299:374–377, 2003.
- [66] J.C. Vaughan, T. Feurer, T. Hornung, and K.A. Nelson. Typesetting thz waveforms. In T. Kobayashi, T. Okada, T. Kobayashi, K.A. Nelson, and S. De Silvestri, editors, *Ultrafast Phenomena XIV*, pages 717–719. Springer-Verlag, 2005.
- [67] T. Feurer, J.C. Vaughan, T. Hornung, and K.A. Nelson. Typesetting of terahertz waveforms. *Optics Letters*, 29:1802–1804, 2004.
- [68] Y. Sohn, Y.H. Ahn, D.J. Park, E. Oh, and D.S. Kima. Tunable terahertz generation using femtosecond pulse shaping. *Appl. Phys. Lett.*, 81:13–15, 2002.
- [69] A.A. Weiling and D.H. Auston. Novel sources and detectors for coherent tunable narrow-band terahertz radiation in free space. *J. Opt. Soc. Am. B*, 13:233–235, 1996.
- [70] Y. Liu, S.G. Park, and A.M. Weiner. Terahertz waveform synthesis via optical pulse shaping. *IEEE J. Sel. Top. Quant. Elec.*, 2:709–719, 1996.
- [71] J. Ahn, A.V. Efimov, R.D. Averitt, and A.J. Taylor. Terahertz waveform synthesis via optical rectification of shaped ultrafast laser pulses. *Opt. Express*, 11:2486–2496, 2003.
- [72] N.M. Froberg, B.B. hu, X.C. Zhang, and D.H. Auston. Terahertz radiation from a photon-conducting antenna array. *IEEE J. Quant. Elec.*, 28:2291–2301, 1992.
- [73] J. Bromage, S. Radic, G.P. Agrawal, C.R. Stroud, P.M. Fauchet, and R. Sobolewski. Spatiotemporal shaping of half-cycle terahertz pulses by diffraction through conductive apertures of finite thickness. *J. Opt. Soc. Am. B*, 15:1953–1959, 1998.
- [74] Y.S. Lee, T. Meade, T.B. Norris, and A. Galvanauskas. Tunable narrow-band terahertz generation from periodically poled lithium niobate. *Appl. Phys. Lett.*, 78:3583–3585, 2001.
- [75] N.S. Stoyanov, T. Feurer, D.W. Ward, and K.A. Nelson. Integrated diffractive THz elements. *Applied Physics Letters*, 82:674–676, 2003.

- [76] E. Hecht. *Optics*. Addison Wesley, Reading, MA, 1987.
- [77] D.W. Ward, J.D. Beers, T. Feurer, E. Statz, N. Stoyanov, and K.A. Nelson. Coherent control of phonon-polaritons in a THz resonator fabricated with femtosecond laser machining. *Opt. Lett.*, 29:2671–2673, 2004.
- [78] D.W. Ward and K.A. Nelson. Finite-difference time-domain (FDTD) simulations of electromagnetic wave propagation using a spreadsheet. *Comput. Appl. Eng. Educ.*, 13:213–221, 2005.
- [79] A. Mayer and F. Keilmann. Far-infrared nonlinear optics. i. $\chi^{(2)}$ near ionic resonance. *Phys. Rev. B*, 33:6954–6961, 1986.
- [80] C. Glorieux, J.D. Beers, E.H. Bentefour, K. Van de Rostyne, and K.A. Nelson. Phase mask based interferometer: Operation principle, performance, and application to thermoelastic phenomena. *Review of Scientific Instruments*, 75:2906–2920, 2004.
- [81] Grant R. Fowles. *Introduction to Modern Optics*. Dover, New York, second edition, 1989.
- [82] Frederic Garet Lionel Duvillaret and Jean-Louis Coutaz. A reliable method for extraction of material parameters in terahertz time-domain spectroscopy. *IEEE J. Selected Topics IN Quantum Electronics*, 2:739–746, 1996.
- [83] Martin van Exter and Ch. Fattinger and D. Grischkowsky. Terahertz time-domain spectroscopy of water vapor. *Opt. Lett.*, 14(20):1128–1130, 1989.
- [84] U. Schneider, P. Lunkenheimer, R. Brand, and A. Loidl. Dielectric and far-infrared spectroscopy of glycerol. *J. Non. Cryst. Solids*, 235-237:173–179, 1998.
- [85] Ronald E. Cohen. Origin of ferroelectricity in perovskite oxides. *Nature*, 359:136–138, 1992.
- [86] R.E. Cohen. Theory of ferroelectrics: a vision for the next decade and beyond. *J. Phys. Chem. Solids*, 61:139–146, 1999.
- [87] M. Sepiarsky, S.R. Phillpot, D Wolf, M.G. Stachiotti, and R.L. Migoni. Atomic-level simulation of ferroelectricity in perovskite solid solutions. *App. Phys. Lett.*, 76(26):3986–3988, 2000.
- [88] M.E. Lines and A.M. Glass. *Principles and Applications of Ferroelectrics and Related Materials*. Clarendon Press, 1977.
- [89] N. Setter and E.L. Colla, editors. *Ferroelectric Ceramics*. Birkhäuser Verlag, 1993.
- [90] Yuhuan Xu. *Ferroelectric materials and Their Applications*. North-Holland, 1991.
- [91] Not just a flash in the pan. *Economist*, 378(8468):26, March 2006. Technology Quarterly Insert.

- [92] Hiroshi Ishiwara, Masanori Okuyama, and Yohihiro Arimoto, editors. *Ferroelectric Random Access Memories*. Topics in Applied Physics. Springer-Verlag, 2004.
- [93] Seung-Eek Park and Thomas R. Shrout. Relaxor based ferroelectric single crystals for electro-mechanical actuators. *Mat Res Innovat*, 1:20–25, 1997.
- [94] R. Blinc and B. Žekš. *Soft Modes in Ferroelectrics and Antiferroelectrics*. North-Holland, 1974.
- [95] W. Cochran. Crystal stability and theory of ferroelectricity. *Advances in Physics*, page 387, 1960.
- [96] R.L. Prater, L.L. Chase, and L.A. Boatner. Raman scattering studies of the impurity-induced ferroelectric phase transition in $\text{KTaO}_3\text{:Nb}$. *Phys. Rev. B*, 23(1):221–231, 1981.
- [97] P.M. Gehring, Henry Chou, S.M. Shapiro, J.A. Hriljac, D.H. Chen, J. Toulouse, D. Rytz, and L.A. Boatner. New Dielectric Resonances in Mesoscopic Ferroelectrics. *Phys. Rev. B*, 46(9):5116, 1992.
- [98] O. Hanske-Petitpierre, Y. Yacoby, J. Mustre de Leon, E.A. Stern, and J.J. Rehr. Off-center displacement of the nb ions below and above the ferroelectric phase transition of $\text{KTa}_{0.91}\text{Nb}_{0.09}\text{O}_3$. *Phys. Rev. B*, 44(13):6700–6707, 1991.
- [99] J. Toulouse, F. Jiang, O. Svitelskiy, W. Chen, and Z.G. Ye. Temperature evolution of the relaxor dynamics in $\text{Pb}(\text{Zn}_{1/3}\text{Nb}_{2/3})\text{O}_3$: A critical Raman analysis. *Phys. Rev. B*, 72:184106, 2005.
- [100] George A Samara. *Solid State Physics: Advances in Research and Applications*, volume 56. Academic Press, 2001.
- [101] J. Toulouse, D. La-Orauttapong, and O Svitelskiy. *Ferroelectrics*, 302:271, 2003.
- [102] Grace Yong, Jean Toulouse, Ross Erwin, Stephen M. Shapiro, and Bernard Hennion. Pretransitional diffuse neutron scattering in the mixed perovskite relaxor $\text{K}_{1-x}\text{Li}_x\text{TaO}_3$. *Phys. Rev. B*, 62, 2000.
- [103] B.E. Vugmeister and M.D. Glinchuk. Dipole glass and ferroelectricity in random-site electric dipole systems. *Review Modern Physics*, 62(4):993–1026, 1990.
- [104] B. I. Halperin and C. M. Varma. Defects and the central peak near structural phase transitions. *Phys. Rev. B*, 14:40304044, 1976.
- [105] J. Toulouse and R. Pattnaik. Collective behaviors in the disordered ferroelectrics KLT and KTN. *Journal of the Korean Physical Society*, 32:S942–S946, 1998.
- [106] E. Bouziane, M.D. Fontana, and M. Ayadi. Phase transition in dilute ktn crystals investigated by raman scattering measurements. *J. Raman Spec.*, 36:872–878, 2005.

- [107] P. DiAntonio, X.M. Wang, J. Toulouse, and L.A. Boatner. Dielectric and raman study of short and long range order in ktn. *Ferroelectrics*, 120:107, 1991.
- [108] Godefroy Kugel, Hans Vogt, Winfried Kress, and Daniel Rytz. Study of the ferroelectric soft mode in solid solutions of $\text{KTa}_{1-x}\text{Nb}_x\text{O}_3$ by hyper-raman scattering. *Phys. Rev. B.*, 30(2):985–991, 1984.
- [109] L. Foussadier, MD FOntana, and W Kress. Phonon dispersion curves in dilute ktn crystals. *J. Phys. Cond. Matt.*, 8:1135–1150, 1996.
- [110] G.A Samara. Glasslike behavior and novel pressure effect in $\text{KTa}_{1-x}\text{Nb}_x\text{O}_3$. *Phys. Rev. Lett.*, 53(3):298–301, 1984.
- [111] J.J. van der Klink, S. Rod, and A. Châtelain. Local properties, long-range order, and quantum ferroelectricity in $\text{KTa}_{1-x}\text{Nb}_x\text{O}_3$. *Phys. Rev. B.*, 33(3):2084, 1986.
- [112] G.A Samara. Pressure as a probe of the glassy properties of disordered ferroelectrics, antiferroelectrics and dielectrics. *Ferroelectrics*, 117:341, 1991.
- [113] U.T. Hochli, K Knorr, and A Loidl. Orientational glasses. *Adv. Phys.*, 39(5):405–615, 1990.
- [114] K.B. Lyons, P.A. Fleury, and D. Rytz. Cluster dynamics in a dipolar glass. *Phys. Rev. Lett.*, 57(17):2207, 1986.
- [115] J. Toulouse. Private Communication.
- [116] P. Doussineau, Y. Farssi, C. Frenois, A. Levelut, J. Toulouse, and S. Ziolkiewicz. Polar fluctuations and first order raman scattering in highly polarizable crystals with off-center ions $\text{KTaO}_3:\text{Li,Nb}$. *Ferroelectrics*, 150:59, 1993.

Benjamin Paxton

- EDUCATION** **MASSACHUSETTS INSTITUTE OF TECHNOLOGY (MIT)** **CAMBRIDGE, MA**
PhD in Physical Chemistry **2006**
Advisor: Keith A. Nelson
- Thesis: "Development of Phonon-Polariton THz Spectroscopy, and The Investigation of Relaxor Ferroelectrics".
 - MIT Sloan courses in strategic management & corporate finance.
- UNIVERSITY OF OREGON** **EUGENE, OR**
B.S. Mathematics & Chemistry, magna cum laude **2000**
- RESEARCH EXPERIENCE** **MASSACHUSETTS INSTITUTE OF TECHNOLOGY (MIT)** **CAMBRIDGE, MA**
Graduate Research Assistant **2000 – Present**
- Developed a new type of spectrometer to measure phase transitions in mixed ferroelectric crystals and provided new understanding of the basic physics.
- Increased functionality of an optical pulse shaper and performed high frequency (2-500GHz) acoustic spectroscopy in low temperature silica glasses.
- Performed nonlinear optical spectroscopies.
- NORTHWESTERN UNIVERSITY** **EVANSTON, IL**
Undergraduate Research Assistant **Summer 1999**
- Performed quantum mechanical calculations to find the vibrational reorganization energy associated with electron transfer in organic molecules.
- UNIVERSITY OF OREGON** **EUGENE, OR**
Undergraduate Research Assistant **1996-2000**
- Organic & inorganic synthesis, electrochemistry, & characterization of self assembled monolayers on gold substrates. Demonstrated feasibility of measuring layer quality with electrochemistry.
- BUISNESS EXPERIENCE** **PATTENT CONSULTANT ApLLoN Inc.** **CAMBRIDGE MA**
Provided paid technical advice on several nanotechnology patents. **2002**
- AWARDS**
- Richard M Noyes Physical Chemistry Achievement Award, University of Oregon (2000)
 - Barry M Goldwater Scholar (1999)
 - Oregon Presidential Scholar (1995-2000)
- PUBLICATIONS & PRESENTATIONS** J. D. Choi, T. Feurer, M. Yamaguchi, B. Paxton, and Keith A. Nelson, "Generation of Ultrahigh Frequency Tunable Acoustic Waves" Applied Physics Letters 87 (8): Art. No. 081907 AUG 22 2005.
- B.J. Paxton, M. Yamaguchi, and K.A. Nelson, "Phonon-polariton based THz spectroscopy," in Ultrafast Phenomena XIV, T. Kobayashi, T. Okada, T. Kobayashi, K.A. Nelson, and S. De Silvestri, eds. (Springer-Verlag, Berlin 2005), pp. 254-256.
- M. Yamaguchi, B. Paxton and K.A. Nelson, "Development of THz Spectroscopy Utilizing Phonon – Polaritons: Applications to Relaxor Ferroelectrics" Workshop on Fundamental Physics of Ferroelectrics, Williamsburg VA, 2004.
- J.D. Beers, M. Yamaguchi, T. Feurer, B.J. Paxton, and K.A. Nelson, "Ultrahigh frequency acoustic phonon generation and spectroscopy with Deathstar pulse shaping," in Ultrafast Phenomena XIV, T. Kobayashi, T. Okada, T. Kobayashi, K.A. Nelson, and S. De Silvestri, eds. (Springer-Verlag, Berlin 2005), pp. 236-238.
- PATENT** Jaime D. Choi, Benjamin Paxton, Thomas Feurer, Masashi Yamaguchi and Keith A. Nelson;
"Characterization of Materials with Optically Shaped Acoustic Waveforms" US Patent 11/186,401.